Nanomechanics and Nanotribology of Protein Films

by

Navinkumar Jayvant Patil

Thesis

Presented to the Department of Physics of

University of Calabria

for the Degree of

Doctor of Philosophy in Science and Technology of Mesophases and Molecular Materials

University of Calabria, Italy

November 2015

Table of Contents

INTRODUCTION

Nature provides numerous examples of organisms and tissues showing outstanding surface adhesion and lubrication properties in wet aqueous conditions where artificial devices and material are ineffective or completely fail. Marine organisms such as sea shells and algae are able to firmly attach underwater to wave-swept rocks and sea hulls. Insects and small reptiles such as the gecko are able to climb vertical walls and rest upside down from horizontal surfaces with various composition (hydrated or waxy hydrophobic plant leaves and fruits, dusty rocks, household glass, etc). Animal tissues and organs such as cartilage, mucosal surfaces or slug slime are very hydrated, and yet provide slippery and robust interfaces for tissue articulation, locomotion and interaction with the external environment. By comparison, artificial glues are typically based on polymers (e.g. acrylates, resins, silicon glue or scotch tape) and unable to bind two surfaces underwater; lubricant fluids contain hydrophobic oils and fats and wear resistant surfaces (e.g. metals, ceramics and plastics) are not hydrate. Understanding the mechanisms adopted by Nature for inhibiting or enhancing surface adsorption, adhesion, friction and wear is a major challenge for modern science, not only from the fundamental point of view but because some of these mechanisms may be replicated in artificial materials and devices. In fact, the field of “biomimetics”, that is the fabrication of functional systems inspired to biological organisms and materials, has been rapidly expanding in recent years in material and surfaces science.

In this thesis we have focused on the *molecular* scale mechanisms of adhesion and lubrication provided by some animal proteins that could be replicated with biomimetic polymers, since proteins and polymers share a chain-like linear molecular structure. Our study did not extent, for instance, to the full scale of biological organs, limbs or organisms (e.g. gecko foot, insect adhesive pads) that could be replicated by artificial devices.

We considered two classes of proteins: (a) the adhesive foot proteins of the Asian green mussel *Perna Viridis* owing their surface adsorption and adhesive properties to the grafting of the functional group L-3,4-dihydroxyphenylalanine (DOPA) on the protein chain, grafted on the polymer chain, and (b) surface-protecting and lubricating mucins, glycoproteins commonly found on the surface of animal tissue and organs, that are heavily grafted with hydrophilic sugar groups. Adhesive foot proteins were provides in purified form by prof. A. Miserez and coworkers at the Nanyang Technologial Univeresity(NTU) in Singapore. Mucins and lubricating polymer were provided by prof. Seunghwan Lee at the Denmark Technological University (DTU) in Copenhagen.

(A) Adhesive proteins of the mussel foot

Animal attachment to a substrate is very different in terrestrial and aquatic environments. In terrestrial environment, gravity is considered as the most important detachment force. In submerged conditions gravity is nearly balanced out by buoyancy but flow forces such as drag and lift are of higher importance.[1] Water is regarded as a contaminant in adhesion

technology because interfacial water leads to dramatic bond failure.[2] Despite this prevalent challenges, wave-swept rocky shores and ship hulls are home to a variety of organisms that have evolved to attach themselves permanently to variety of substrates that are wet, saline, corroded, and/or fouled by biofilms. Mussels are prominent examples of sessile type organisms attaching themselves permanently to variety of underwater solid substrates.

Detailed studies on *Mytilus* mussel genus (blue mussels) during the last decade has enhanced our understanding of underlying physiochemical principles of mussel adhesion. The attachment apparatus of mussels is called the byssus, which is the bundle of threads extending from within the shell of the mussel, each of which terminates in an adhesive plaque attached to a substrate (Fig. 1).[3, 4]

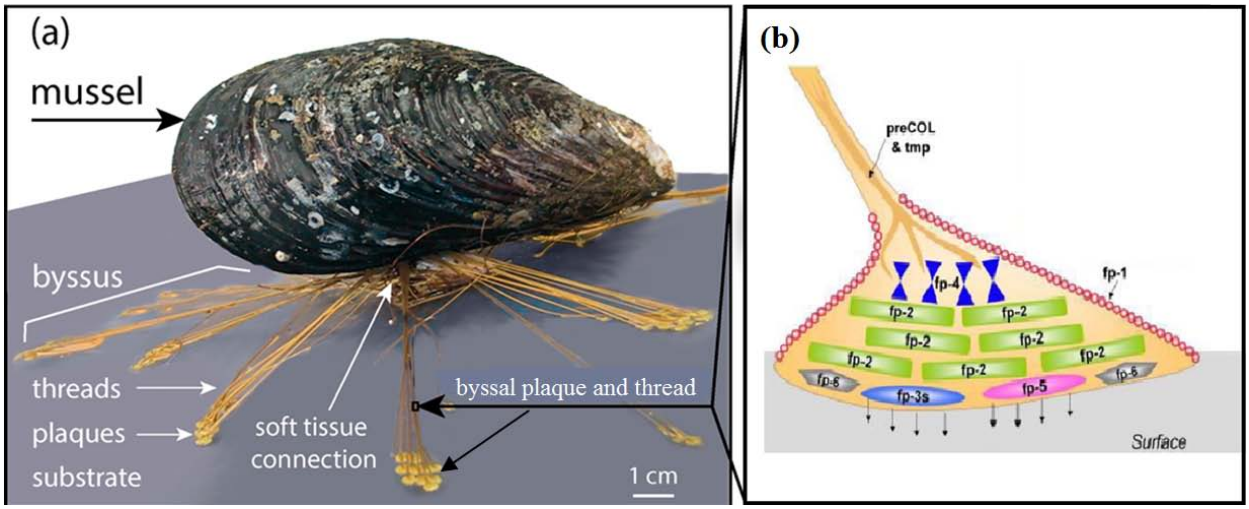

Figure 1 (a) Adhesion of marine mussel.(b) Schematic cross-section of byssal thread and adhesive plaque with approximate location of each of the major proteins. Figures adapted from ref. [7,8].

Byssal thread and adhesive plaque of mussels contains liquid protein mixture that is secreted from within glands of the mussel foot. The plaque proteins are known as mussel foot proteins (mfp). The solidification of the liquid proteins occurs rapidly and the mussel secretes one to several threads in one secreting motion. Finally the mussel body is attached with more than 50 byssal threads and plaques.[5] In the byssal plaque of mussels that is specialized for adhesion, six mussel foot proteins have been identified in the blue mussels (*Mytilus* species) (mfp-2, -3S, -3F, -4, -5, and -6) (Fig. 1.1).[2]All mfps that have been identified for *Mytilus* genus share a common distinguished feature: the presence of Dopa that is added by post-translational hydroxylation of tyrosine (Tyr). Mfps are distinguished by their isoelectric points [Section 1.10] and Dopa content.[6] Mfps found near the interface (e.g. mfp-3, -5 & -6) are the proteins with highest amount of Dopa. The presence of Dopa and its localization near the plaque-substrate interface have prompted the researchers' attention for its likely involvement in surface adhesion.

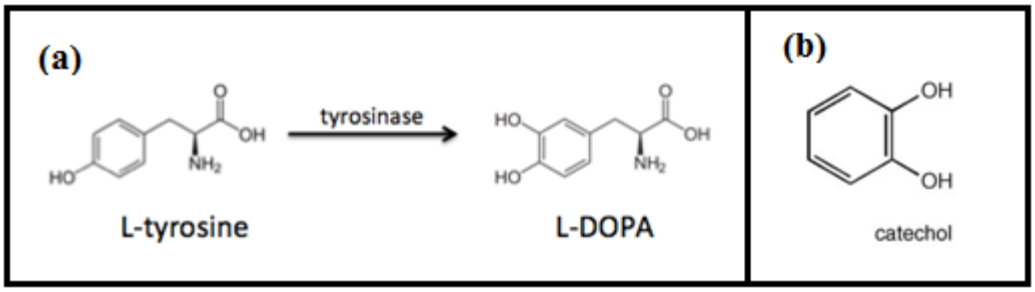

Figure 2 (a) Hydroxylation of Tyr to Dopa and **(b)** catechol in Dopa

In fact, Tyr-DOPA amino acids play multiple key roles in both surface interaction (adhesion) and cohesion (cross-linking). Besides generating the chemical interface to the

substrate, the mussel forms Dopa cross-links between different mfps, which also strengthen cohesion in the mussel foot. It is the catechol (3,4-dihydroxyphenyl) moiety of Dopa that gives Dopa its unique properties to surface coupling and adhesion (Fig. 2b). Catechol bonding mechanism has been studied for several years and different interaction forms and attachment mechanism have been proposed. A brief schematic of diverse interactions of protein-bound Dopa is shown in Fig. 3. The reported routes for Dopa surface bonding include bidentate hydrogen bonding, metal/metal oxide coordination, and oxidative crosslinking.[9]

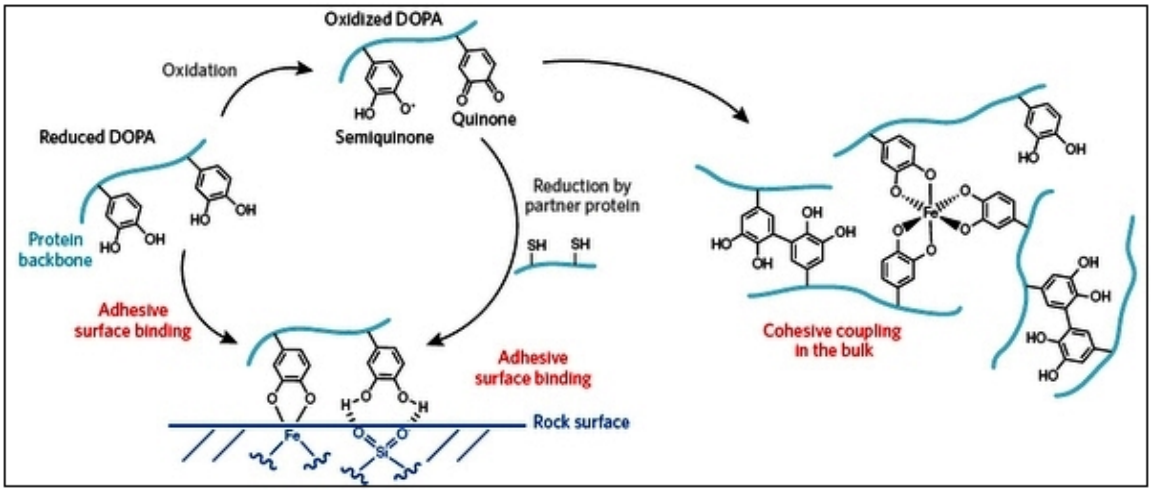

Figure 3. Schematic of adhesion mechanism and reactions of protein-bound Dopa. Figure adapted from ref. [7].

However, intermolecular cross-linking reactions lead to oxidation of Dopa to Dopa-quinone[10] and oxidation compromises the adhesive property Dopa.[11] The strength of adhesion of Dopa rich mfps (mfp -3 and -5) was found to be inversely correlated to the

degree of Dopa oxidation to Dopa-quinone[12] and complete oxidation of Dopa abolished adhesion while reduction back to Dopa restored it. There are several factors which may lead to oxidation of Dopa to Dopa-quinone. Spontaneously oxidation occurs at alkaline pH[13] and auto-oxidation at neutral pH leads to loss of adhesion of mfps to substrates like mica and titanium.[14, 15] Other factors include exposure to light and oxidation over time.

Mussel-inspired biomimetic polymers: Biomimetics has been a very attractive route for scientists and engineers, since the solutions presented by nature to the arising challenges are real wonders and examples of maximizing functionality with reduced energy and materials. The natural adhesive system of marine mussels is receiving growing interest in the context of biomimetics. Unraveling the secrets of mussels underwater adhesion, mussel-inspired polymers having underwater adhesive and sealant properties and synthetic antifouling polymer coatings are being tested and developed and this field has seen tremendous growth, especially in the past 5 years.[16] The following application are briefly discussed below:

1) By incorporating Dopa and analogous reactive groups such as catechols into polymers chains, synthetic biomimetic adhesives, medical polymer adhesives and sealants are being developed.[16,17] Bio-mimetic cross-linking polymers having cohesive and adhesive bonding properties is an active area of research.[16] Injectable wet medical adhesives capable of bonding or repairing tissues are considered one of the frontier areas in this realm. However, there are still great challenges associated with adhering in the presence

of excess biological fluid, as well as the usual concerns related to the biological response to synthetic polymers.[17] Several synthetic and natural medical adhesives are currently used in a number of medical specialties. These include mainly fibrin, cyanoacrylate and gelatin-resorcinol-formaldehyde (GRF) glues.[18] However, currently used biocompatible glue like fibrin glue suffers for weak cohesive strength and blood-borne disease transmission is a major concern with this glue. Cyanoacrylate adhesives and gelatin-resorcinol-formaldehyde (GRF) glue have been shown to display higher bond strength but they release toxic formaldehyde on degradation. Mussel glue with its several key properties like ability to solidify rapidly in an aqueous environment, high adhesive and cohesive strength, and versatile ability to adhere toboth inorganic and organic surfaces, appeals use of their mimics as medical adhesives.[18]

2) Marine biofouling refers to an undesirable process in which the underwater surface becomes encrusted with living organisms and their by-products. Marine biofouling is a huge problem to naval and shipping industry as it decreases the vessel speed and increases fuel consumption. Previous generation antifouling coatings used tributyltin (TBT) which are now prohibited since they were detrimental to non-target organisms and the surrounding environment.[19] Current antifouling paints release copper and copper toxicity is under recent scrutiny. Better understanding of marine biological adhesives may help develop antifouling surfaces without having to load the water with toxics and kill the foulers.[20] Besides marine biofouling, medical devices coming in continuous contact with biological milieu suffer from nonspecific interaction of cells, proteins and

microorganisms with material surfaces and these interactions can prove highly problematic for device efficacy and safety.[21]

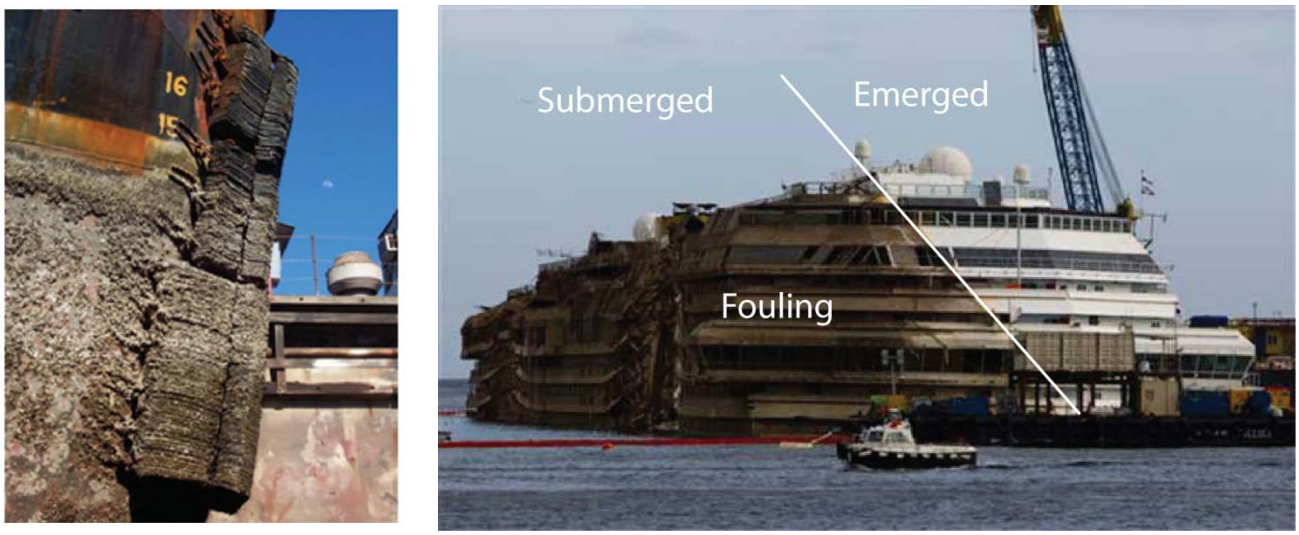

Figure 4. Biofouling on the hull of a ship increases drag and fuel consumption. The right images show the wreckage of the Costa Concordia cruise ship after being pulled up. Marine biofouling was evident below the line of buoyancy after one year and a half of immersion of the ship decks.

The strategy of using mussel adhesive protein mimic can make outstanding surface anchors for antifouling polymers which can control marine biofouling and fouling of medical devices by proteins, cells and bacteria. Although the catechol side chain of Dopa is a powerful anchor for surface coating, but adhesion of mussel byssus is more complicated than a simple catechol-mediated recipe. There is still a long way to go in the field of biomimetics and materials science to really mimic mussel foot proteins to generate the best underwater adhesives, biofouling polymers and universal coatings

The current state of knowledge on the nature and properties of mussel adhesion is based only on limited set of mussel species studied. The overall objective of this research is to gain a better understanding of the molecular basis of adhesion in green mussels so that in the future, this knowledge can be implemented in the design of alternate mussel inspired bioadhesives and targeted anti-fouling strategies. In order to understand mussel adhesion however, there is a need to first characterize the proteins that constitutes the adhesive plaque and are localized near the plaque-substrate interface. To fully understand mussel adhesion, it is essential to understand the time-regulated secretion and interplay between the *P. Viridis* foot proteins (Pvfps). Pvfp-5 is the first protein to initiate interaction with the substrate, displacing interfacial water molecules and forming adhesive bonds with the substrate.[2] Pvfp-3 is subsequently secreted in addition to Pvfp-5, followed by the addition of Pvfp-6 in the last step of plaque deposition.[2] Additionally, Pvfps are enriched with cysteine (Cys) and tyrosine (Tyr)/Dopa residues.

Cys has low pK_a, which allows the formation of thiolate at pH 5.5 inside the mussel. Since thiolates are more reductive than thiols, the thiolates are the operative antioxidant group in mussel foot proteins.[22] The mechanism of the dopaquinone reduction to catechol by thiolates is proposed to consist of two steps: (i) nucleophilic attack of quinone by the first thiolate anion to form S-cysteinyldopa adducts; (ii) the thiolether adducts are attacked by a second thiolate anion to form a disulfide and dopa, as depicted in Fig. 5.

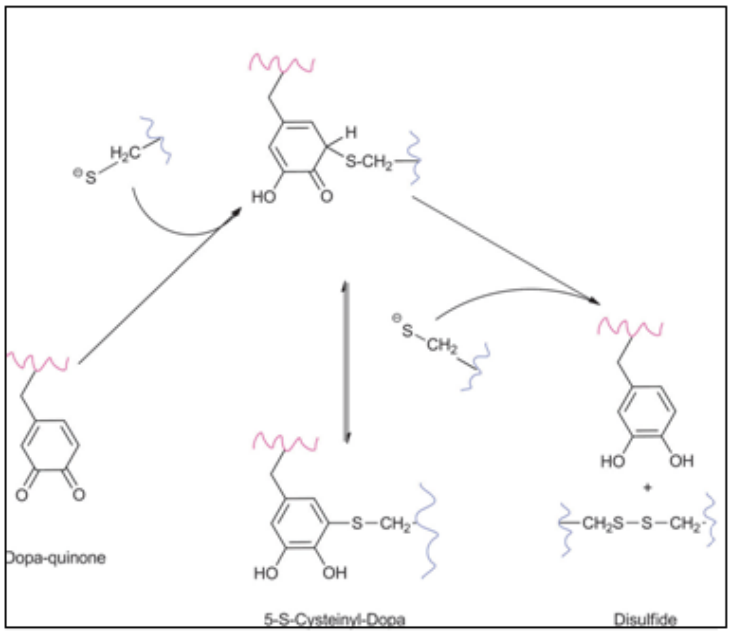

Figure 5. Proposed reaction mechanism of the quinone reduction by thiolates.[22]

Presence of Cys in all known Pvfps and potential of Cys to prevent Dopa oxidation via redox chemistry suggests that the mechanism of adhesion may be significantly different in *P. Viridis* and that distinction could represent different strategy of underwater adhesion.

Our work was to investigate the adhesive properties of *P. Viridis* foot proteins, Pvfp-3 and Pvfp-5, which are localized near the plaque-substrate interface, enriched with Dopa and cysteine residues and are the first proteins to be secreted by *P. Viridis*. Different experiments with varying conditions of pH, ionic strength, adsorption time, concentration, etc., were conducted to study their effect of adhesive properties of these proteins. The surface force apparatus (SFA) measures interaction forces between two surfaces with nano-Newton and Angstrom distance resolution and has enabled precise,

sensitive, and highly reproducible analysis of adhesive properties of mfps. SFA was employed to investigate adhesion properties of Pvfp-5 and Pvfp-3.

(B) Lubricating and surface-protecting mucin proteins

In nature, biological surfaces in motion are common. These surfaces are often surrounded by fluid-film, composed of different biological molecules like proteins, lipids, polysaccharides, etc. Saliva is composed of water and macromolecules that serve as a biological lubricant in oral cavity. Aritcular joints are surrounded by lubricating synovial fluid. Epithelial surfaces of many biological organs and tissues, including mouth (teeth ad tongue), eyes(cornea and eyelids), articular joints(cartilage), and gastrointestinal, respiratory, and reproductive tracts are coated with highly hydrated protein gel called mucus layer.[23-26] The function and composition of mucus gel differs at different locations of body but the normal functions ascribed to mucus gel includes lubrication and maintenance of hydrated layer over epithelium, protection against adsorption of unwanted biomolecules, bacteria, and particles, and protection of the underlying tissues against wear.[27]

Mucus gel contain various proteins and biopolymers. However, the essential and distinctive ingredients are mucins, a class of high-molecular-weight glycosylated proteins whose biophysical properties are due to highly hydrated oligosaccharide sugar side-chains that make up 50%-90% of the molecular weight.[28]

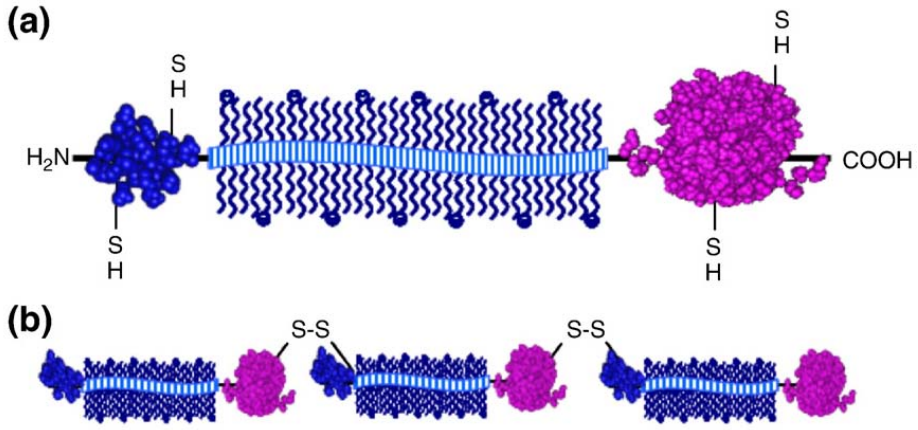

Figure 6. Structure of (a) a typical mucin subunit showing a central linear glycosylated domain flanked by globular domains and (b) a mucin molecule composed of subunitslinked linearly by disulfide bonds. Figure adapted from ref.[28].

Fig. 6 shows different regions in mucin molecule. The terminal regions are very lightly glycosylated, but rich in cysteines, which are involved in disulphide linkages and taking part in intermolecular interactions with other proteins, mainly bonding with other mucins,[29] mucin self-association and mucin adsorption on surfaces. Large glycosylated central regions in which half of the amino acids are serine and threonine are saturated with hundreds of O-linked oligosaccharides sugar side chains. Glycosylation involves covalent bonding of carbohydrates (oligosaccharides, sugars) to the polypeptide backbone of proteins. The oligosaccharides sugar side chains make up to 50–90 % of the mucin mass. N-linked oligosaccharides are also found on mucins, but much less abundantly. Glycosylation generally has a major impact on the structure and physiochemical properties of proteins. In mucins, glycosylation is important for their stability, folding, solubility and rheological properties.[30]

Most oligosaccharides are terminated by sialic acid (pKa~ 2.6) residues and, along with sulphate groups (pKa~ 1), they generally give mucins a net negative charge under most physiological conditions. The negatively charged central domain is responsible for the intramolecular repulsion rendering the mucin their expanded bottle-brush structure (Fig. 6).

Mucin molecules play a central role in determining the viscous properties of bodily fluids such as saliva, tears and synovial fluids, and the lubrication of mucosal surface and mucin coated tissues (e.g. saliva coated teeth or cornea wet by tears). Lubrication in the presence of a fluid may occur in one of three regimes (boundary lubrication, mixed lubrication, and hydrodynamic lubrication), and mucins facilitate lubrication in each regime.[28]All these three regimes of lubrication can be conveniently visualized in a Stribeck curve, in which coefficient of friction is plotted as a function of shear velocity and fluid viscosity (Fig. 7).

Boundary lubrication occurs when the two surfaces are in close contact due to high contact pressure and shear velocity and fluid viscosity are low. Surface interactions are dominated by the contacting monolayer or multilayer films of the boundary lubricant and repulsive forces between adsorbed layers carry the load and prevent adhesion between contacting asperities thus lowering the overall friction.[28,30] For being an effective lubricant in this regime, a lubricant molecules should either tightly adhere to the surface to avoid being sheared away or re-adsorb quickly enough from solution to replace elements of surface layer that have been sheared off.[28]

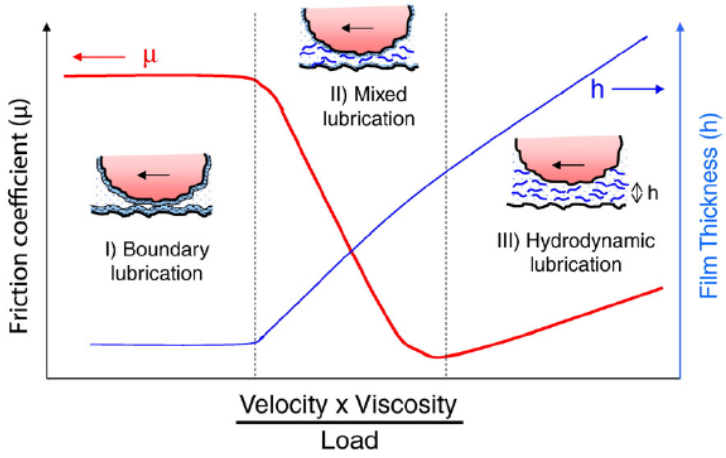

Figure 7. Friction coefficient plotted as a function of fluid viscosity and shear velocity divided by load (Stribeck curve) with corresponding lubrication film thickness. The schematic shows boundary, mixed, and hydrodynamic lubrication regimes. Figure adopted from ref.[28].

In mixed mode lubrication, the formation of the fluid film results in corporately lower friction than at the boundary condition but some contacting surface asperities cause friction. Hydrodynamic lubrication occurs at high speed regime and the surfaces are fully separated by fluid film. The pressure which supports the separation of surface originates from the change in viscosity of the lubricant at high speed.

Mucins are highly surface active molecules and are able to adhere to wide variety of surfaces depending on substrate chemistry, substrate charge, solution concentration and ionic strength.[28] Hydrophobic residue in the terminal domain of mucins have proven to be of paramount importance for the boundary lubrication properties of mucins between hydrophobic surfaces. Mucins adsorb onto hydrophobic surfaces with characteristic 'bottle-brush' structure, where the hydrophobic moieties in the polypeptide backbone of

mucins form anchoring bonds with surface via hydrophobic interactions and hydrophilic glycosylated regions stretch to bulk water.[31] Adsorption and lubrication by mucins are not restricted to hydrophobic surfaces, and have also been reported for hydrophilic surfaces.[32] Surface adsorption and lubrication studies have been studied most extensively. Surface force apparatus was initially used to study properties of adsorbed mucins at solid-liquid interface.[33,34,35] Atomic force microscopy (AFM) was used to image the molecular shape, size and morphology.[36,37] Optical waveguide lightmode spectroscopy (OWLS)[38,39] and ellipsometry[40] were used to determining the mass of surface adsorbed mucin. Tribological studies of mucins have been performed under many different conditions, at both macro- and micro scale, mainly using a pin-on-disc (PoD) tribometer, a mini traction machine (MTM), colloidal force microscopy or an SFA.[39,41,42]

Due to the their relevance to food industry, bovine submaxillary mucin (BSM) and porcine gastric mucin (PGM) are some of the most extensively studied mucins. BSM is extracted from the fresh salivary glands of cows and PGM is isolated from the lining of the stomach of pigs. Submaxillary mucins secreted in saliva, lines teeth, tongue, and palate, and interacts with food, external liquids, and air, while gastric mucins protect the stomach from attack by digestive acid and enzymes. These mucins from bovine and porcine sources have several potential biomedical applications. However, high molar mass, polydisperse nature and presence of contaminants in mucins have always complicated their controlled study. Aggregation and adsorption properties of BSM and PGM differ widely as well as their ability to reduce friction are different, but they do

share important similarities that are favorable for lubrication. Boundary lubrication provided by these mucins is due to their high level of glycosylation, their ability to adsorb strongly to a broad range of surfaces and the presence of steric repulsion between their adsorbed layers. However, role of hydration, effect of varying pH and ionic strength on lubricating properties of mucins is not very well understood. Also mechanical wear is of practical concern for many biological surfaces where mucins are present. However, little is understood about the relationship between friction and wear, and how mucins prevent wear in biological systems.

Mucins are particularly studied for possible application in biomedical engineering that require a high degree of control over the tribological performance of sliding systems, as a quality of life could be reduced significantly in case of excessive friction and wear of the running surfaces. Mucins are lubricious, biocompatible, show good adhesivity and form hydrogels. These features are of potential benefit in medical coating applications. Mucins can be directly incorporated into the surfaces of existing biomedical devices and can also serve as excellent model for biomimetic design of synthetic polymers, such as brush forming co-block polymers that are able to both adsorb onto surfaces and retain water. Interest in aqueous lubrication has recently been growing due to its high relevance in biological tribosystems and potential biomedical applications such as knee and hip joint implants, catheters, and endoscopes, where traditional engineering lubricants (e.g., petroleum-based mineral oils and greases) are excluded because of biocompatibility issues. Bio-compatible coatings for artificial bone implants can improve surgical

recovery times, life span of an implant and reduce the need for revision surgery. The possibility of using these unique property of mucins for creating novel mucin-based biomaterials and in areas of drug delivery has gained lot of interest.

In this thesis we considered BSM and PGM. Commercially available BSM contains contaminants (e.g Bovine serum albumin (BSA)). The aim of study on BSM was to investigate influence of pH on interaction between BSM coated surfaces across aqueous media using SFA, in which purified BSM was used in order to understand the interaction free from other biomolecules. Also, aggregation of mucins, especially acid-induced aggregation, has been actively studied with PGM, but the influence of acidic medium on BSM is very rare in literature, and was studied using SFA and dynamic light scattering (DLS). The nanoscale mechanism of surface force generation by adsorbed mucin layers were studied, which underlie surface-protecting and lubricating properties.

Due to the molecular nature of mucin, it interacts with most substances including cationic biopolymers. Cationic polymers such as chitosan and some synthetic polymethacrylates have been reported to show excellent mucoadhesive performance. Polycation polyethylenimine (PEI), due to its strong interation with mucins has emerged as the choice transgene delivery agent or transfection reagent and have been extensively used in medicine industry due to its suitable characteristics for variety of biomedical applications. However, interaction of branched PEI (b-PEI) with mucin glycoproteins and its impact on lubricating properties of mucins were unexplored. Lubricating properties of PGM are known and PGM exhibits effective boundary lubrication under specific conditions of

acidic pH. Since acidic pH conditions are less relevant to applications in the areas of biomedical sciences, the specific objective of this work on PGM was enhancing its lubricating properties via its synergistic complexation with b-PEI in neutral pH conditions.

References

[1] Ditsche, P.; Summers, A. P. *Beilstein J. Nanotechnol.***2014,** 5, 2424–2439.
[2] Petrone, P.; Kumar, A.; Sutanto, C. N.; Patil, N. J.; Kannan, S.; Palaniappan, A.; Amini, S.; Zappone, B.; Verma, C.; Miserez, A.; *Nature comm.***2015**, 6:8737.
[3] Waite, J. H. *Chem. Industry*, **199**1, 2, 607–611.
[4] Waite, J. H. *Ann. NY Acad. Sci.*, **1999**, 875, 301–309.
[5] Nishida, A.; Ohkawa, K.; Ueda, I.; Yamamoto, H. Biomolecular Engineering, 2003, 20, 381-387.
[6] Hwang, D.S.; Zeng, H.; Masic, A.; Harrington, M. J.; Israelachvili, J.; Waite, J. H. *Journal of Biological Chemistry* **2010**, , 285, 25850–25858.
[7] Houwink, R.; Salomon, G. Adhesion and adhesives. 2nd Ed. Vol. 1. Amsterdam (The Netherlands): Elsevier; 1965.
[8] Miller, D. R.; Das, S.; Huang, K.; Han, S.; Israelachvili, J. N.; Waite, J. H. *ACS Biomater. Sci. Eng.* **2015**, 10, 1021.
[9] Wilker, J.J. *Nature Chemical Biology***2011**, 7, 579–580.
[10] Yu, M.; Hwang, J.; Deming, T. J. *J Am ChemSoc*, **1999**, 121, 5825–5826.
[11] Lee, H. S.; Scherer, N. F.; Messersmith, P. B. *P Natl AcadSciUSA*, **2006**, 103, 12999–13003.
[12] Danner, E.; Kan, Y. J.; Hammer, M.; Israelachvili. J. N.; Waite, J. H. *Biochemistry*, **2012**, 51(33), 6511–6518.
[13] Waite, J. H. *Comp BiochemPhysiol B Comp Biochem*, **1990**, 97, 19–29.
[14] Yu, J.; Wei, W.; Danner, E.; Ashley, R. K.; Israelachvili, J. N. *Nat ChemBiol*, **2011**, 7, 588–590.
[15] Menyo, M. S.; Hawker, C. J; Waite. J. H. *Soft Matter*, **2013**, 10314.
[16] Matos-Pérez, C. R.; White, J. D.; Wilker, J. J. *J. Am. Chem. Soc*.**2012**, 134, 9498−9505.
[17] Lee, B. P.; Messersmith, P. B.; Israelachvili, J. N.; Waite, J. H.*Annu Rev Mater Res.***2011**, 41, 99–132.
[18] Lee, B. P.; Dalsin, J. L.; Messersmith, P. B. *Biological Adhesives*, (ed. by A.M. Smith and J.A. Callow), **2006,** Springer-Verlag Berlin Heidelberg.
[19] Magin, C. M.; Cooper, S. P.; Brennan, A. B. *Materialstoday* 2010 , 13(4), 36-44.
[20] Wilker, J. J. *Current Opinion in Chemical Biology* **2010**, 14, 276–283.
[21] Dalsin, J. L.; Messersmith, P. B. *Materialstoday***2005**,1,38-46.

[22] Yang, J.; Cohen Stuart, M. A.; Kamperman, M. *Chem. Soc. Rev.*, **2014**, 43, 8271.
[23] Perez-Vilar, J.; Hill, R. L. *J. Biol. Chem.***1999**, 274, 31751−31754.
[24] Dekker, J.; Rossen, J. W. A.; Buller, H. A.; Einerhand, A. W. C. *Trends Biochem. Sci.***2002**, 27, 126− 131.
[25] Bansil, R.; Turner, B. S. *Curr. Opin. Colloid Interface Sci.***2006**, 11, 164−170.
[26] Hoorens, P. R.; Rinaldi, M.; Li, R. W.; Goddeeris, B.; Claerebout, E.; Vercruysse, J.; Geldhof, P. *BMC Genomics***2011**, 12, 140−151.
[27] Zappone, B.; Patil, N. J.; Madsen, J. B.; Pakkanen, K. I.; Lee, S. Langmuir **2015**, 31, 4524−4533.
[28] Coles, J. M.; Chang, D. P.; Zauscher, S. *Current Opinion in Colloid & Interface Science***2010**, 15 406–416.
[29] Madsen. J. B. Investigation of the surface adsorption and biotribological properties of mucins, Ph. D. Thesis, July-**2014**.
[30] Thornton, D. J.; Rousseau, K.; McGuckin, M. A. *Annual Review of Physiology***2008**, *70*, 459-486.
[31] Malmsten, M.; Blomberg, E.; Claesson, P.; Carlstedt, I.; Ljusegren, I. *J Colloid Interface Sci***1992**, 151, 579–90.
[32] Pettersson, T.; Dedinaite, A. J. *Colloid Interface Sci.***2008**, 324 , 246-256.
[33] Proust, J. E.; Baszkin, A.; Boissonnade, M. M. *C R AcadSciSer Ii***1982**, 294, 1325–8.
[34] Perez, E.; Proust, J. E.; Baszkin, A.; Boissonnade, M. M. *Colloids Surf***1984**, 9, 297–306.
[35] Perez, E.; Proust, J. E. *J Colloid Interface Sci***1987**, 118, 182–91.
[36] Hong, Z. N.; Chasan, B.; Bansil, R.; Turner, B. S.; Bhaskar, K. R.; Afdhal, N. H. *Biomacromolecules***2005**, 6, 3458–66.
[37] McMaster, T.J.; Berry, M.; Corfield, A. P.; Miles, M. J. *Biophys J***1999**, 77, 533–41.
[38] Horvath, R.; McColl, J.; Yakubov, G. E.; Ramsden, J. J. *J Chem Phys***2008**, 129, 071102.
[39] Lee, S.; Muller, M.; Rezwan, K.; Spencer, N. D. *Langmuir***2005**, 21, 8344–53.
[40] Nikonenko, N.A.; Bushnak, I.A.; Keddie, J.L. *ApplSpectrosc***2009**, 63, 889–98.
[41] Harvey, N.M.; Yakubov, G. E.; Stokes, J. R.; Klein, J. *Biomacromolecules***2011**, 12(4), 1041-1050.
[42] Proust, J.E. *Colloids and Surfaces* **1984**, 10, 43-52.

CHAPTER 1

Background, Methods and Materials

A polymer, from a physicist's point of view, is a set of units, called monomers, connected linearly as a chain.[1] Biopolymers like DNA, proteins as well as real polymers are essentially long chain molecules that are formed by chemically bonding monomers. Unstructured proteins can be viewed as linear assemblies of amino-acids and some protein properties can be measured and understood using experimental methods and ideas developed in polymer physics. This chapter introduces the basic theoretical concepts of polymer physics and describes the methods used to characterize proteins diffusing in solution and adsorbed on solid surfaces. The Surface Force Apparatus at CNR-Nanotec will be described in some detail as the results obtained during this thesis were the first to be published using this technique. Because we considered proteins that are secreted in a water-based extracellular environment, the role of water and electrolytes in protein conformation, adsorption and surface adhesion will also be briefly reviewed.

1.1 Statistical models of polymer chains: the ideal chain

The simplest model for the statistical theory of polymer chain conformation treats the molecule as a chain of N+1 rigid subunits or "monomers" with the same mass and length, joined by N perfectly flexible hinges. The position of i^{th} monomer unit is given by the position vector $\vec{R}_i$ and the chain configuration can be expressed by the set of bond

vectors $\{\mathbf{u_i}\}$ = $(\mathbf{u_1}, \mathbf{u_2}, ..., \mathbf{u_N})$ with length l(Fig. 1.1).[2] The end-to-end distance vector connects the chain ends:

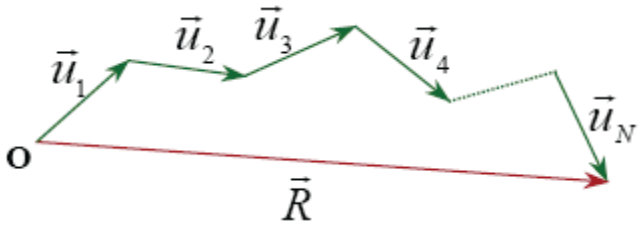

Figure 1.1. Model polymer chain

$$\mathbf{R} = \mathbf{R_N} - \mathbf{R_0} = \sum_{\mathbf{i=1}}^{\mathbf{N}} \mathbf{u_i} \tag{1.1}$$

and reaches the maximum value $R_{MAX} = Nl$ when the chain is fully extended. Since the chain can extend in any direction, the mean value of $\boldsymbol{R}$ is zero. Instead we consider the mean square end-to-end distance, $\langle \boldsymbol{R}^2 \rangle$.

$$\boldsymbol{R}^2 = \left(\sum_{i=1}^{N} \boldsymbol{u}_i \right) \left(\sum_{j=1}^{N} \boldsymbol{u}_j \right) = \sum_{i=1}^{N} \sum_{j=1}^{N} \boldsymbol{u}_i \cdot \boldsymbol{u}_j \,, \tag{1.2}$$

$$\langle \boldsymbol{R}^2 \rangle = \sum_{i=1}^{N} \sum_{j=1}^{N} \langle \boldsymbol{u}_i \cdot \boldsymbol{u}_j \rangle = \sum_{i=1}^{N} \langle \boldsymbol{u}_i^2 \rangle + \sum_{\substack{i,j=1 \\ i \neq j}}^{N} \langle \boldsymbol{u}_i \cdot \boldsymbol{u}_j \rangle \,. \tag{1.3}$$

The size of the chain can also be characterized by the radius of gyration R_g defined as:

$$R_g^2 = \frac{1}{N+1} \sum_{i=1}^{n} (\boldsymbol{R}_i - \boldsymbol{R}_{CM})^2 \,. \tag{1.4}$$

where $\vec{R}_i$ and $\vec{R}_{CM}$ are the position vectors of the i-th monomeric unit and center of mass. If the chain is freely joined and there is no restriction on the orientation of one segment

with respect to its neighbor, $\langle \boldsymbol{u}_i \cdot \boldsymbol{u}_j \rangle = 0$ for $i \neq j$, and $\langle \boldsymbol{u}_i^2 \rangle = l^2$. Therefore Eq. 1.3 becomes:

$$\langle \mathbf{R}^2 \rangle = \sum_{i=1}^{N} \langle \mathbf{u}_i^2 \rangle = Nl^2 = R_{MAX} l \,. \tag{1.5}$$

so that the size *R*, measured by the root mean square (rms) end-to-end distance of a polymer, depends on its length N as,

$$R \sim lN^{\nu}, \tag{1.6}$$

where $\nu = 1/2$ for the freely jointed chain (FJC) (Fig. 1.2). The exponent ν is called the size exponent.[1]

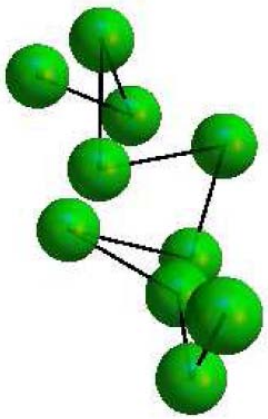

Figure 1.2: Representation of freely jointed chain for a polymer with rigid bonds and full free rotations. The beads and bonds may cross without any penalty.[1]

For FJC, the radius of gyration is $R_g = \left(\frac{Nl^2}{6} \right)^{1/2}$. Thus the average radius of gyration can be written as:

$$\left\langle R_g^2 \right\rangle = \frac{Nl^2}{6} = \frac{\left\langle R^2 \right\rangle}{6} \tag{1.7}$$

1.2 Freely rotating and worm-like chains

The freely jointed chain model can be adapted fairly easily to somewhat more realistic chains with orientational correlation between successive bonds. Consider a polymer chain having a sufficiently long backbone consisting entirely of N single bonds of fixed bond length l and fixed bond angle ϕ, but with free rotation around any of the single bond. The complementary angle θ will be equal to $\theta = 180^\circ - \phi$. In this case the scalar product of the vectors $\left\langle \boldsymbol{u}_i \cdot \boldsymbol{u}_j \right\rangle$ along the chain will be given as:

$$\left\langle \boldsymbol{u}_i \cdot \boldsymbol{u}_j \right\rangle = u_i u_j \cos\phi = l^2 \cos\phi \neq 0 . \tag{1.8}$$

We substitute the second term on the right side of Eq. 1.3 with Eq. 1.8 to obtain $\left\langle \boldsymbol{R}^2 \right\rangle$ of the freely rotating chain:

$$\left\langle \boldsymbol{R}^2 \right\rangle = Nl^2 + l^2 \sum_{\substack{i,j=1 \\ i \neq j}}^{N} \left\langle \cos\phi_{i,j} \right\rangle$$

Since $\left\langle \cos\phi_{i,i+1} \right\rangle = \cos\theta$, $\left\langle \cos\phi_{i,i+2} \right\rangle = \cos^2\theta$ and $\left\langle \cos\phi_{i,i+k} \right\rangle = \cos^k\theta$

$$\left\langle \boldsymbol{R}^2 \right\rangle = Nl^2 + 2l^2 \sum_{i=1}^{N} \sum_{k=1}^{N-i} \left\langle \cos\phi_{i,i+k} \right\rangle = Nl^2 + 2l^2 \sum_{i=1}^{N} \sum_{k=1}^{N-i} \cos^k\theta \approx Nl^2 \frac{1+\cos\theta}{1-\cos\theta} \tag{1.9}$$

The freely rotating chain in the limit of small bond length, $l \to 0$, and bond angle close to zero, $\phi \to 0$, is called worm-like chain (WLC), because it looks like an infinitely thin

chain of a continuous curvature. The worm-like chain has the defined value of contour length, $R_{MAX} = Nl\cos\left(\frac{\phi}{2}\right)$.

1.3 Kuhn length and persistence length

At length scales equal or smaller than the monomer length *l*, the polymer chain is considered rigid. In many situations, the flexibility of a polymers is not very noticeable below a certain length $l_K > l$ known as effective length or Kuhn length. Over a length scale larger than l_K the polymer flexibility becomes noticeable. The Swiss physical chemist Werner Kuhn (1899-1963) first used the concepts of statistical mechanics to understand polymers and he suggested the idea of effective/Kuhn length. A molecule of contour length s contains $N_{eff} = s / l_K$ Kuhn segments. Since Kuhn segments are nearly independent, we can imagine they are freely jointed, and use Eq. 1.5:

$$\mathbf{R}^2 = \left\langle \mathbf{R}^2 \right\rangle = N_{eff} l_K^2 = (s / l_K) l_K^2 = s \cdot l_K \quad . \tag{1.10}$$

Eq. 1.10 gives the length of the effective Kuhn segment. The Kuhn length for real polymers ranges from about 1 nm for simple synthetic chain to about 100 nm for DNA. Notice that the bond vector *l* considered in section 1.1 is exactly the Kuhn length of the ideal freely-jointed chain. Also, a rigid linear molecule or rod of length l_R can be considered as a polymer with Kuhn length $l_K >> l_R$.

The persistence length, l_P, is defined as the distance along the molecule beyond which the orientation of one segment loses its correlation with the orientation of another. Fig.

1.3 shows two points on the chain separated by contour length *s*. Since the chain flexes, the tangent vectors at two points are generally different. The angle between them is $\gamma(s)$.

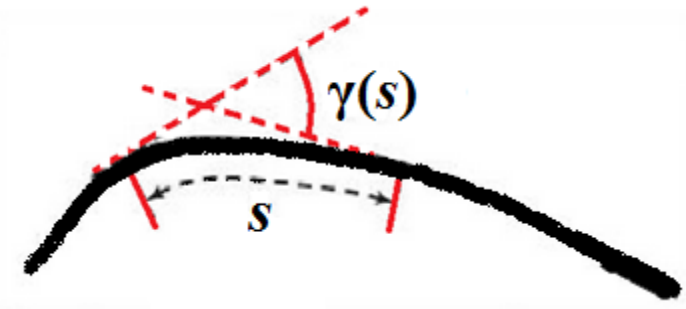

Figure 1.3. Diagram explaining the concept of persistence length: the angle between the tangents of two points contour distances apart is γ.

If s is reasonably large, the expectation value of the cosine of the angle falls off exponentially with distance,[1]

$$\langle \cos\gamma(s) \rangle = e^{-(s/l_P)} \tag{1.11}$$

where l_p is the persistence length. If $s << l_p$, Eq. 1.11 gives $\langle \cos\gamma \rangle \approx 1$ and the angle fluctuates around zero, whereas if $l_P << s$, then $\langle \cos\gamma \rangle \approx 0$. Thus, γ can be anything between 0 to 180 with equal probability. Thus for lengths greater than l_p, the correlation in orientation of segments is lost. If $l_p > s$, the chain behaves like a stiff rod.

1.4 Non-gaussian behavior and simple Flory theory

This section has been developed mainly basing on ref.[1]. The FJC is also known as *ideal* chain since it is characterized by Gaussian behavior. It also goes by the name of Gaussian

polymer or non-self-interacting polymer. The excluded volume makes the real chains non-ideal.

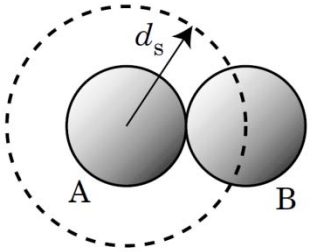

Figure 1.4. Excluded volume of a sphere. The sphere of radius d_s indicated by dashed line is the space not available to the center of sphere B.

The dimension of real chain is different than that of the ideal chain of the same contour length. In a real polymer, interactions between monomers close to each other in space cannot be neglected (Fig. 1.4). By introducing the repulsive interaction of the monomers, e.g., the thermal excluded volume interaction, we go beyond the Gaussian behavior. The fact that monomers cannot interpenetrate is taken into account by considering hard-wall repulsion, that is proportional to the excluded volume v_{exe} of each pair of monomers, times the number of monomer pairs (N^2) per unit of available volume (R^3), that is

$$\text{repulsive energy} \sim v_{exe} \frac{N^2}{R^3} \tag{1.12}$$

The entropy of the chain is given by

$$S_N(R) = k_B \log P(R, N) \sim -\frac{R^2}{Nl^2}, \tag{1.13}$$

where $P(R,N)$ is the probability distribution of the end-to-end distance to be Gaussian, k_B is the Boltzmann constant. The free energy of a polymer chain of *N* monomers with excluded volume interaction if it had size of radius *R* at temperature T is equal to,[1]

$$F_N(R) = F_0 + e_0 \frac{R^2}{Nl^2} + e_1 v_{exe} \frac{N^2}{R^3}, \qquad (1.14)$$

e_0 and e_1 are T-dependent constants and F_0 is the remaining part of the free energy. The size of the unconstrained polymer comes from a minimization of $F_N(R)$ with respect to R which has the form of Eq. 1.6, but with ν = 3/5 instead of 1/2. This ν is called the Flory exponent.

1.5 Surface forces and general theory of molecular interactions in aqueous medium: the DLVO theory

Surface forces and interactions relevant to biopolymer systems in an aqueous environment can be quantitatively described using the DLVO theory of colloidal stability that is named after Derjaguin, Landau, Verwey and Overbeek. DLVO theory was initially developed to describe interactions between colloids in liquids which assumes that the interaction forces can be approximated by a superimposition of van der Waal attractive forces and electric double layer repulsive contributions.

For charges of same sign in liquid medium, the DLVO theory predicts repulsion at large separations originating from so-called double-layer of co-ions and counterions, whereas attractive van der Waals attraction becomes more significant at shorter distances.

Increasing the electrolyte concentration of the medium causes shielding of the electrostatic repulsion, and the balance between the DLVO forces can be altered towards the van der Waals attraction between the interacting bodies.

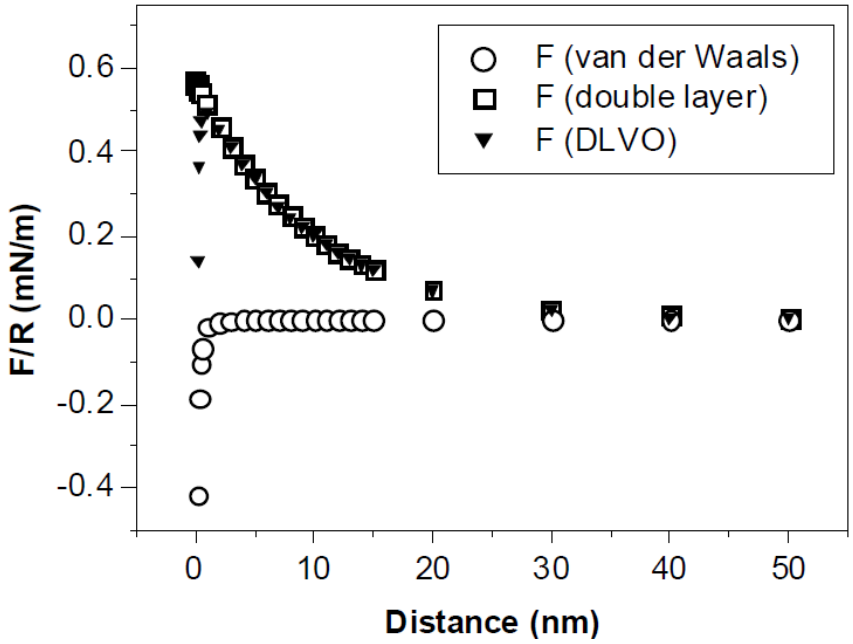

Figure 1.5. Contributions of the van der Waals and the electrostatic double-layer forces to the total DLVO interaction. Calculated according to equations 1 and 4.[3]

van der Waals forces

The van der Waals forces consists of three different types of forces that originate from time-dependent dipoles in atoms or molecules. They include contributions from forces between two permanent dipoles (*Keesom* forces), forces originating from permanent dipole-induced dipole interactions (*Debye* forces) and forces due to interaction between spatially fluctuating electron cloud distribution (*London* forces).

The detailed description of van de Waals forces can be found in the textbook of Israelachvili.[4] The non-retarded van der Waals force $(F_{vdW}(D))$ between two spheres of radius and is $F_{vdW}(D) = -\frac{A_H}{6D^2} \cdot \frac{R_1 R_2}{R_1 + R_2}$ (1.16)

where A_H is Hamaker constant and *D* is the distance between interacting surfaces.[5]

van der Waals force *F* between crossed cylinders of radius *R*, as in the case of SFA, is same as the force between sphere of radius *R* and a flat plane surface. According to *Derjaguin* approximation, this force equals the free energy *E* of interaction per unit area between two plane parallel plates of the same material.[4] Specifically, $F = 2\pi RE$ where *R* is the geometric radius of curvature of the surfaces. For this reason the force *F(D)* measured by SFA is generally plotted as F/R and is therefore implicitly related to the interaction free energy *E(D)* per unit area between parallel plates. For mica interacting across vacuum or air, the Hamaker constant, $A_H = 10 \times 10^{-20}$ J.[4] Mica was used as the substrate in all the SFA experiments performed in this work.

Electrostatic double-layer forces

Near the charged surface there is an accumulation of counterions and depletion of co-ions. The co- and counterions together with charged surface are called the electric double-layer. The electrostatic double-layer forces are always present between charged surfaces in water, due to water dissociation ($H_2O \leftrightarrow H^+ + OH^-$). The electrostatic double-layer force decays exponentially as a function of the surface separation *D* when *D* is

larger than the Debye length, κ^{-1}, that depends on dielectric properties (ε) and the ionic strength (I) of the medium.

$$\kappa^{-1} = \sqrt{\frac{\varepsilon\varepsilon_0 k_B T}{e^2 I}}, \qquad I = \sum_i c_i Z_i^2 \tag{1.17}$$

where ε_0 is the permittivity of the vacuum, e is the unit charge, c_i is the bulk concentration and Z_i is the valency of the ion i, summing over all ions present. As can be seen from equation (1) the Debye length is shorter at higher ionic strengths. For monovalent ions in aqueous solution at 25º C, the Debye length is given by:

$$\kappa^{-1} \approx \frac{0.304}{\sqrt{C}}, \qquad C = \sum_i c_i \tag{1.18}$$

where C is concentrations of ions and κ^{-1} is in nanometers.

The electrostatic double layer force $(F_{DL}(D))$ between two spheres of same material with radius R_1 and R_2 at low surface potentials ψ < 25 mV, can be expressed as: [4]

$$F_{DL}(D) = 4\pi \frac{R_1 R_2}{R_1 + R_2} \varepsilon\varepsilon_0 \kappa \psi^2 e^{-\kappa D} \tag{1.19}$$

where ε is dielectric constant and κ is the reciprocal of Debye length (Eq. 18). In the limit of small surface potential ψ, the following equation due to Grahame can be used to link ψ with the surface density of charges σ, $\sigma^2 = 2\varepsilon\varepsilon_0 kT(\sum_i \rho_{0i} - \sum_i \rho_{\infty i}) =$ $2\varepsilon\varepsilon_0 kT \sum_i \rho_{0i}(e^{-Z_i e\psi_0/kT} - 1)$, where $\rho_{0i} = \rho_{\infty i} e^{-Z_i e\psi_0/kT}$ is the ionic concentration of ions at the surface, at x=0.[4]

1.6 Protein studies with the surface force apparatus

The SFA was first implemented by Tabor and Winterton,[6] further developed by Tabor and Israelachvili,[6] and later modified by Israelachivili and Adams[6] to measure surface forces in fluids. SFA enabled the direct measurement of static and dynamic forces between surfaces as a function of their separation. It provided the first direct experimental verification of the DLVO theory for surface interacting in dilute electrolytes as well as surface hydration and hydrophobic forces, and has been successfully used to study polymers and proteins,[9,10] notably mucins.[11,12] The following section describes the SFA technique which was predominantly used to acquire most of the experimental data presented in this work. It is follows by the description of experimental protocol, procedure of force measurements and distance measurements in the SFA technique.

In this thesis we used a SFA Mk III distributed by Surforce LLC, USA (Fig. 1.6, 1.7). The setup was developed in 1985-1989 by Isrealachvili and McGuiggan.[13] SFA distinguishes itself from other nanoscale measurement instruments like Atomic Force Microscope (AFM) by its ability to measure distance over several orders of magnitude ranging from Angstrom level up to tens or even hundreds of microns. Unlike AFM, SFA measures forces between two surfaces rather than between surface and tip. Distance between two surfaces can be controlled using series of motors and actuators.

Section 1.6.1 describes SFA design and differential and fine micrometers with which SFA Mk III is equipped. SFA measurements were carried out on mica surfaces. Section 1.6.2 deals with the properties of muscovite mica, which was used as the substrate in all

SFA experiments. Multiple-beam interferometry is used to directly measure distance *D* between two macroscopic cylindrical surfaces arranged in crossed-cylindrical geometry. Section 1.6.3 describes the lens and sample configuration and equations that were used to calculate *D* using three-layer interferometer typically used in SFA setup. Sections 1.6.4 and 1.6.5 deal with experimentally measuring normal forces using SFA and experimental procedures, respectively.

1.6.1 SFA design

The photograph and the schematic drawing of SFA Mk III is shown in Fig. 1.6 and Fig. 1.7, respectively.

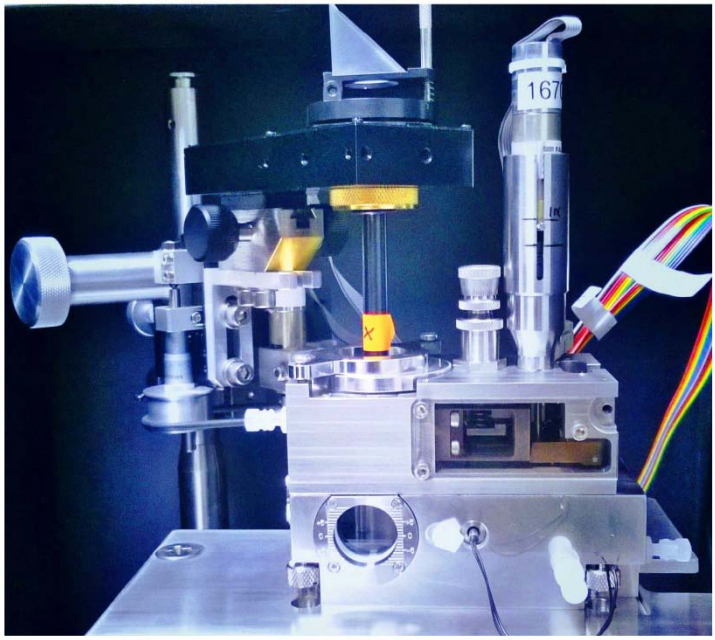

Figure 1.6. Photograph of SFA Mk III with optics stand.

The apparatus consists of two units: an upper (control) chamber comprising the surfaces, distance controls and force measuring springs and a lower (bathing/liquid) chamber

which acts a simple bath that can be filled with liquid. The base of the upper chamber is coupled to the lower chamber and the design is such that the lower chamber is completely sealed from the mechanical controls of the upper chamber.

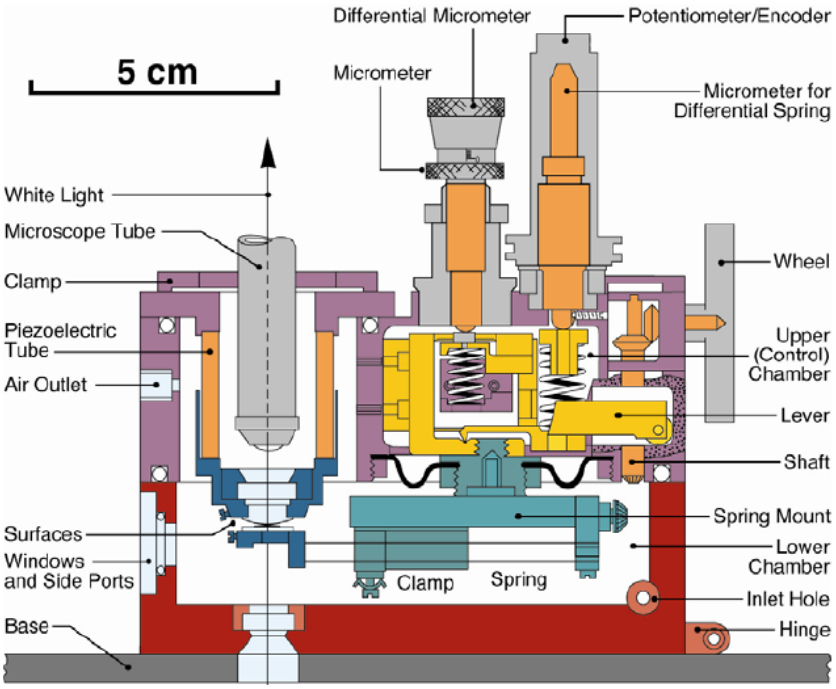

Figure 1.7. Schematic drawing of SFA Mk III showing key parts.

The basic idea underlying the SFA technique is the direct measurement of forces by the bending of cantilever springs to which the sample surfaces are attached. The lower surface is attached to a double cantilever spring with elastic constant *k*. A multiple-beam interferometry (Section 1.3.4) is used to directly measure *D* and the deflection *L* of this force-measuring springs, that is proportional to the normal force $F=kL$ acting on the surfaces. The upper surface is attached to the piezoelectric crystal tube that is in turn rigidly connected to the upper frame of the SFA. Since the piezoelectric tube can be

moved laterally and rotated before it is clamped tightly to the upper frame of the apparatus, the upper surface can actually be moved, which helps in making optical adjustments and finding and changing the contact position.

To meet the goal of high positioning accuracy with large enough travel range of few millimeters necessary to mount the surfaces, the surface separation in SFA Mk III is controlled by the four-stage distance control mechanism which is carefully tuned to provide necessary range and resolution.[13] In a typical experiment, the upper surface can be displaced by using a piezoelectric element, while the lower surface is mounted at the end of the double cantilever spring that can be moved to bring the surfaces to a given separation. Double cantilever springs are preferably used over single leaf springs in order to minimize the tilting and/or sliding between the surfaces when the spring is deflected.[14]

There are three mechanical distance controls to control the movement of the lower surface. Both a coarse and a differential micrometer act as coarse controls, while the third distance control is via a differential spring mechanism. Here a helical spring is compressed by a motor-driven non-rotating micrometer. The final, fourth distance control is non-mechanical control in which the upper surface is displaced by applying a voltage across the piezoelectric tube. Table 1.1 summarizes the operating principle, range, and resolution of the four distance controls.

The three micrometer controls, M1, M2 and M3 in Table 1.1 are conveniently positioned for manual control, but any one of them can be controlled by a variable-speed reversible

DC motor. The displacement of the spring in M3 can be measured from a encoder attached to the top of M3.

CONTROL	OPERATION	RESOLUTION	RANGE
Normal micrometer (M1)	Manual	500 nm	± 3 mm
Differential micrometer (M2)	Manual	50 nm	± 50 μm
Differential spring (M3)	DC-motor	1 nm	± 2.5 μm
Piezo control	High voltage	<0.1 nm	± 0.5 μm

Table 1.1 Distance controls in the SFA Mk III

1.6.2 Mica surfaces

In the typical SFA experiment, two mica sheets with equal thickness *T* ranging from 1 to 5 micron are glued to cylindrical silica lenses. Mica has been the choice material for SFA studies over the past 20 since its introduction by Bailey and Courtney-Pratt[15] due to its unique properties. It is relatively easily cleaved into large thin sheets of a very uniform thickness with an area of several square centimeters. The surface of the cleaved mica is so smooth that is called "atomically smooth" substrate. Furthermore, mica is transparent, flexible, has a high shear and tensile strength, and is chemically inert in most liquids. Thin cleaved mica sheets placed on a base sheet are mechanically and chemically stable to withstand further handling and processing.Cleaving of defect free sheets can be achieved by inserting a sharp tip of pointed tweezers into a thick sheet of muscovite mica. Once thinned down to desired thickness by repeated cleavage, small rectangular sheets (10 X 10 mm^2 in size) are cut out by melt cutting by using a hot platinum wire of

diameter 0.2 mm. Melt cutting is used to avoid mica flakes that readily deposit of freshly cleaved mica.

Mica is a crystal belonging to the family of layered silicates (Fig. 1.8). SFA experiments generally use the most abundant variety of mica with chemical composition: $KAl_2(AlSi_3)O_{10}(OH)_2$.The covalently bound alumosilicate layers are separated by potassium ions. The basal plane, presented in Fig. 1.8(b), is composed of SiO_4 and AlO_4 tetrahedrons linked by their corners. In the basal plane the ratio of silicon to aluminum is 3:1. Thus, roughly 25% of tetrahedrons has aluminum central atoms. Since aluminum carried formal charge of +3 vs. +4 of silicon, the

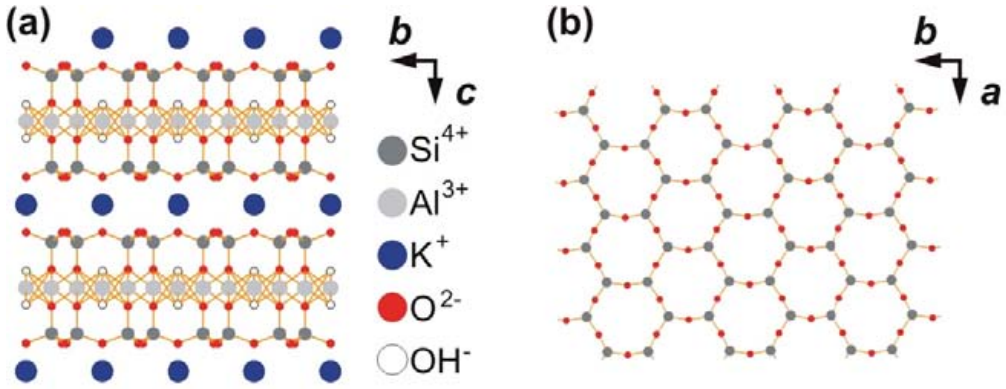

Figure 1.8: Schematic representation of the muscovite mica crystal structure. Vectors *a* and *b* define the {001} planes, vector *c* is the surface normal vector. (a) Side-view (projection onto the *a*-axis) exhibiting aluminosilicate layers separated by electrostatically bound interlayer potassium ions. (b) Hexagonal arrangement of the {001} surface top layer (projection onto the *c*-axis) exhibiting Si (partly Al) and O atoms of a cleaved mica surface, residual potassium ions are not displayed. Figure adapted from ref. [16].

replacement of the silicon by aluminum atoms create negative lattice charge, which is compensated by the K^+ ions between aluminosilicate sheets, as shown in the model

structure of Fig.1.8(a).[16] These K^+ are only bound electrostatically. This ionic binding between potassium and oxygen is much weaker than the covalent bonds between the aluminosilicate layers, and muscovite mica can therefore be cleaved along the basal plane creating molecularly smooth, defect-free surfaces.[17] Upon cleavage along the basal plane the potassium ions are evenly distributed between the two new surfaces, which have zero net charge. It has been claimed that upon cleavage the atomic structure of the aluminosilicate layers is undisturbed while the potassium layer is disrupted.[18] Therefore, a cleaved mice surface exhibits a hexagonal arrangement of Si (partly Al) and O atoms, as illustrated in Fig. 1.8(b).

If the mica sheet is immersed in water or other polar solvents, the potassium ions dissociate rendering the surface negatively charged the total number of negative lattice sites on the mica basal plane correspond to one negative charge per 48 Å^2 or 2.1×10^{14} charges per cm^2 when complete dissociation occurs. Hence, the hydrophilic nature of mica surface.

Muscovite mica is a monoclinic crystal, is optically biaxial and thus has three principal indices of refraction. Two of them, β and γ are within the cleavage plane and typical values for the refractive indices are as follows:

$\mu_\gamma = 1.5846 + 4.76 \cdot 10^5 / \lambda^5 (\text{Å})$, $\mu_\beta = 1.5794 + 4.76 \cdot 10^5 / \lambda^5$ (Å), giving

$$\mu_{mean} = 1.5820 + 4.76 \cdot 10^5 / \lambda^5 (\text{Å}) \qquad (1.20)$$

for red and brownish micas, and

$\mu_\gamma = 1.5953 + 4.76 \cdot 10^5 / \lambda^5 (\text{Å})$, $\mu_\beta = 1.5907 + 4.76 \cdot 10^5 / \lambda^5 (\text{Å})$, giving

$$\mu_{mean} = 1.5930 + 4.76 \cdot 10^5 / \lambda^5 (\text{Å}) \quad (1.21)$$

for greenish micas.

By using the appropriate values of refractive index of mica together with the equations derived for three-layer interferometer (see section1.6.3), the distance *D* between two surfaces and the medium refractive index μ can be determined. .

SFA III measures the forces between two surfaces in vapors and liquids with a force sensitivity of 10 nN and a distance resolution of 0.1 nm. Optical interferometry also provide a measure of radius of curvature *R*, refractive index of the medium between two surfaces, surface deformations arising from surface forces, molecular orientations in thin films, dynamic interactions like viscoelastic and frictional forces, and other time-dependent phenomenon in real time.

1.6.3 Distance measurements: multiple-beam interferometry

Optical interferometry provides a method for measuring the thickness and refractive index of transparent thin films.[19] Immediately after cleaving and cutting, mica sheets are placed face down onto the baking sheet. After less than 48 h, they are coated with a 55 nm layer of silver using thermal evaporation or chemical sputtering technique. This thickness of silver coating gives a good compromise between sharpness and intensity of the interference fringes.

The distance between two surfaces and the refractive index of the film confined between two mica sheets is measured by monitoring the fringes of equal chromatic order (FECO)

using a spectrometer. Identically thick and flat mica sheets, each coated with a thin reflective layer of silver, glued onto two cylindrical glass support discs in a crossed-cylinder orientation (Fig. 1.9) imitates a single asperity contact know as the point of closest approach (PCA).

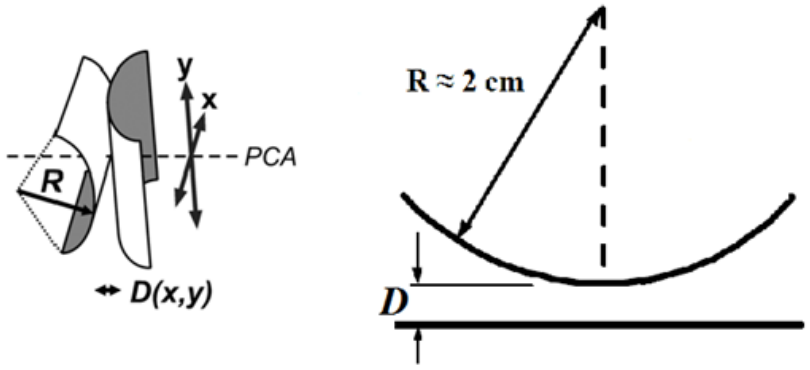

Figure 1.9. Geometry of two crossed cylinders used in SFA. Note that this contact geometry is equivalent to a sphere of radius R approaching a flat surface.

The protein coated discs are placed in cross cylinder geometry and the measured radius of curvature for each contact position is used to normalize the measured force, *F(D)* to enable quantitative comparison between different contact positions and experiments. The force *F(D)* measured between two curved surfaces can be directly related to energy per unit area *W(D)* between two flat surfaces at the same separation, *D*, using Derjaguin approximation[20] under the assumption that *D* is much smaller than the radius of curvature R (*D* << *R*),

$$E(D) = \frac{F(D)}{2\pi \cdot R}. \qquad (1.22)$$

Furthermore, the partially reflective silver mirrors at the back side of the mica surfaces together with the intervening medium forms a symmetrical three-layer interferometer, as shown in Fig. 1.10.

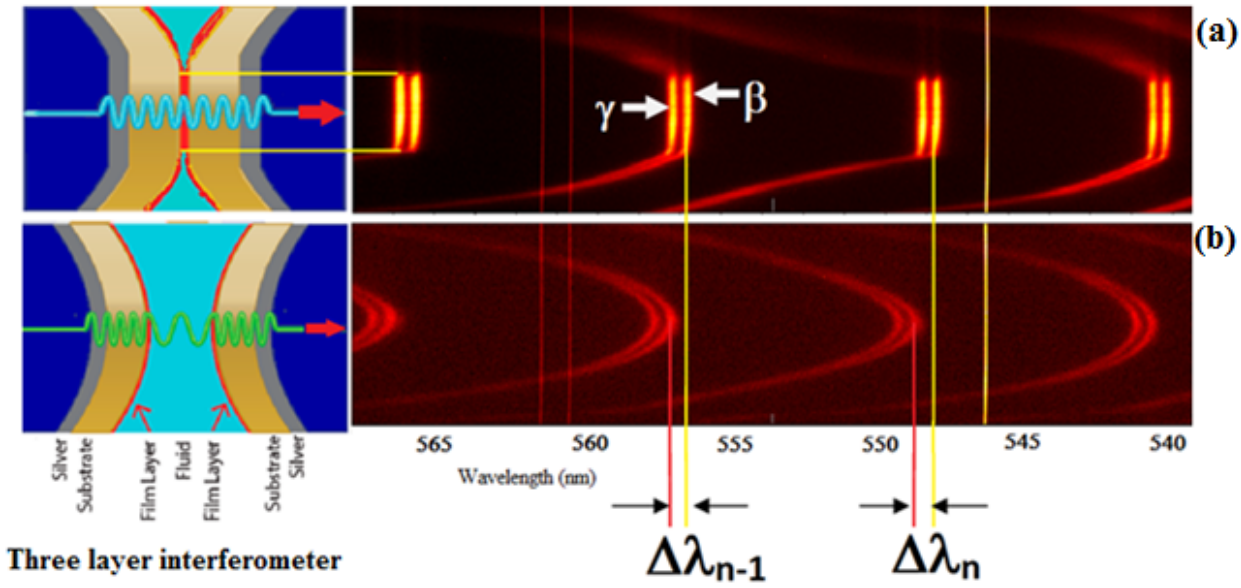

Figure 1.10. Example of spectral images with surfaces (a) in compressed contact and (b) with surfaces separated. To the left of panel a and b is the illustration of interferometer. White light collimated and shone through the assembled interferometer transmits whole-order wavelengths called fringes of equal chromatic order (FECO).

When the white light is passed through the surfaces, a discrete set of wavelengths is transmitted, corresponding to constructive interference in the interferometer. When the two mica surfaces are in direct adhesive contact in air (D = 0) the wavelengths λ_n^0 are recorded, where n =1,2,…is the chromatic order. When the surfaces are separated by a distance D, the transmitted wavelengths are red-shifted according to the formula

$$\tan\left(\frac{2\pi\mu D}{\lambda_n^D}\right)=\frac{2\bar{\mu}\sin[\pi(1-\lambda_n^0/\lambda_n^D)/(1-\lambda_n^0/\lambda_{n-1}^0)]}{(1+\bar{\mu}^2)\cos[\pi(1-\lambda_n^0/\lambda_n^D)/(1-\lambda_n^0/\lambda_{n-1}^0)]\pm(\bar{\mu}^2-1)} \tag{1.23}$$

where the sign "$\pm$" refers to the odd or even fringe order, respectively and $\bar{\mu}=\mu_{mica}/\mu$, where μ_{mica} is mica the refractive index and μ is the medium refractive index at λ_n^D. The order is given by the formula:

$$n=\frac{\lambda_{n-1}^0}{\lambda_{n-1}^0-\lambda_n^0}. \tag{1.24}$$

By using Eq. 1.23 and 1.24, both *D* and μ of the medium can be determined independently by measuring the wavelengths of at least two odd and an even fringes. The distance *D* is generally measured by following the motion of an odd fringe throughout the experiment because λ_n^D does not depend on μ for small values of *D*. Using this technique, the accuracy on *D* is often as good as 1 $\mathring{A}$.

Mica has properties of a negative biaxial crystal.[21] In SFA, direction of light propagation coincides with the axis α of refractive index of mica (Fig. 1.11) and when the crystallographic axes of the two mica sheets are parallel to each other, $\lambda_\gamma > \lambda_\beta$ and the resulting FECO appears as doublet (Fig. 1.11a). Whereas, when the crystallographic axes of the two mica sheets are perpendicular to each other, $\lambda_\gamma = \lambda_\beta$ and FECO appears as singlet (Fig. 1.11b).

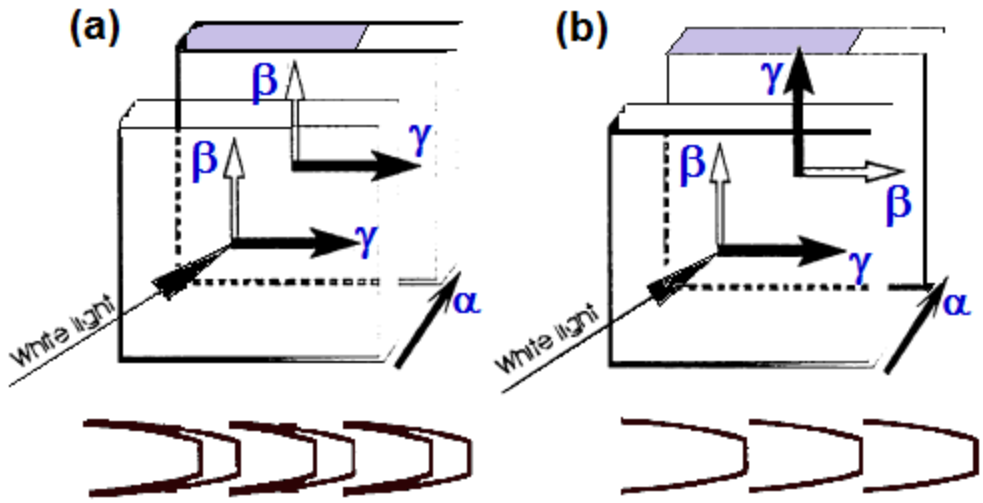

Figure 1.11. Schematic representation of FECO observed for (a) parallel and (b) perpendicular orientation of the crystallographic axes of mica sheets.

Simultaneous recording of at least one pair of odd and even fringes allowed to determine the refractive index *n* averaged acrossthe surface separation *D*. In the presence of a solute in a liquid film with known refractive index n_C, the average solute concentration *c* can be calculated as $c=(n-n_c)(dn/dc)$.[22]

1.6.4 Normal force measurements

Normal forces are measured by moving one of the surfaces by an amount Δz using one of the actuators (micrometers or piezo) while monitoring the change in surface separation ΔD which is measured by MBI. The deflection of the double cantilever spring is $L = \Delta z - \Delta D$ and the change in force between surfaces is simply given by Hooke's law,

$$\Delta F = k(\Delta z - \Delta D) = kL \text{ where } L = \Delta z - \Delta D \qquad (1.25)$$

When the surfaces are separated by a large distance, ΔF = 0, since $\Delta z = \Delta D$ and the surface position *z* (in arbitrary units) can be precisely calibrated in nm using a simple linear interpolation *z* vs *D*. The case $\Delta z = 0$ corresponds to a 'hard wall' repulsion, namely *dF/dD*= -∞.

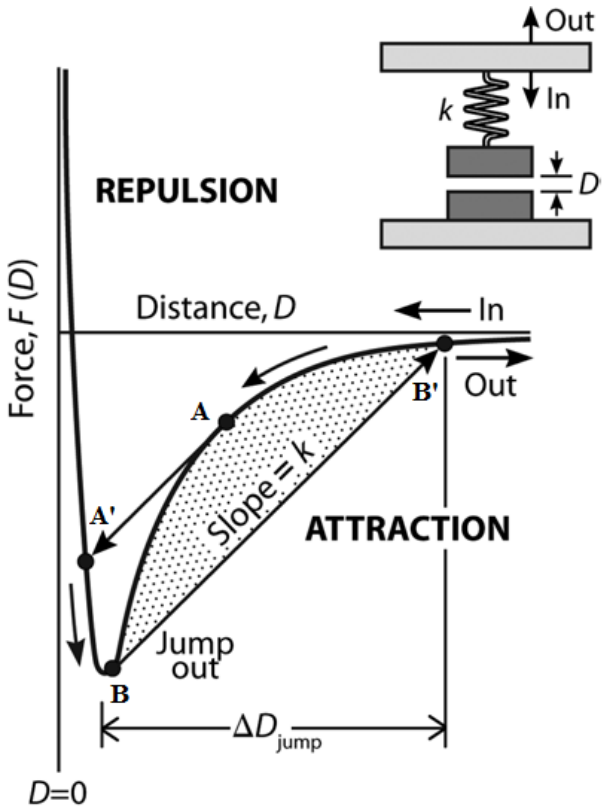

Figure 1.12. Schematic attractive force law measurement by force-measuring spring system. If the gradient of the attractive force *dF/dD* exceeds the gradient of the springs restoring force defined by spring constant *k*, the surfaces will jump from A into contact at A' while approaching, while on separating the surfaces, they will jump from B to B'. The distance (B - B') multiplied by *k* gives the adhesive force, F_{ad}, i.e. the value of F at B.

Spring-based force measurements are inherently unstable at distances *D* such that $dF/dD > k$ (Fig. 1.12). Therefore, quickly increasing or decaying forces are inaccessible. Due to this mechanical instability, the lower surface mounted on the double-cantilever force spring will either jump towards or away from the upper surface to the next stable region during approach or separation, respectively. Thus using weaker springs are more sensitive and can result in more inaccessible regions of the complex force profile because of increased range between instabilities.

1.6.5 Experimental procedure

Mica sheets are glued on cylindrical silica lenses which act as optical window and support for mica during the measurements. The lenses are placed on heating plate and a grain of thermosetting EPON RESIN 1004 resin (from Shell) is placed on the glass, melted and spread in a thin uniform layer. Mica is then glued with the silvered face down avoiding overheating, which may lead to degradation of silver film, and bubbles trapped below the mica. The lenses with the glued mica surfaces are then mounted in SFA, the SFA chamber is closed tightly and a stream of nitrogen is passed in the chamber to remove adsorbed ambient water from the surfaces.

Optical alignments of the lamp and lenses are checked and optimized before bringing the surfaces in contact in air for the first time. This alignment will help the white light to pass perpendicularly through the mica surfaces mounted in the SFA. With the help of the eyepiece placed on the microscope objective (Fig. 1.13), a contact position is determined and fixed. This contact position will be observable in monochromatic light as a ring-

shaped interference pattern (i.e. Newton's rings) (Fig. 1.13b) coming from the crossed cylinder semi-reflective surfaces. Then the light path is established with the help of the prism so that the FECO can be resolved in the eyepiece of the spectrometer.

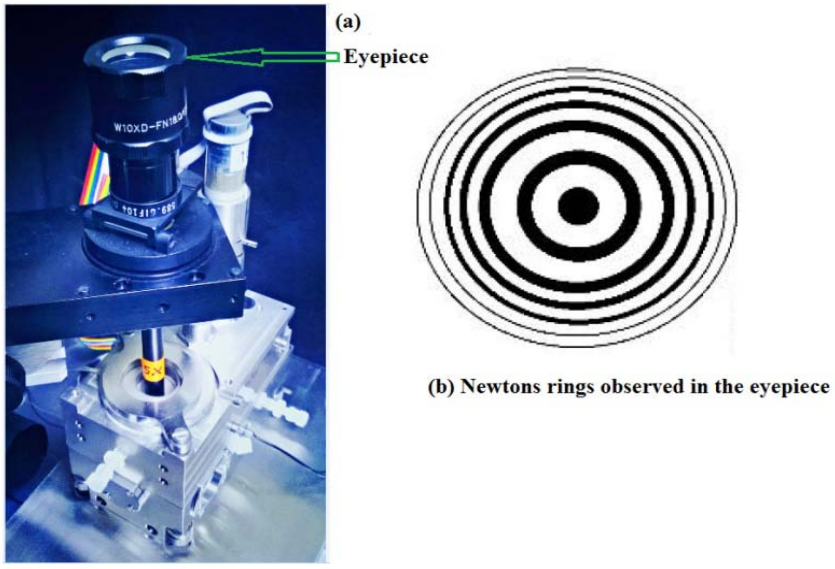

Figure 1.13. (a) SFA with eyepiece placed on microscopic objective to fix a contact position. (b) Circular fringes (Newton's rings) where dark fringes correspond to destructive interference occurring when path difference, $2T = n\lambda$ and bright fringes correspond to constructive interference occurring at path difference, $2T = (n+1/2)\lambda$.

Contact of the surfaces is achieved by bringing the surfaces close to each other with the help of the rough and fine motor driven micrometer of the SFA until the fringes stop moving and the tip of fringe flattens. The flattening occurs only when the mica surfaces are in strong adhesive contact in air due to deformation of glue layer. When the surfaces are separated, the shape of the fringes become parabolic. The pattern, shape and

sharpness of the fringes depends upon the thickness of the mica surfaces and how well the cross cylindrical lenses are aligned with respect to each other.

With the help of a spectrometer and a Hg-Ar^+ pencil lamp producing spectral lines of the know wavelength, the proper calibration for wavelengths $\lambda_n^0, \lambda_{n-1}^0$ and λ_{n-2}^0 transmitted through the contact position is obtained. Typically, the position of three consecutive fringes ($\lambda_n^0, \lambda_{n-1}^0$ and λ_{n-2}^0) are recorded. If the contact position is not satisfactory, the surfaces are receded and the new contact position is established by moving the top surface slightly with respect to the lower one. The experiments in solution can be performed in two different ways, either by filling up the bath with solvent/buffer where the surfaces are completely immersed in liquid or by just injecting a droplet between two surfaces. Using a bath have some advantages over injecting a droplet between the surfaces as it minimizes thermal drifts and eliminates unwanted forces due to surface tension of the drop. However, for most of the experiments performed in this work, the liquid drop injection method was used since the amount of samples used were limited.

The SFA experiments were performed in a dark room in the basement. The SFA was installed on a vibration-free table to avoid noise in the force measurements and in a thermostated room to reduce thermal drifts. The apparatus was covered with a simple 1-cm thick plexiglass box which ensures a crude thermal isolation and sound vibration isolation.

Forces are measured by the SFA over molecular-scale distances and hence great care has to be exercised to avoid any surface contaminations, which may arise from various

sources like dust particles, fingerprints and any contaminant left from the earlier experiment. Therefore, all the manipulations are done in a laminar-flow cabinet, including cleaning of the apparatus and glass lenses, and gluing of the mica sheets to the lenses. All tools are cleaned in ethanol before use and tools coming in contact with glue are routinely cleaned with chloroform. The glassware is washed in distilled water and the rinsed with ethanol. The glass lenses are stored in chloroform after they are used in SFA experiments since the glue is soluble in chloroform.

1.7 Pin-on-disk tribometry

Pin-on-disk tribometry was used during the visit at DTU-Copenhagen to investigate lubrication and frictional properties of protein and protein-polymer mixtures. The pin-on-disk tribometer is a technique to measure the sliding friction on macroscopic scale for sphere-on-plane configurations where the pin and disk represents sphere and plane respectively. The characteristic parts of the instrumental setup are illustrated in Fig.. 1.13. The disk is mounted inside a cup holder . The pin is loaded by dead weights to apply a normal force or load F_{Load} and is brought into contact with the disk. Interfacial friction force, $F_{Friction}$, between a loaded pin sliding in contact with the disk is measured by the lateral deflection of a strain gauge in the measuring arm.[23] The friction coefficient (μ) was calculated as $\mu = (F_{Friction}/F_{Load})$. Wide range of samples can be readily employed in the pin-on-disk tribometer and the available sliding speeds typically range from mm/s to

cm/s which allows investigating several lubrication regimes from fluid film to boundary lubrication.

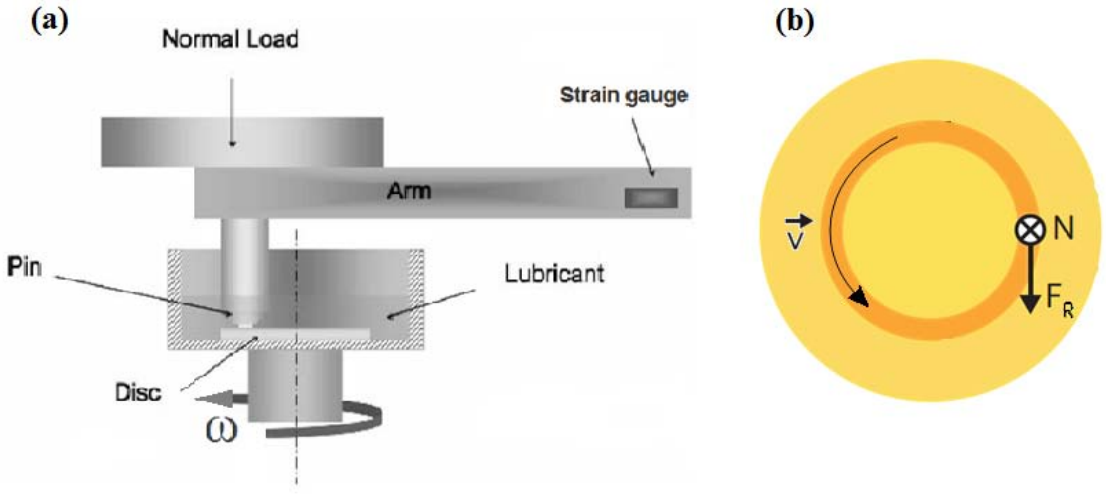

Figure 1.13. (a) Schematic representation of pin-on-disk tribometer and (b) top view of the rotating disk.

We used a pin-on-disk tribometer from CSM Instruments SA, Peseux, Switzerland. Poly(dimethyl siloxane) (PDMS) was employed to prepare pins and disks in all the pin-on-disk tribometry experiments. The PDMS pins and disks were prepared from the Sylgard 184 silicone elastomer kit (Dow Corning, Midland, MI). The base and the curing agent/cross-linker were thoroughly mixed at a ratio of 10:1 ratio by weight. The foams generated in the mixture were removed by applying a gentle vacuum. In order to prepare PDMS disks, machined aluminum plate moulds with the flat base designed to dimensions (40 mm diameter x 5 mm thickness) were employed. All tribological measurements were made with the PDMS disk side exposed to the ambient during the curing process. The PDMS pins with the hemispherical ends were molded in a commercially available 96 Microwell plate with the round-shaped wells (radius = 3 mm, NUNCLON Delta Surface,

Roskilde, Denmark). The mixture was transferred into these moulds and incubated in an oven at 70° C overnight. Tribological measurements were conducted at room temperature (RT). The load on pin was set to F = 1N in all experiments. The range of sliding speed **v** in all the experiments were from 0.25 to 100 mm/s. The number of laps was at least 20 for each measurement and error bars in μ vs. sliding speed plots designate standard deviation from the average over number of laps of measurement of μ in the same track.

1.8 Optical waveguide lightmode spectroscopy

Optical waveguide lightmode spectroscopy (OWLS) was used at DTU-Copenhagen to study adsorption and determine the surface mass density of proteins, polymers and protein-polymer mixtures adsorbed on a surface. OWLS is based on multiple total internal reflections and allows in situ measurement of the surface immobilization of biomolecules in aqueous environment onto the surface of a waveguide sensor chips.[24] The waveguide comprises of glass substrate coated with thin, optically transparent metal oxide film (200 nm thick $Si_{0.25}Ti_{0.75}O_2$ layer on 1 mm thick AF 45 glass, Microvacuum Ltd, Budapest, Hungary) with a diffraction grating embossed into its surface. Linearly polarized light from He-Ne laser is coupled into the waveguide by the means of the grating.

The four layer model depicting the sensor chip and the flowcell is shown in Fig. 1.14. The sensor chip with waveguide film material $Si_{(1-x)}Ti_xO_2$ was used which is depicted as layer F in Fig. 1.14.Due to total internal reflection at the film-substrate (F, S) and film

adlayer (F, A) interfaces, light is confined inside the film as it propagates in the x direction. Total internal reflection occurs at the film-substrate and film-adlayer interfaces provided (i) the refractive index of the film is higher than that of the substrate and adlayer and (ii) the propagation angle, ϕ_b, incident on the film at the F-A and F-S interfaces is greater than or equal to the critical angles, ϕ_c, at each of the two interfaces.

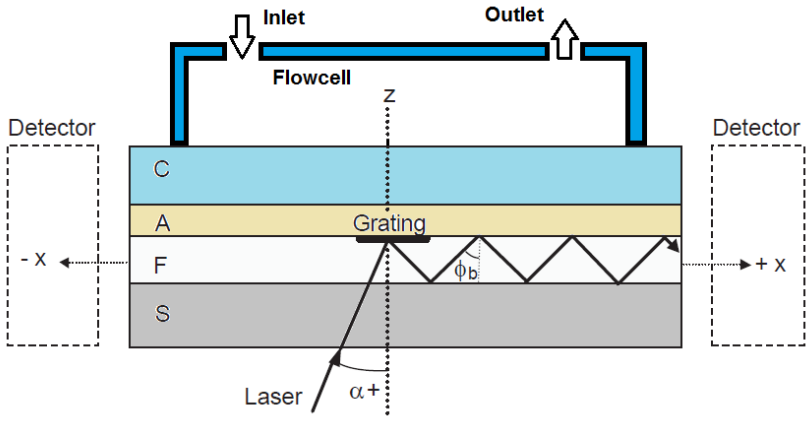

Figure 1.14: The physical configuration of OWLS. The sensor chip is depicted as a three layer planar dielectric waveguide: (S) is a glass substrate, (F) is a waveguiding thin film onto which a diffraction grating is embossed, (A) is adsorbed protein layer and (C) is solution-state protein that is incontact with the film at the grating region.The angle of incidence at which light is maximally coupled into the waveguide varies with the effective refractive index of the waveguide.

Polarized light from He-Be laser is directed onto the sensor chip. The sensor chip is rotated during an angular scan and the photodiodes/detectors measure the intensity of light coupled out of the faces of the sensor chip. The computer records the angular peak position of light power as a function of incident angle of the laser beam onto the chip.

The incident angle of the laser beam onto the sensor chip at which light is maximally coupled into the waveguide are the basic physical values determined by the OWLS. As protein adsorbs onto the film surface of the sensor chip, the angles changes due to the formation of protein adlayer. A computer tracks the values of the incoupling angles with time. Since OWLS measurements depend on the refractive index contrast between particle-free and particle-containing solvent, the measured adsorbed mass includes the mass of particles but not that of the solvent between the adsorbed particles. Since the refractive index is a linear function of the concentration over a wide range of concentrations, the absolute amount of adsorbed molecules can be calculated using de Feijter's formula:[25]

$$M = d_A \frac{n_A - n_C}{dn/dc}, \tag{1.26}$$

where d_A is the thickness of the adsorbed layer and (dn/dc) is the refractive index increment of the molecules. The surface adsorbed mass densities determined from Eq. 1.26 depend only on the difference in the refractive index of the adsorbed molecules (n_A) and the cover medium (n_C); thus the solvent molecules do not contribute to the mass.

OWLS experiments were carried out using OWLS 210 high sensitivity (~ 1 ng/cm^2), label free biosensor system. Waveguides used in this work were spin-coated with an ultrathin layer (~ 30 nm) of polystyrene (PS) (Sigma Aldrich, Brondby, Denmark), 6 mg/ml in toluene at 2500 rpm for 15 s followed by ultrathin layer of PDMS. The base and curing agents of the silicone elastomer (Sylgard 184 elastomer kit, Dow Corning,

Midland, MI) were dissolved in hexane at a ratio of 10:3 (final concentration, 0.5 % w/w). This solution is spin-coated onto a waveguide at 2000 rpm for 25s, and cured in an oven at 70 °C overnight. The thickness of spin-coated PDMS layer was approximately 20 nm as measured on silicon wafer by ellipsometry.[26] The PS/PDMS coated waveguide sensor chips were equilibrated in PBS overnight. In OWLS, it is usually necessary to achieve a steady baseline in a particle/protein free buffer solution before injecting the sample solution.

100 µL of sample solution was injected via the loading loop of the flow-cell of OWLS. Adsorption was allowed for 15 minutes for all the samples on PS/PDMS coated sensor chips followed by 30 minute rinse with protein-free buffer solution. A syringe pump (Model 1000-NE, New Era pump Systems, Inc., NY) was employed to transport buffer solutions through the flow-cell containing the waveguide surface. The value for the refractive index increment, dn/dC, of various samples with respect to varying concentration, C was experimentally determined using an automatic refractometer (Rudolph, J157). Due to the significant dependence of refractive index on temperature, the flowcell at maintained at 25 ± 0.5 ºC.

1.9 Dynamic light scattering

Dynamic light scattering (DLS) was used at DTU-Copenhagen and NTU-Singapore to measure hydrodynamic diameters of mucins, polymers, mucin-polymer mixtures and *P. viridis* mussel foot proteins (Pvfps).

Dynamic light scattering is one of the most powerful and popular technique used to determine the size of particles in range from about 0.001 to several microns. Dynamic light scattering (DLS) measures time-dependent fluctuations in the scattering intensity arising from particles undergoing random Brownian motion. Diffusion coefficient and particle size information can be obtained from the analysis of these fluctuations.

When the beam of light passes through a colloidal dispersion, the particles scatter some of the light in all directions. Small particles suspended within a liquid undergo Brownian motion which causes nonuniform distribution of scattering centers and fluctuations of their concentration. Correspondingly, the intensity of the scattered light detected at an angle θ undergoes temporal fluctuation around the mean value $<I_s>$, also called time averaged scattered intensity. The kinetics of the intensity fluctuations depends on the diffusion coefficient of the particles, which in turn is related to their size. Smaller and rapidly diffusing particles produce rapid fluctuations, while large and slowly moving particles causes slow fluctuations. The dynamic light scattering (DLS) technique analyses the rapidity of the fluctuations by the means of autocorrelation function, such as the normalized temporal autocorrelation function of the scattered field amplitude, $g_1(Q,\tau)$, which is a function of scattering vector Q and the time difference between the correlated points τ. $g_1(Q,\tau)$ is related to the diffusion coefficient, D, of the scattering particles via Siegert relation:[27]

$$g_1(Q,\tau) = 1 + e^{-2DQ^2\tau} \qquad (1.27)$$

Once the diffusion coefficient, D, is known, the Strokes-Einstein equation can be used which relates the diffusion coefficient, D, to the inverse of the particle hydrodynamic diameter, d_H:

$$D = \frac{k_B T}{3\pi\rho d_H} \tag{1.28}$$

where k_B is Boltzmann's constant, T is absolute temperature and μ is the dynamic viscosity of the solvent. The hydrodynamic diameter is always slightly greater than the actual particle diameter, as it includes solvent molecule that are bound or coupled to the particle as it moves through the surrounding fluid.

Light scattering experiments were carried out with Brookhaven ZetaPALS instrument (Brookhaven Instruments Corporation, Holtsville, New York) based on phase analysis light scattering via ZetaPALS particle sizing software. The light source is a laser beam with an incident wavelength of 658 nm. The standard protocol was followed for sample preparation. Prior to analysis, measurement cuvettes are cleaned with DI-water and ethanol and stored dry. 1.7 ml of unfiltered sample solution was placed into clean and dried plastic cuvette. The DLS instrument analyzed each sample for at least three runs at 5 minutes per run. The multiple runs resulted in a combined output reading for d_H, which is statistically more accurate than the mean reading from each individual run. A software “dust filter” was used for all of the runs and the measurements were performed at RT. The pH for all samples was readjusted to 7.2.

1.10 Zeta potential

Most colloidal dispersions in aqueous media carry an electric charge. This surface charge affects the distribution of ions around the particles and induce the formation of the so-called electric double layer. The double layer is formed in order to neutralize the charged particle and, in turn, it causes an electrokinetic potential between the surface of the charged particle and any point in the mass of the suspending liquid. This is referred to as the surface potential. The rigidly attached layer of counter ions to the charged particle is known as Stern layer and the adjacent layer to Stern layer where the charged atmosphere of counter ions exists is called the diffuse layer (Fig. 1.15).

The Stern layer and diffuse layer together are referred to as double layer. The boundary where the Stern layer and diffuse layer meet is usually defined as shear/slip plane. The electrical potential at this junction is related to mobility of the particle and is called the zeta potential. In other words, for a charged particle moving with respect to the solution phase, the potential at the shear surface, with respect to the bulk solution, is referred to as the zeta potential.[28] Although ζ is not the actual surface potential, in theoretical calculations, ζ is frequently taken to be identical to Stern potential, Ψ_δ.

One important parameter in the evaluation of the ζ is the value of pH of the suspension and the isoelectric point (IEP), which is defined as the pH at which the ζ is equal to zero.[29] The closer the pH is to the IEP, the smaller the magnitude of the ζ. Other

important parameters are the concentration of the non-specifically bound (or "indifferent") and specifically bound ions.

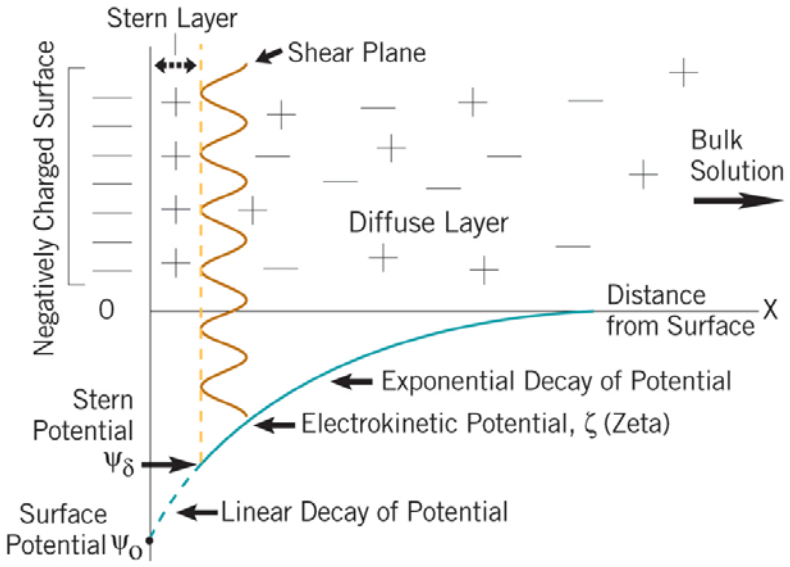

Figure 1.15: Simplified model of electric double-layer at a charged interface in aqueous solution.

ζ can be estimated by measuring electrophoretic mobility, in an electric field. The velocity, v of the particles moving in an electric field, E, gives the electrophoretic mobility, μ_E,

$$\mu_E = \frac{v}{E} \tag{1.29}$$

which in turn depends on the dielectric constant, ε, of the medium, the viscosity, η, of the medium, and the zeta potential, ζ:

$$\mu_E = \frac{v}{E} = \frac{2\varepsilon\zeta . f(\kappa a)}{3\eta} \tag{1.30}$$

The factor $f(\kappa a)$ accounts for the ratio between the particle radius, a, and the thickness of the double layer, $1/\kappa$. When the particle is much smaller than the double layer, then $f(\kappa a)$ = 1 (Hückel limit), while when the particle is larger than the double layer, as is the case when the ionic strength is high, then $f(\kappa a)$ = 1.5 (Smoluchowsky limit).[30]

The zeta potential was measured using ZetaPALS instrument (Brookhaven Instruments Corporation, Holtsville, New York) using zeta potential analyzer software. The disposable cuvettes and electrode were cleaned with millipore water and then with ethanol and blow dried. About 1.5 ml of sample was placed in the cuvette and then electrode is carefully placed in the cuvette avoiding any spillage. The electrode was always preconditioned in 0.5M KCl solution for one cycle consisting of 300 runs before starting measurements and all ζ measurements were recorded at pH 7.2.

1.11 Circular dichroism spectroscopy

Circular dichroism (CD) spectroscopy was used in DTU, Copenhagen to analyze protein-polymer interactions. Circular dichroism (CD) spectroscopy provides a low-resolution picture of the protein conformation and is widely used technique for characterization of proteins in solution. As proteins consists of amino acid residues which are optically active or chiral molecules, it exhibits optical activity and so CD. When a molecule is optically active, it has different refractive index for right- and left- circularly polarized light. Thus the molecule adsorbs right- and left- circularly polarized light to different extents.[31] This is called circular dichroism.

When the light passes through an absorbing optically active substance, the right- and left-circularly polarized rays travel at different speeds, $c_R \neq c_L$, which leads to unequal wavelengths, and given these facts, the two rays are also absorbed at different extents ($\varepsilon_R \neq \varepsilon_L$). The difference $\Delta\varepsilon = \varepsilon_R - \varepsilon_L$ is called as CD. The absence of regular structure results in zero CD intensity, while an ordered structure results in a spectrum which can contain both positive and negative signals.

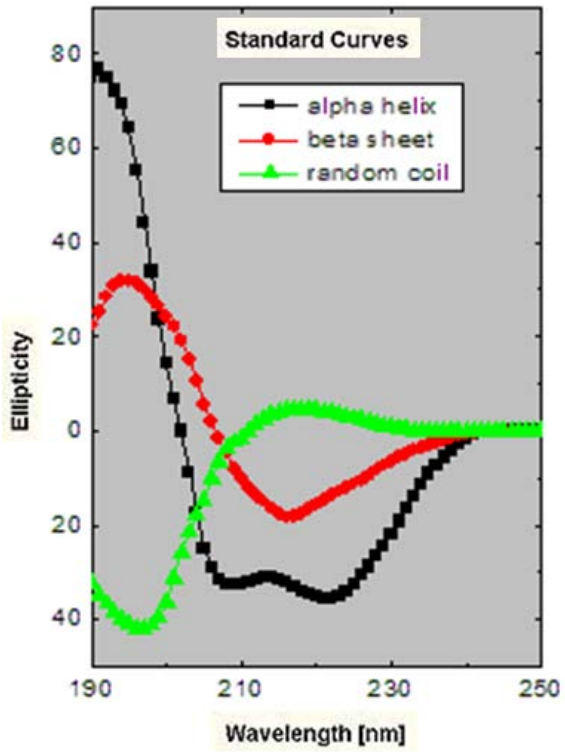

Figure 1.16. Far UV CD spectra associated with various types of secondary structure.

The chromophore which interacts with light is the amide bond. Far-UV spectra of proteins can be used to predict characteristics of their secondary structure (Fig. 1.16). This is based on the fact that isolated α-helices, β-sheets, and random coils possess

characteristic shape and magnitude of CD signal.[32] CD measurements of the amide bond adsorption in far-UV (190-230 nm) was done for the quantitative determination of secondary structures of protein. Far-UV CD spectra require 20 to 200 µl of solution containing 1 mg/ml to 50 µg/ml protein, in any buffer which does not have a high absorbance in this region of the spectrum.

The CD spectrum of a protein in the near-UV (240-400 nm) spectral region can be sensitive to certain aspects of tertiary structure.[32] At these wavelengths the chromophores are the aromatic amino acids and disulfide bonds, and the CD signals they produce are sensitive to the overall tertiary structure of the protein. If a protein retains secondary structure but no defined three-dimensional structure (*e.g.* an incorrectly folded or "molten-globule" structure), the signals in the near-UV region will be nearly zero. On the other hand, the presence of significant near-UV signals is a good indication that the protein is folded into a well-defined structure. The near-UV CD spectrum can be sensitive to small changes in tertiary structure due to protein-protein interactions and/or changes in solvent conditions. Near-UV CD spectra require about 1 ml of protein solution containing 0.25 to 2 mg/ml of protein.

CD spectra of mucin, polymer and mucin-polymer mixtures were acquired by using Chirascan photospectrometer. Rectangular quartz cuvettes with path length 0.5 mm and 10 mm were used for far UV and near UV measurements respectively. The photospectrometer is equipped with high energy lamp to generate UV frequencies which converts ambient oxygen to ozone which corrodes the optics of the instrument. So proper

amount of liquid nitrogen was purged through instrument for 15 minutes before turning on the lamp, during the entire measurement and 15 minutes after turning off the lamp. Far UV spectra were recorded in the region from 230 to 190 nm with a step size of 1nm, bandwidth of 1 nm, and time-per-point value of 0.5 s. Near UV spectra were recorded from 400 to 240 nm with a step size of 1 nm, bandwidth of 1 nm, and a time-per-point value of 0.5 s. One measurement was obtained from averaging three traces.

References

[1] Bhattacharjee, S. M.; Giacometti, A.; Martian, A. *Flory theory for Polymers*, **2013**, arXiv: 1308.2414v2.
[2] Doi, M; Edwards, S. F. *The Theory of Polymer Dynamics*, **1986**, Clarendon, Oxford, 317.
[3] Paananen, A. *On the interactions and interfacial behavior of biopolymers. An AFM study*, Espoo **2007**, VTT Publications.
[4] Israelachvili, J. N. *Intermolecular and Surface Forces*, 3rd ed.; Academic Press: London, **2011**.
[5] Hamaker, H. C. *Physica* **1937**, *4*, 1058-1072.
[6] Tabor, D.; Winterton, R.H.S. *Proc. R.Soc.Lond*. **1969**, A312, 435.
[7] Israelachvili, J. N.; Tabor, D. *Proc. R. Soc. Lund*. **1972**, A331, 19.
[8] Israelachvili, J. N.; Adams, *G. E. J. Chem Soc. Faraday Trans*. 1. **1978**, 74, 975.
[9] Zappone, B.; Ruths, M.; Greene, G. W.; Jay, G. D.; Israelachvili, J. *Biophysical Journal* **2007**, 92, 1693-1707.
[10] Klein, J. *Macromol. Chem. Macromol. Symp.* **1986,** 1, 125-137.
[11] Proust, J. E.; Baszkin, A.; Perez, E.; Boissonnade, M. M. Colloids and Surfaces, **1984**, 10, 43-52.
[12] Harvey, N. M.; Yakubov, G. E.; Stokes, J. R.; Klein, J. *Biomacromolecules*, **2011**, 12, 1041-1050.
[13] Israelachvili, J. N.; McGuiggan, P. M. *J. Mater. Res*. **1990, 5,** 2223-2231.
[14] Christenson, H. K. J. *Colloid Interface Sci*. **1988**, 121, 170-178.
[15] Bailey, A. I.; Courtney-Pratt, J. S. *Proc. R. Soc. London*, Ser. A **1955**, 227, 500-515.
[16] Ostendorf, F.; Schmitz1, C.; Hirth, S.; Kuhnle, A.; Kolodziej, J. J.; Reichling, M. *Nanotechnology*, **2008,** 19, 305705.
[17] Butt, H-J.; Graf, K.; Kappl, M. *Physics and chemistry of interfaces*; **2006,** Wiley.
[18] Muller, K.; Chang, C. C. *Surf. Sci.* **1969,** 14**,** 39.

[19] Tolansky, S. *Multiple-Beam Interferometry of Surfaces and Films*; **1949**, University Press, Clarendon, Oxford.
[20] Derjaguin, B. V. *Kolloid-Z.*, **1934**, 69, 155–164.
[21] Driscoll, W.G.; Vaughan, W. *Handbook of Optics*, **1978**, McGraw Hill Book Co.:New York.
[22] De Feijter, J. A.; Benjamins, J.; Veer, F. A. *Biopolymers*, **1978**, 17, 1759-1772.
[23] Butt, H-J. and Kappl. M. *Surface and Interfacial Forces*.**2010**, Wiley-VCH Verlag GmbH Co. KGaAWeinheim.
[24] Székács, A.; Adányi, N.; Székács, I.; Majer-Baranyi, K.; Szendrö, I. *Applied Optics*, **2009**, 48, 151-158.
[25] De Feijter, J. A.; Benjamins, J.; Veer, F. A. *Biopolymers*, **1978**, 17, 1759-1772.
[26] Javakhishvili, I.; Røn, T.; Jankova, K.; Hvilsted, S.; Lee, S. *Macromolecules*, **2014,** 47, 2019-2029.
[27] Schurtenberger, P.; Newman, M. E. *IUPAC Environmental Analytical Chemistry Series*, **1993**, 2, Lewis Publishers, 37-115.
[28] Miller, J.; Schatzel, K.; Vincent, B. *Journal of Colloid and Interface Science*, **1991**, 143 (2),532-554.
[29] Wilson, W. W.; Wade, M. M; Holman, S. C; Champlin, F. R. *J. Microbiol. Meth.*, **2001**, 43,153-164.
[30] Hunter, R. J. *Zeta potential in colloid science. Principles and applications*, **1981**, Academic press.
[31] Hammes, G.G. *Spectroscopy for the Biological Sciences* **2005**, John Wiley & Sons, Inc.
[32] Kelly, S. M.; Jess, T. J.; Price, N. C. *Biochimica et BiophysicaActa*. **2005**, 1751, 119-139.

CHAPTER 2

Wet Adhesion Of Mussel Foot Proteins

Mussel foot proteins (Mfps) are being increasingly investigated for their ability to generate adhesion underwater. *Mytilus* species is one of the most extensively studied mussel species. At least 12 different foot proteins have been characterized from the byssus of *Mytilus* species, and eight of these are present in adhesive plaque whereas the rest are found in plaque as well as byssal threads.[1,2,3] All mfps are post-translationally modified to various extents with the amino acid 3,4,-dihydroxyphenyl-L-alanine (Dopa) (Intro., Fig. 2).[4]

While initial studies of mfps have proposed that the adhesion depends on Dopa, recent work has demonstrated that the success of mussel adhesion goes beyond the Dopa 'paradigm'. These studies have notably revealed that stronger adhesion is the effect of redox chemistry between mfps (Intro., Fig. 5), the hydrophobic/hydrophilic interactions can also engage in adhesive interactions, and the local concentration of adhesive proteins during secretion also plays a critical role to ensure proper plaque delivery. The recent studies of mfps suggests that the abundance and proximity of catecholic Dopa and lysine residues interact synergistically to displace hydrated salt ions and thereby promoting adhesion.[2]

Since the current understanding of these systems is based on a limited set of mussel species, the primary objective of the present work was to expand this knowledge base by

studying the adhesion mechanism of Asian green mussels *Perna viridis*. Three Dopa-containing P. viridis foot proteins, termed Pvfp-3, -5, and -6 have been identified. Pvfps exhibited similar molecular weights to *Mytilus* adhesive proteins, however, their primary amino acid sequences were found to diverge significantly. These proteins were found to contain DOPA and notably, each of them were extremely rich in cysteine.[4] This is not the case for all the mfps, except Mfp-6 which was recently found to have high concentration of Cys (more than 11 mol%).[5,6] Abundance of cysteine in all known Pvfps suggests that distinct species may have adopted different strategies for underwater adhesion based on different protein molecular structure.

The chemical versatility of Dopa in adhering to wide range of substrates is indeed an asset only if its reactivity is precisely controlled, since oxidation of Dopa compromises its adhesive property.[7] There are several factors which may lead to oxidation of Dopa to Dopa-quinone (Intro., Fig. 3). Spontaneously oxidation occurs at alkaline pH[8] and auto-oxidation which refers to spontaneous oxidation of cathechol in the presence of oxygen at neutral pH leads to loss of adhesion of mfps to substrates like mica and titanium.[7,9] Other factors include exposure to light and oxidation over time. Dopa oxidation in Pvfps, unlike mfps, can be limited by the cysteine-based redox activity, since all of the Pvfps identified are extremely rich in cysteine (Intro., Fig. 5).

In this section we review the main bio-chemical features of Pvfps, some of which were studied in collaboration with prof. A. Miserez at NTU Singapore and recently published in ref.[4] Injection of KCl solution in the foot organ inducing the secretion of Pvfps from

the groove within the mussel foot, which reasonably mimics the natural byssus secretions of *P. viridis*, is referred as saline-induced mussel secretion. Saline-induced secretions of *P. viridis* were collected from the groove at the tip of the foot organ before and after injection at times ranging between 10 s to 30 min. Pvfp-5 variants which typically appeared after 10 s of saline injection, were always the first to be secreted and had molecular weight (MW) in the range 8-10 kDa. Pvfp-3 variants appeared after 30 s, often concurrently with Pvfp-5 had MW in the range 5-6 kDa. Depending on the individual mussel, Pvfp-6 at 11.4 kDa appeared from 5 min after injection, along with Pvfp-3 and -5. All Pvfps predominantly exhibited random coil structure. Dynamic light scattering (DLS) revealed a hydrodynamic diameter, d_H = 7.42±0.44, 9.50±0.26 and 24.13±0.84 nm for Pvfp-3, -5 and -6, respectively.

2.1 Results

2.1.1Adhesion between Pvfp-5 layers

Pvfp-5, the first protein to be secreted by *P. viridis*, is enriched with tyrosine (Tyr)/Dopa residues and contains ~ 11 mol% Dopa and 21 mol% Tyr side chains in its primary sequence.[4] High Dopa content and its localization at plaque-substrate interface has provoked interest in its adhesive properties. SFA was used to determine adhesion between interacting Pvfp-5 layers and its adhesion to mica. More specifically we explored the effects of changing pH on adhesive properties of Pvfp-5.

(A) Acid pH

Purified Pvfp-5 was dissolved at concentration of 0.02 mg/mL in acid saline containing 0.25 M potassium nitrate (KNO_3) or potassium chloride (KCl) and 0.1M or 0.01M Acetic acid (AcOH), with pH ≈ 3 or pH ≈ 4, respectively. Proteins were adsorbed from the solution on the mica surfaces for 20 minutes and before initiating SFA force measurements, adsorption was stopped by flushing the surfaces with protein-free acid saline with pH ≈ 3 or pH ≈ 4.

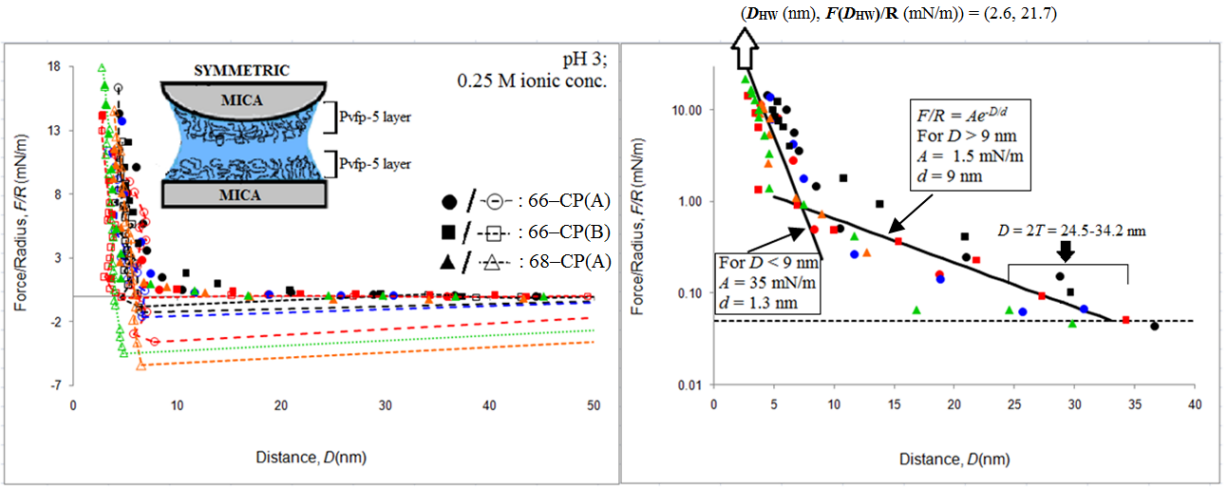

Figure 2.1 (**A**) Force–distance (*F–D*) curve measured between two Pvfp-5 coated mica surfaces (symmetric configuration) at pH 3. (**B**)Semi-logarithmic plot showing the range of repulsion *2T*, force detection threshold (dotted line) and exponential curves $F/R=Ae^{-D/d}$. Filled/open symbols indicate forces on approach/retraction of the surfaces. Each contact position (CP) is represented with a different symbol and each force run (FR) with different color.

Interaction forces (*F/R*) between pair of Pvfp-5 coated mica surfaces were measured as a function of separation distance (*D*) at acidic pH conditions (Fig. 2.1A and 2.2A). Three different contact positions (CP) were tested for pH 3(Fig. 2.1A) and one at pH 4 (Fig. 2.2A). The maximum adhesive force at pH 3 was $F_a/R \approx 5.4$mN/m upon separating two

surfaces after a contact time equal to 1 min and surfaces jumped apart from contact at D = 4 to 136.5 nm (Table 2.1). The total contact time refers to the time for which the motor (used for varying surface separation) is paused when the surfaces are in contact.At pH 4, the maximum adhesive force was $F_a/R \approx$ 5.65 mN/m after a contact time of 6 min and surfaces jumped apart from contact at D = 3.3 nm to 132 nm (Table 2.1). The adhesion showed variability from one measurement to another as adhesion may depend from multiple factors that were not explicitly controlled such as contact time or maximum load applied during compression. However, a clear trend emerged that that adhesion decreased with time as the surfaces were repeatedly approached and retracted at same contact position and as different contact positions were tested (Table 2.1). This was most likely due to oxidation of Dopa.[4]

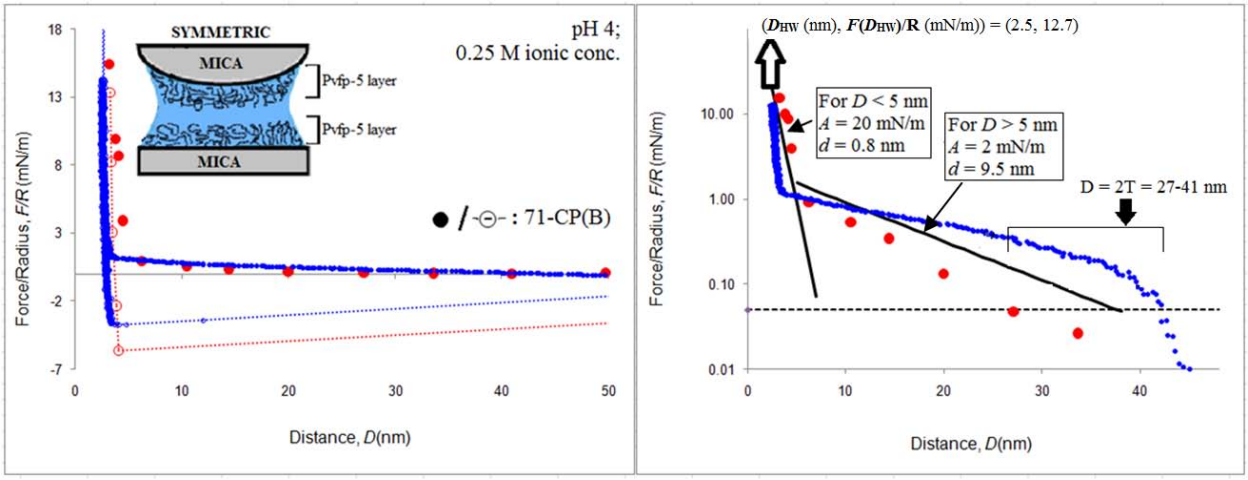

Figure 2.2 (**A**) Force–distance (*F–D*) curve measured between two Pvfp-5 coated mica surfaces (symmetric configuration) at pH 4 and (**B**) semi-logarithmic plot. Filled circles are the forces on approach; open circles are the forces on retraction. Single contact position (CP) with two individual force runs (FR) are represented with different color.

In view of such variability, for each set of measurements we also calculated the average value of the adhesion force, that was ~ 2.5 mN/m for pH 3 and ~4.6 mN/m for pH 4. For the symmetric configuration in SFA experiments, the thickness, *T,* of the adsorbed protein layer on the surface is determined as half of the distance, $D = 2T$ where the repulsive force consistently exceed the threshold, $F/R > 0.05$ mN/m. For Pvfp5–Pvfp5 interaction was $2T$ = 24.5–34.2 nm at pH 3 (Fig. 2.1B) and $2T$ = 27–41 nm at pH 4 (Fig. 2.2B).

Exp. No.– Contact position (CP) – Force Run (FR)	pH	Adhesive force, F_a/R (mN/m)	Hard wall, D_{HW} (nm)	Max. load applied, $F(D_{HW})$ (mN/m)	Jump-out distance (nm)	Contact time (min)
66 – CP(A) FR0	3	1.3	4.4	14.3	75	3.5
66 – CP(A) FR1	3	3.5	4.1	11.2	89	6
66 – CP(A) FR2	3	1.6	4.6	13.5	72,5	6
66 – CP(B) FR0	3	0.8	5.4	12	34	3.5
66 – CP(B) FR1	3	0.11	2.8	14.2	15.2	1
68 – CP(A) FR0	3	5.4	4.0	11.5	136.5	1
68 – CP(A) FR1	3	4.5	2.6	21.7	116.8	1
71 – CP(B) FR0	4	5.65	3.3	15	132	6
71 – CP(B) FR1	4	3.7	2.5	12.7	85	1

Table 2.1 Summary of Pvfp5–Pvfp5 interactions in acidic saline as measured by SFA. At least two distinct force runs (FRs) were recorded for each contact position (CP) tested.

At the high ionic strengths of our experiments, long-range electrostatic interactions are screened and the Debye length of the saline was smaller than 1 nm.[10] Therefore the long range repulsion can be attributed to the overlap between the adsorbed protein layers on opposite surfaces, each having an approximate thickness T = 12–17 nm at pH 3 and T = 13–21 nm at pH 4, respectively. Dynamic light scattering (DLS) revealed a d_H = (9.50 ±

0.26) nm for the Pvfp-5 molecule, which actually represents the average value of diameter of Pvfp-5 aggregates in solution. Larger value of adsorbed Pvfp-5 layer, i.e., $T > d_H$, may be due to further aggregation of particles or presence of long tails (Fig. 2.3).

Fig. 2.1B and 2.2B shows that the repulsion sets in at comparably larger distances (D=2T) for the first approach and appeared to shift towards smaller distances for the retraction part of force curve as well as successive approaches for a given contact position. This hysteresis indicates that the adsorbed molecules and aggregates could be irreversibly compacted or flattened on the substrate, perhaps due to the formation of additional Dopa-Dopa covalent cross-links or Dopa-mica hydrogen bonds upon compression.

The force curve becomes approximately exponential at distances D < 9 nm at pH 3, with a decay length, d ≈ 1.3 nm (Fig. 2.1B) and D < 5 nm at pH 4, with d ≈ 0.8 nm (Fig. 2.2B). This behavior suggests that Pvfp-5 was adsorbed as a soft-hydrated layer, as opposed to a compact "hard-wall" coating, allowing water and protein molecules to move and rearrange as the compressive force was increased.

Figure 2.3 Schematic of the adsorbed Pvfp-5 on mica showing hydrodynamic diameter (d_H) and layer thickness (T).

(B) Basic pH

In these experiments, adsorption of Pvfp-5 on mica was done as described in the previous section, and force measurements were done after flushing the surfaces with protein-free alkaline solution (pH≈ 8 –10). The solution pH was adjusted by adding small amounts sodium hydroxide (NaOH). Since Pvfp-5 is enriched with cysteine, tyrosine and Dopa residues[4] and possible synergy and redox activity between catecholic Dopa and cysteine can resist oxidation at high pH conditions, force-distance profiles and adhesion forces were measured to test the ability of Pvfp-5 to sustain adhesion at basic pH.

After adsorption, rinsing with acid saline and verifying that there was adhesion, the surfaces were rinsed again with basic saline with pH ≈ 8 –10. A first set of force-distance profile as a function of *D* was measured for Pvfp-5 coated mica surfaces at pH 8. Two distinct force runs showed hysteresis between approach and retraction, but no adhesion was recorded (Fig. 2.4A, Table 2.2). Note that the rinsing with pH 8 saline and force measurements were done 2 days (> 48 hours) after adsorption. Oxidation of Dopa over time and other factors like long exposure to light may have contributed to absence of adhesion between Pvfp-5 layers at pH 8. Upon approaching, the repulsive force was observed setting in at $2T$= 60–61 nm (Fig. 2.4B), higher than the repulsion range observed for the same system at acidic pH. This may be due to the pH dependent conformational changes of adsorbed protein layer.[11] The force curve became approximately exponential at distance D < 9 nm, with a decay length, d ≈ 0.8 nm (Fig. 2.4B).

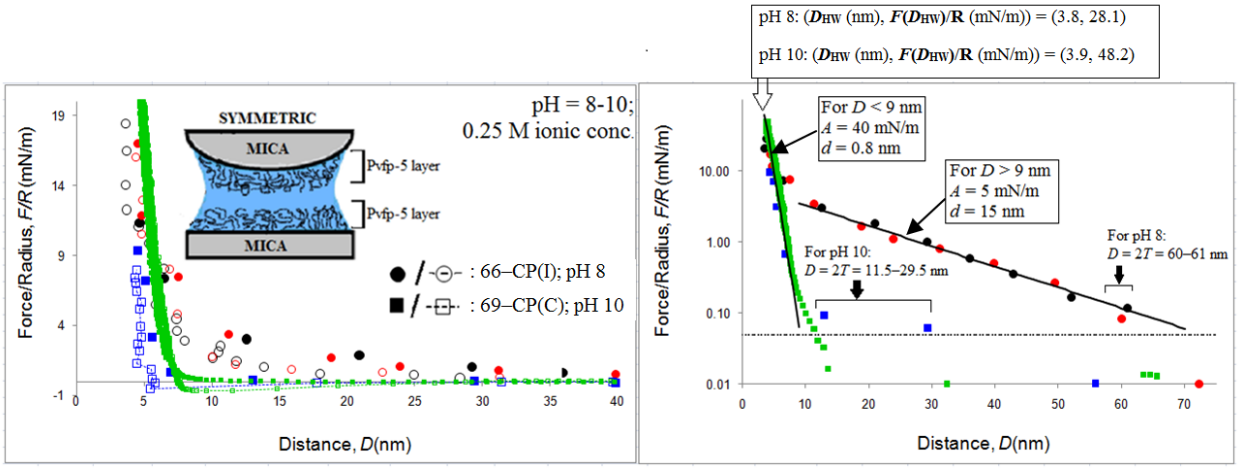

Figure 2.4 (**A**) Force–distance (*F–D*) curve measured between two Pvfp-5 coated mica surfaces at pH≈ 8 (circles - red/black) and pH ≈ 10 (squares - blue/green), and(**B**) semi-logarithmic plot. Filled/open symbols indicate forces on approach/retraction of the surfaces. Individual FRs are represented with different color.

Exp. No.– Contact position (CP) – Force Run (FR)	pH	Adhesive force, F_a/R (mN/m)	Hard wall, D_{HW} (nm)	Max. load applied, $F(D_{HW})$ (mN/m)	Jump-out distance (nm)	Contact time (min)
66 – CP(I) FR0	8	No adhesion	3.8	28	-	0.5
66 – CP(I) FR1	8	No adhesion	4.5	17	-	7
69– CP(C) FR1	10	0.53	4.5	9.4	18	1
69– CP(C) FR3	10	0.86	3.8	42.5	29	1

Table 2.2 Summary of Pvfp5–Pvfp5 interactions in basic saline as measured by SFA.

The second set of force-distance profile as a function of *D* was measured for Pvfp-5 at pH 10. Unlike the first set of data, the second set was acquired within few hours from adsorption to limit Dopa oxidation . Two distinct force runs were recorded. Adhesive force upon retraction was recorded for both the force runs at pH 10. For FR1 with applied load 9.4 mN/m, measured adhesive force was equal to -0.53 mN/m. For FR3 with much higher applied load equal to 42.5 mN/m, the adhesion force increased to -0.86 mN/m,

about 62% rise of the initial adhesion. The increase in maximum applied load was approximately 350% of the initial load. Since all the parameters for the two consecutive force runs were same except the maximum load applied, it indicates that the adhesion force as well as the jump out distance for Pvfp-5 adsorbed on mica surface was dependent on the maximum load applied provided that the difference in applied load for two consecutive runs is considerably higher.[3]

Hysteresis was present for both the force runs. The approaching branch of the force curve revealed a repulsion setting in at a comparably smaller surface separation of $2T \approx 11.5–29.5$ nm than that recorded for acidic pH. The measurements made in basic buffer conditions indicate that Cys enriched Pvfp-5 is indeed resistant to oxidation and thereby preserves adhesion even at high pH.

(C) Neutral pH

Interaction forces (F/R) between Pvfp-5 coated mica surfaces were measured as a function of separation distance (D) in neutral saline. After adsorption, rinsing with acid saline and verifying that there was adhesion, the surfaces were rinsed again with protein-free neutral saline with pH ≈ 5.5–7.0 without added HCl or NaOH.

A first set of force-distance profile was measured at pH 5.5, where four distinct runs, were recorded (Fig. 2.5A, Table 2.3). The first force curve (69–CP(A) FR1 in Fig. 2.5A) recorded the strongest adhesive force, $F_a/R \approx 2.45$ mN/m upon separating the two surfaces and the surfaces jumped apart from $D = 3.7$ to 62 nm. Adhesion force at pH 5.5 decreased with time as the number of approach/separation force run cycles progressed

during experiment. Decrease in adhesion was probably due to oxidation of Dopa. The onset of repulsion was observed at $2T$ = 19–30 nm (Fig. 2.5B) which was comparable with the value measured at acidic pH ≈ 3 (Fig. 2.1B). Thin hard-wall, $D_{HW} \approx 4$ nm was measured and force curve became approximately exponential at distance, $D < 5$ nm with a decay length, $d \approx 0.75$ nm (Fig. 2.5B) .

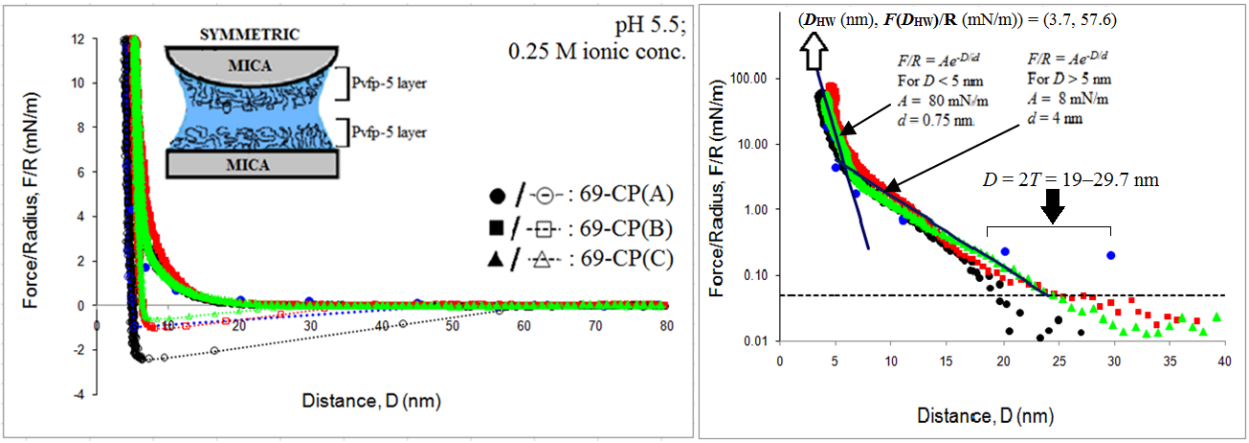

Figure 2.5 (**A**) Force–distance (*F–D*) curve measured between two Pvfp-5 coated mica surfaces at pH ≈ 5.5 and (**B**)semi-logarithmic plot. Filled/open symbols indicate forces on approach/retraction and circles, squares and triangles indicate different CPs.

Exp. No.– Contact position (CP) – Force Run (FR)	pH	Adhesive force, F_a/R (mN/m)	Hard wall, D_{HW} (nm)	Max. load applied, $F(D_{HW})$ (mN/m)	Jump-out distance (nm)	Contact time (min)
69 – CP(A) FR1	5.5	2.45	3.7	57.6	62	1
69– CP(A) FR2	5.5	0.97	4.2	18.5	50	6
69– CP(B) FR1	5.5	1.06	4.6	76	38	1
69– CP(C) FR0	5.5	0.6	5.3	11.3	33	1
66–CP(C)FR3	7	0.84	4.1	28	41	10
66–CP(C)FR4	7	1.28	3.2	25	44	20
66–CP(C)FR5	7	0.43	2.9	35	25	1
66–CP(D)FR1	7	0.82	2.2	15	38	1

Table 2.3 Summary of Pvfp5–Pvfp5 interactions in neutral saline as measured by SFA.

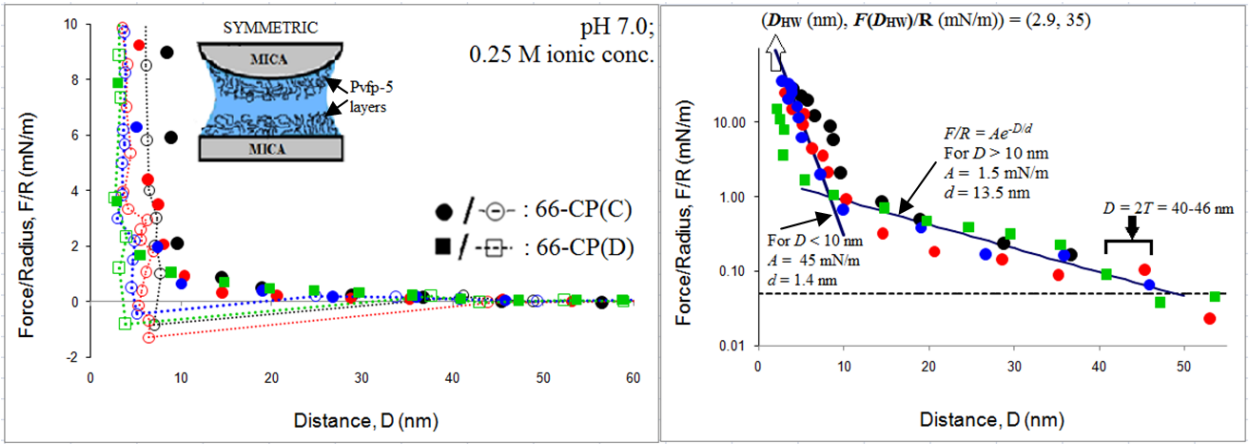

Figure 2.6 (**A**) Force–distance (*F–D*) curve measured between two Pvfp-5 coated mica surfaces at pH ≈ 7.0 and (**B**)semi-logarithmic plot. Filled/open symbols indicate forces on approach/retraction and two different CPs are represented with circles and squares, respectively. .

A second set of force-distance profile was measured at pH 7.0. Four distinct runs were recorded. The first run (66–CP(C)FR3 in Fig. 2.6A) recorded adhesive force, $F_a/R \approx 0.84$ mN/m, where the surfaces were kept into contact for 10 min. The F_a/R increased to 1.28 mN/m for second force run 66–(CP(C)FR4 (Fig. 2.6A) after a 20 min. contact time and surfaces jumped apart from D = 3.2 to 44 nm, recording 53 % increase from initial adhesion with respect to increase in contact time (Table 2.3). Earlier studies on Mefp-5 at pH 2.6 reported similar behavior.[3] The onset of repulsion was observed at $2T$= 40–46 nm (Fig. 2.6B), greater than repulsion range recorded at pH 3.0, 4.0 and 5.5 (Fig. 2.1B, 2.2B and 2.5B). Thin hard-wall, $D_{HW} \approx$ 2.5 nm was measured and force curve became approximately exponential at distance, D< 10 nm with a decay length, $d \approx$ 1.4 nm (Fig. 2.6B) .

2.1.2 Adhesion between Pvfp-5 and mica

In asymmetric testing, a thin film of Pvfp-5 was deposited onto a freshly cleaved mica surface, whereas the other mica surface was left untreated. Two different purified Pvfp-5 samples with different MW, 9 kDa and 14 kDa, respectively, were considered in order to study their adhesive interaction with mica. Pvfp-5 solution was prepared, adsorbed on mica and rinsed at pH = 3–4 in the same way as for symmetric Pvfp5–Pvfp5 adhesion experiments.

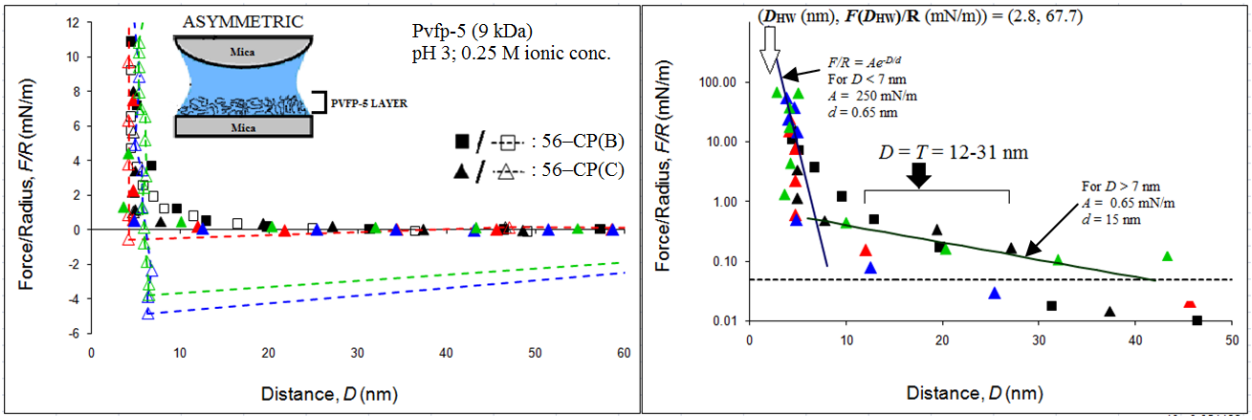

Figure 2.7 (**A**) Force–distance (*F–D*) curve measured by SFA for Pvfp-5 interaction with mica at pH≈ 3, and (**B**)semi-logarithmic plot. Filled/open symbols indicate forces on approach/retraction and two different CPs are represented with squares and triangles, respectively.

The force run recorded for Pvfp-5 (9 kDa) sample at pH 3.0 showed maximum adhesion, $F_a/R \approx 4.85$ mN/m, after the mica surface was kept in contact with adsorbed Pvfp-5 layer for 3 min and the surfaces jumped apart from $D = 3.8$ nm to 116 nm (Fig. 2.7A and Table 2.4). The onset of repulsion was observed at $D = T = 12–31$ nm (Fig. 2.7B). The hard-wall

distance, $D_{HW} \approx 2.8$ nm was measured and force curve became approximately exponential at distance, $D < 7$ nm with a decay length, $d \approx 0.65$ nm (Fig. 2.7B) .

For Pvfp-5 (14 kDa) sample, no adhesive force was measured but hysteresis in the force was observed for all the force runs recorded (Fig. 2.8A). The forces were purely repulsive and the repulsion range during surface approach (Fig. 2.8B). The hysteresis decreased as the surfaces were repeatedly approached and retracted at a same contact position. The repulsion onset was observed at T = 19–40.5 nm and the hard-wall distance, $D_{HW} \approx 2.06$ nm was measured, and force curve became approximately exponential at distance, $D< 6$ nm with a decay length, $d \approx 1.5$ nm (Fig. 2.8B) .

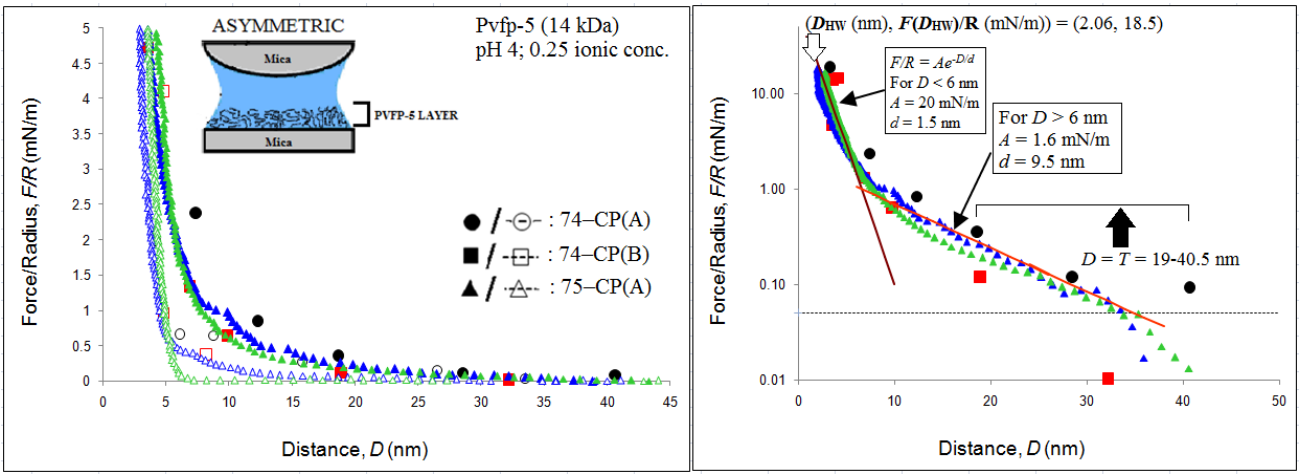

Figure 2.8 (**A**) Force–distance (*F–D*) curve measured by SFA for Pvfp-5 (14kDa) interaction with mica at pH ≈ 4, and (**B**)semi-logarithmic plot. Filled/open symbols indicate forces on approach/retraction and three different CPs are represented with circles, squares and triangles, respectively. Individual FRs are represented with different color.

Exp. No.– Contact position (CP) – Force Run (FR)	MW of sample (kDa)	pH	Adhesive force, F_a/R (mN/m)	Hard wall, D_{HW} (nm)	Max. load applied, $F(D_{HW})$ (mN/m)	Jump-out distance (nm)	Contact time (min)
56 – CP(B) FR2	9	3	No adhesion	4.5	11	NA	1
56 – CP(C) FR0	9	3	No adhesion	4.7	16	47	4
56 – CP(C) FR1	9	3	0.57	4.2	24	47	4
56 – CP(C) FR2	9	3	4.85	3.8	53	116	3
56 – CP(C) FR3	9	3	3.79	2.8	68	113	5
74– CP(A) FR0	14	4	No adhesion	3.2	18	NA	1
74– CP(B) FR0	14	4	No adhesion	4.1	15	NA	1
75– CP(A) FR0	14	4	No adhesion	2.1	18	NA	1
75– CP(A) FR1	14	4	No adhesion	2.7	20	NA	1

Table 2.4 Summary of Pvfp-5 interactions with mica as measured by SFA.

2.1.3 Adhesion between Pvfp-3 layers

Pvfp-3, the second protein to be secreted by *P. viridis* following Pvfp-5, contains ~ 2 mol% Dopa, comparatively lower than that in Pvfp-5 (11 mol%) but is enriched with Cys residues. The surface adhesion capability of Pvfp-3 was determined by SFA experiments. More specifically we explored the effects of changing pH, adsorption time and concentration on adhesion.

(A) Effect of pH

Purified Pvfp-3 was dissolved at concentration of 0.025 mg/ml in the solution containing 0.1 M AcOH and 0.25 M NaOH at pH ≈ 10. Adsorption was done in symmetric configuration and SFA force measurements were initiated 17 hours after adsorption without rinsing.

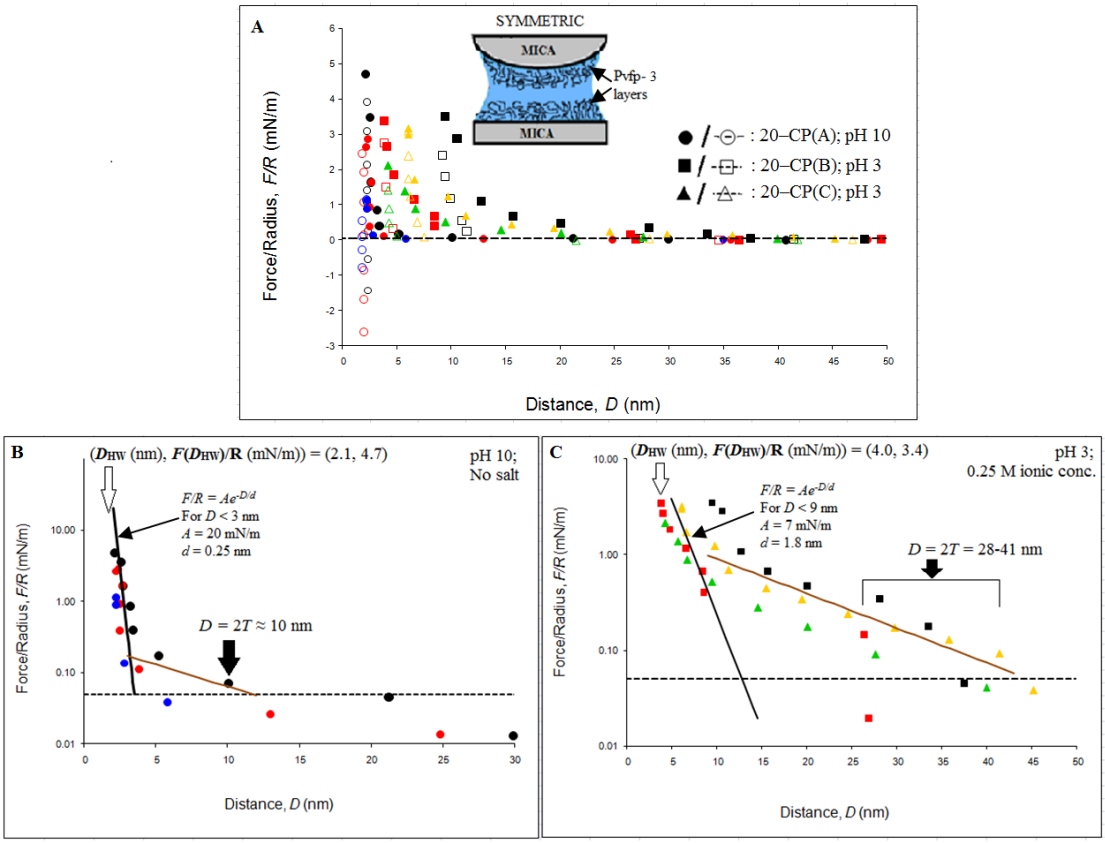

Figure 2.9 (**A**) Force–distance (*F–D*) curve measured by SFA for Pvfp-3 coated mica surfaces in symmetric configuration at pH ≈ 10-3, (**B**)semi-logarithmic plot after adsorption at pH 10, and (**C**)semi-logarithmic plot after rinsing at pH 3. Filled/open symbols indicate forces on approach/retraction where circles indicate CP tested at pH 10 and squares and triangles indicate two different CPs studied at pH 3.Individual FRs are represented with different color.

Three distinct force runs were recorded at pH 10. The strongest adhesive force was $F_a/R \approx$ 2.61 mN/m upon separating the two surfaces after a brief contact time of 26 seconds and surfaces jumped apart from D = 2.4 to 235 nm (Table 2.5). The onset of repulsion for Pvfp3–Pvfp3 interaction at pH 10 was observed at $2T \approx$ 10 nm (Fig. 2.9B). Thin hard-

wall, $D_{HW} \approx 2.2$ nm was measured and force curve became approximately exponential at distance, $D < 3$ nm with a decay length, $d \approx 0.25$ nm (Fig. 2.9B).

After measurements at basic pH, protein-free acid saline (0.1 M AcOH + 0.25 M KCl; pH ≈ 3), was used to rinse the surfaces. All the force runs after rinsing showed hysteresis between approach and retraction, but no adhesion was recorded (Table 2.5). Upon approaching, the repulsive forces were observed setting in at $2T = 28–41$ nm (Fig. 2.9C), higher than the repulsion range observed for the same system at pH 10 (Fig. 2.9B).

Exp. No.– Contact position (CP) – Force Run (FR)	pH	Adhesive force, F_a/R (mN/m)	Hard wall, D_{HW} (nm)	Max. load applied, $F(D_{HW})$ (mN/m)	Jump-out distance (nm)	Contact time (sec)
20 – CP(A) FR2	10	1.43	2.2	4.7	131	20
20– CP(A) FR3	10	2.61	2.4	2.9	235	26
20– CP(A) FR4	10	0.8	2.3	1.1	109	30
20– CP(B) FR1	3	NA	9.5	3.5	NA	23
20– CP(B) FR3	3	NA	3.9	3.4	35	23
20– CP(C) FR1	3	NA	6.1	3.2	28	77
20– CP(C) FR2	3	NA	4.3	2.1	21	21

Table 2.5 Summary of Pvfp3–Pvfp3 interactions at basic and acidic pH conditions as measured by SFA.

The force run (20 – CP(B) FR1 in Fig. 2.9A and C) recorded after rinsing showed larger repulsion range of $2T \approx 41$ nm, indicating swelling of the adsorbed protein layers, which may reflect pH-dependent conformational changes of adsorbed protein layer.[11] The repulsion range decreased for the subsequent force runs recorded. Observed hysteresis and decreasing repulsion range indicates an irreversible and progressive compaction of adsorbed protein layers.

(B) Effect of adsorption time

To study the effect of adsorption time on adhesion, Pvfp-3 sample was dissolved at the concentration of 0.04 mg/ml in 0.9 M AcOH solution without added salt at pH ≈ 2.4. Adsorption was done in symmetric configuration and SFA force measurements were initiated at different adsorption times (1, 4, 16, and 19 hours) without rinsing.

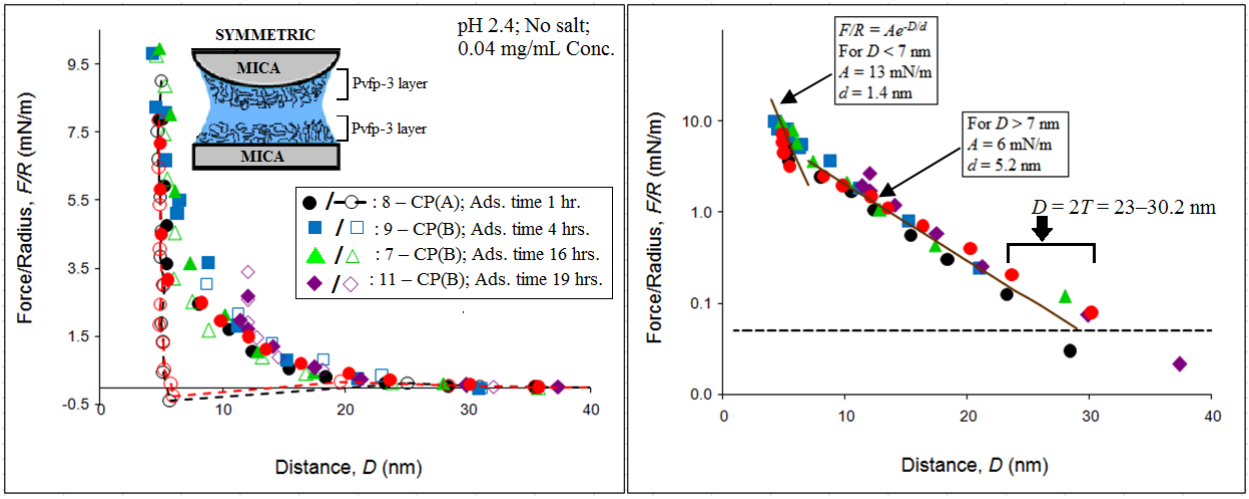

Figure 2.10 (**A**) Force–distance (*F–D*) curve measured by SFA for Pvfp-3 coated mica surfaces in symmetric configuration at pH ≈ 2.4, and (**B**)semi-logarithmic plot. Filled/open symbols indicate forces on approach/retraction and four experiments with different adsorption times are represented with circles, squares, triangles, and diamonds, respectively. Individual FRs are represented with different color.

Fig. 2.10A shows four independent experiments with different adsorption times indicated with different symbols. Both force runs recorded for experiment with shortest adsorption time of 1 hour showed weak adhesion (Table 2.6). The strongest adhesive force was F_a/R ≈ 0.39 mN/m upon separating two surfaces after a brief contact time of 35 seconds and surfaces jumped apart from D = 4.9 to 25.1 nm (Table 2.6). Experiments with longer

adsorption times showed hysteresis between approach and retraction, but did not show any adhesion (Fig. 2.10).

Exp. No.– Contact position (CP) – Force Run (FR)	Adsorption time (Hrs.)	pH	Adhesive force, F_a/R (mN/m)	Hard wall, D_{HW} (nm)	Max. load applied, $F(D_{HW})$ (mN/m)	Jump-out distance (nm)	Contact time (sec)
8 – CP(A) FR2	1	2.4	0.39	4.9	7.87	25.1	35
8 – CP(A) FR3	1	2.4	0.26	5.0	7.17	19.6	43
9– CP(B) FR1	4	2.4	NA	4.3	9.8	NA	22
7– CP(B) FR1	16	2.4	NA	4.9	18.3	NA	32
11– CP(B) FR1	19	2.4	NA	12.1	2.7	NA	18

Table 2.6 Summary of Pvfp3–Pvfp3 interactions at basic and acidic pH conditions as measured by SFA.

The onset of repulsion for Pvfp3–Pvfp3 interaction was observed at $2T \approx 23$–30.2 nm (Fig. 2.10B). Longer adsorption times may lead to excessive cross-linking and oxidation of Dopa, resulting in diminished or no adhesion. Also, longer adsorption time leads to more Dopa H-bonding at protein/mica interface,[3] which may in turn leave less/no exposed Dopa molecules to interact and create adhesive bonds with interacting protein layer/exposed (mica) surface (Fig. 2.11).

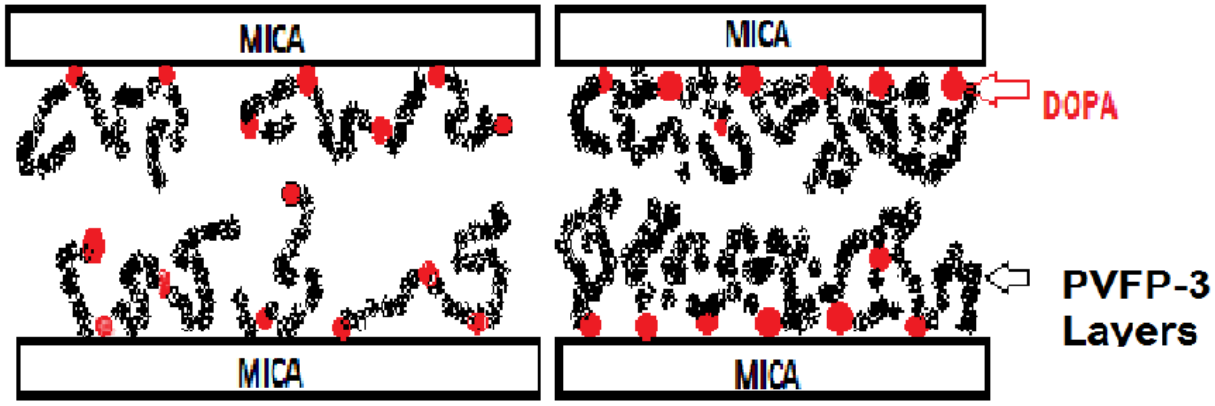

Figure 2.11 Schematic showing exposed Dopa molecules (left) and screened Dopa molecules (right).

(C) Effect of concentration

To study the effect of concentration on adhesion, Pvfp-3 sample was dissolved in the solution containing 0.1 M AcOH and 0.25 M KCl at pH ≈ 3 at two different concentrations of 0.02 mg/mL and 0.1 mg/mL, respectively. Adsorption was done in symmetric configuration and SFA force measurements were initiated 14 hours after adsorption without rinsing.

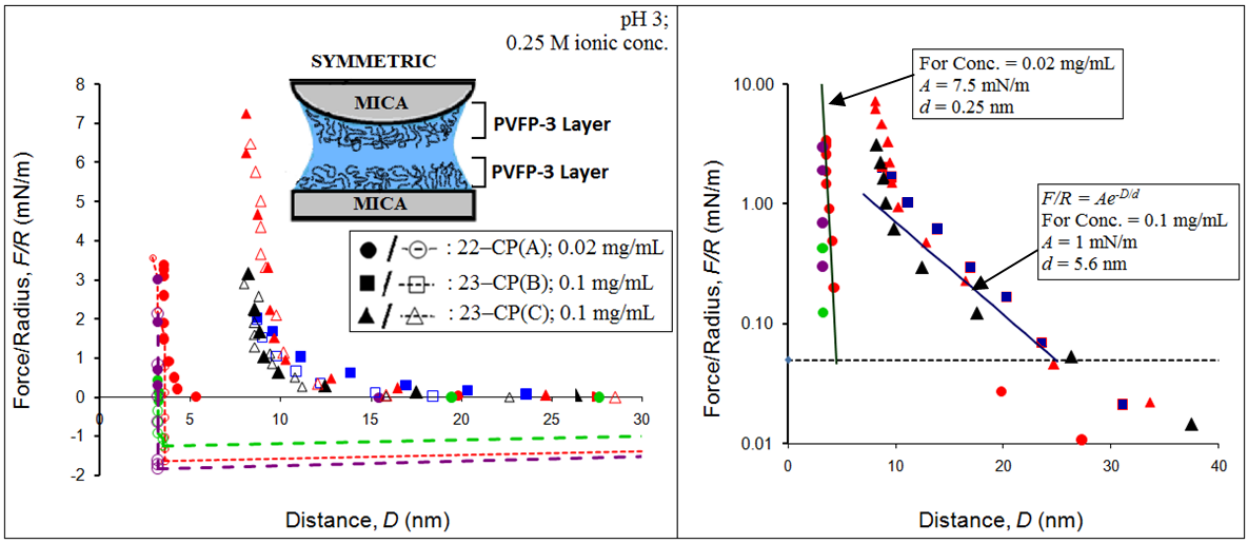

Figure 2.12 (**A**) Force–distance (*F–D*) curve measured by SFA for Pvfp-3 layers adsorbed from solution with different concentration at pH≈ 3, and (**B**) semi-logarithmic plot. Filled/open symbols indicate forces on approach/retraction and different CPs with varying solution concentration are represented with circles, squares, and triangles, respectively.

Three distinct contact positions, one corresponding to low and other two corresponding to high concentration solution, are indicated with different symbols (Fig. 2.12A). All three force runs recorded for experiment with low concentration solution showed adhesion

(Table 2.7). The strongest adhesive force was $F_a/R \approx 1.84$ mN/m upon separating two surfaces after a brief contact time of 30 seconds and surfaces jumped apart from $D = 3.2$ to 149 nm (Table 2.7). Upon approaching, steep repulsive force was seen setting in at $2T \approx 3.25–4.3$ nm (Fig. 2.12B), corresponding to adsorbed layer thickness, $T \approx 1.6–2.1$ nm. The hard-wall distance, $D_{HW} \approx 3.2$ nm was measured and force curve became approximately exponential at distance, $D < 4$ nm with a decay length, $d \approx 0.25$ nm (Fig. 2.12B) .

Exp. No.– Contact position (CP) – Force Run (FR)	Conc. (mg/mL)	pH	Adhesive force, F_a/R (mN/m)	Hard wall, D_{HW} (nm)	Max. load applied, $F(D_{HW})$ (mN/m)	Jump-out distance (nm)	Contact time (sec)
22 – CP(A) FR1	0.02	3	1.67	3.6	3.4	177	19
22– CP(A) FR3	0.02	3	1.25	3.2	0.42	135.5	16
22– CP(A) FR4	0.02	3	1.84	3.2	3.0	149	30
23– CP(B) FR4	0.1	3	NA	8.7	2.02	NA	14
23– CP(C) FR3	0.1	3	NA	8.2	3.17	NA	22
23– CP(C) FR4	0.1	3	NA	8.1	7.26	NA	99

Table 2.7 Summary of Pvfp3–Pvfp3 interactions at varying concentration as measured by SFA.

Experiments with higher concentration of 0.1 mg/mL showed hysteresis between approach and retraction, but did not show any adhesion (Fig. 2.12). The onset of repulsion for Pvfp3–Pvfp3 interaction was observed at $2T \approx 24–26.3$ nm (Fig. 2.12B). The force curve increased almost exponentially as D was decreased from 26.5 nm to about 9 nm with $d = 5.6$ nm and $A = 1$ mN/m (Fig. 2.11B). As D was decreased further, F increased faster than exponentially. The hard-wall distance, $D_{HW} \approx 8.1$ nm was

measured, which was greater than the value measured for experiments with low concentration Pvfp-3 solution (Fig. 2.12B and Table 2.7).

Adsorption of Pvfp-3 on mica from solutions with different concentrations resulted in adsorbed layers of varying thickness, where the layer thickness increased with concentration of the solution. Interestingly, no adhesion was found for thicker layers whereas thinner adsorbed layers displayed adhesion. This experiments support the idea that thinner layers have exposed Dopa molecules (Fig. 2.11), available to interact and form bonds with Dopa molecules on the opposite/interacting surface, thicker layers of screening the Dopa molecules and/or contain cross-linked Dopa unavailable for adhesive binding between the opposing surfaces.

2.1.4 Adhesion between Pvfp-3 and mica

To understand the adhesive mechanism of Pvfp-3 with mica, SFA measurements were done in asymmetric configuration. Pvfp-3 sample was dissolved in 0.1 M AcOH with 0.25 M potassium nitrite (KNO_3) at concentrations 20 µg/ml at pH ≈ 3. Adsorption was done on one of the mica surface for 20 minutes and before initiating SFA force measurements, adsorption was stopped by flushing the surface with protein-free buffer solution (pH ≈ 3).

Two distinct contact positions were tested as indicated in Fig. 2.13. The force curve 60 – CP(C) FR3 in Fig. 2.13A showed maximum adhesion, $F_a/R \approx$ 2.38 mN/m, after the mica surface was kept in contact with adsorbed Pvfp-3 layer for 1 min and the surfaces jumped apart from D = 3.8 to 69 nm (Table 2.8). The value of the adhesive force

measured in this case was greater than the value, $F_a/R \approx 1.84$ mN/m measured for Pvfp-3 at pH 3 in symmetric configuration (Fig. 2.12A and Table 2.7). The onset of repulsion was observed at T = 36.3–52.7 nm (Fig. 2.13B). The hard-wall distance, $D_{HW} \approx$ 2.6 nm, smaller than that measured for Pvfp-3 in symmetric case (Table 2.7), was measured and force curve became approximately exponential at distance, D < 11 nm with a decay length, $d \approx$ 1.5 nm (Fig. 2.13B).

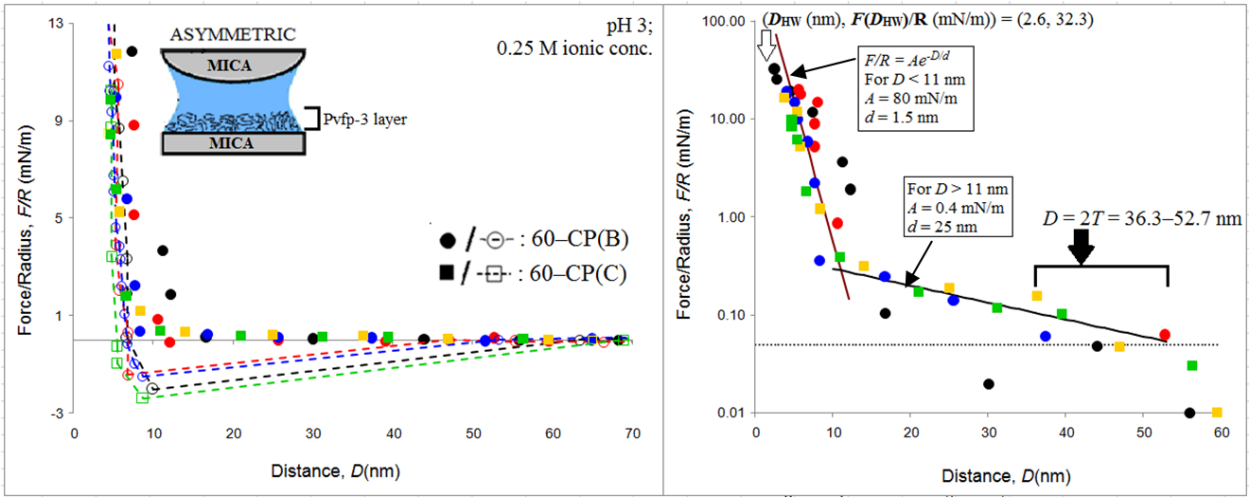

Figure 2.13 (**A**) Force–distance (F–D) curve measured by SFA for Pvfp-3 interaction with mica at pH≈ 3, and (**B**)semi-logarithmic plot. Two different CPs are represented with circles and squares and individual FRs are represented with different color.

Exp. No.–Contact position (CP) – Force Run (FR)	pH	Adhesive force, F_a/R (mN/m)	Hard wall, D_{HW} (nm)	Max. load applied, $F(D_{HW})$ (mN/m)	Jump-out distance (nm)	Contact time (min)
60 – CP(B) FR1	3	2.02	2.6	32.3	63	6
60 – CP(B) FR2	3	1.42	5.6	19.7	47	2
60 – CP(B) FR3	3	1.51	4.1	19.7	53	6
60 – CP(C) FR2	3	NA	3.7	16.5	65	2
60 – CP(C) FR3	3	2.38	4.8	10	69	1

Table 2.8 Summary of Pvfp-3 interactions with mica as measured by SFA.

2.1.5 Pvfp-5 and Pvfp-3 mixtures

By mimicking the adhesive protein secretion of *P. viridis* by stimulating the mussel foot with saline injection, and by analyzing the protein samples collected at specific time intervals, it was shown that Pvfps are secreted at discrete time intervals.[4] To further investigate and support the idea of time-regulated secretion of Pvfps, SFA experiments on mixtures of Pvfp-5 and Pvfp-3 were conducted.

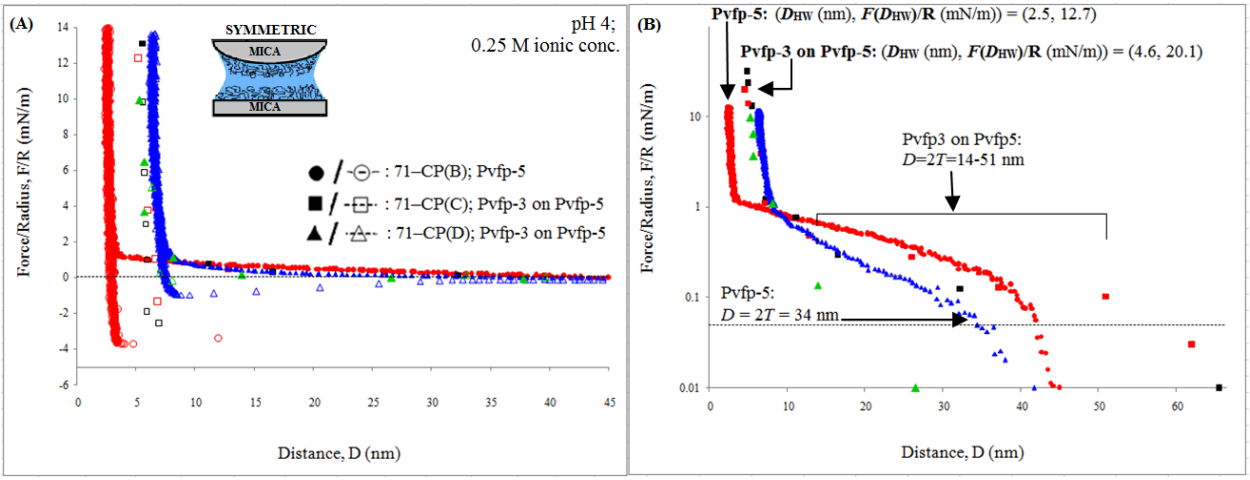

Figure 2.14 (**A**) Force–distance (*F–D*) curve measured between two Pvfp-5 (circles) coated mica surfaces followed by Pvfp-3 (squares and triangles) adsorption at pH≈4 and (**B**)semi-logarithmic plot.

Exp. No.– Contact position (CP) – Force Run (FR)	Sample	pH	Adhesive force, F_a/R (mN/m)	Hard wall, D_{HW} (nm)	Max. load applied, $F(D_{HW})$ (mN/m)	Jump-out distance (nm)	Contact time (min)
71 – CP(B) FR1	Pvfp-5	4	3.74	2.5	12.71	82.1	1
71 – CP(C) FR1	Pvfp3+Pvfp5	4	2.56	4.9	31.66	86.6	6
71 – CP(C) FR2	Pvfp3+Pvfp5	4	1.34	4.6	20.1	63.8	1
71 – CP(D) FR3	Pvfp3+Pvfp5	4	0.95	6.4	11.81	32.7	1
71 – CP(D) FR4	Pvfp3+Pvfp5	4	0.15	5.3	9.93	33.0	1

Table 2.9 Summary of interaction of mixture of Pvfp5 and Pvfp3 in symmetric configuration as measured by SFA.

In the first set of SFA experiments on mixtures, Pvfp-5 was first adsorbed from acid saline at concentration of 0.02 mg/mL at pH 4 for 20 min and after verifying adhesion, Pvfp-3 was adsorbed over pre-adsorbed Pvfp-5, following same adsorption conditions. For Pvfp-5, the adhesive force was $F_a/R \approx 3.74$ mN/m and the hard-wall distance, $D_{HW} \approx$ 2.5 nm (Fig. 2.14A-B and Table 2.9). Following adsorption of Pvfp-3, two different contact positions were tested, indicated by squares and triangles in Fig. 2.14A. The strongest adhesive force was $F_a/R \approx$ 2.56 mN/m, smaller than adhesive force recorded for Pvfp-5 alone (Fig. 2.1A, 2.2A and Table 2.1) and comparable with the values measured for Pvfp-3 alone (Fig. 2.12A and Table 2.7). Increase in D_{HW} from 2.5 nm to 4.6 nm was observed after adsorption of Pvfp-3. Adhesion decreased with time as the surfaces were repeatedly approached and retracted at same contact position and as different contact positions were tested (Table 2.9).

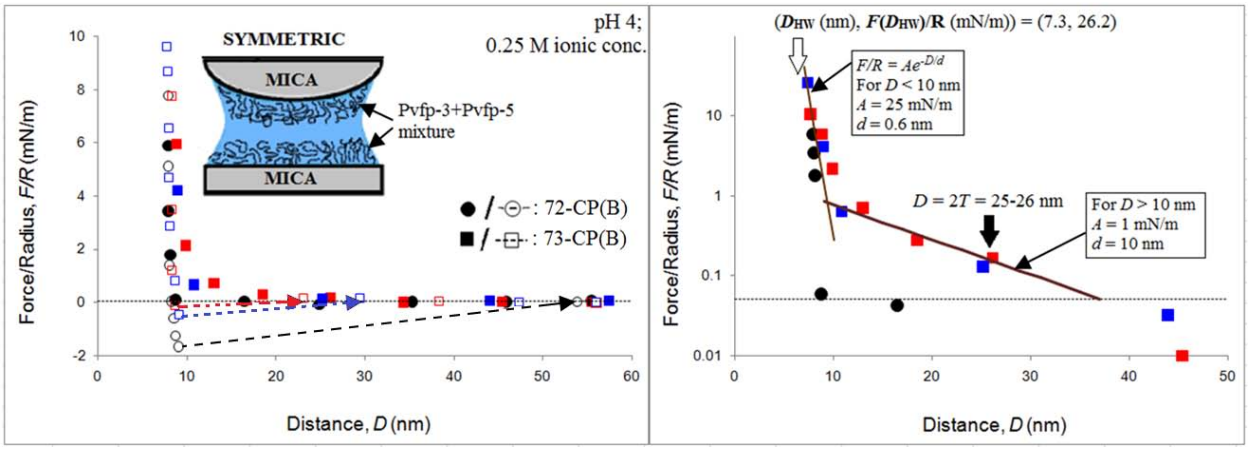

Figure 2.15 (**A**) Force–distance (*F–D*) curve measured between two mica surfaces coated with Pvfp5 and Pvfp3 from a mixed solution at pH≈4 and (**B**) semi-logarithmic plot.

In the second set of SFA experiments on mixtures, interaction of Pvfp-5 with Pvfp-3 was studied by simultaneously adsorbing Pvfp-5 and Pvfp-3 from an equimolar mixture at pH 4. Two different contact positions indicated by circles and squares in Fig. 2.15A were tested. The first run (72 – CP(B) FR0 in Fig. 2.15A) showed maximum adhesive with $F_a/R \approx 1.68$ mN/m and $D_{HW} \approx 7.9$ nm (Fig. 2.15B and Table 2.10).

Exp. No.– Contact position (CP) – Force Run (FR)	pH	Adhesive force, F_a/R (mN/m)	Hard wall, D_{HW} (nm)	Max. load applied, $F(D_{HW})$ (mN/m)	Jump-out distance (nm)	Contact time (min)
72 – CP(B) FR0	4	1.68	7.9	5.90	53.9	1
73 – CP(B) FR0	4	0.13	8.8	5.94	23.1	1
73 – CP(B) FR1	4	0.47	7.3	26.24	29.4	1

Table 2.10 Summary of interaction of mixture of Pvfp5 and Pvfp3 in symmetric configuration as measured by SFA.

For both the cases of mixtures considered above, the adhesive forces recorded were smaller than that recorded for Pvfp-5 alone and almost comparable with Pvfp-3. It also appeared that Pvfp-3 almost screened the adhesive properties of Pvfp-5, which supports the idea of time-regulated protein secretion of *P. viridis*, which may help avoid interference of Pvfp-3 in adhesive properties of Pvfp-5. D_{HW} measured for mixture was greater than D_{HW} recorded for Pvfp-5 or Pvfp-3 alone. This suggests the formation of multilayer configuration of proteins with respect to time-regulated secretion of Pvfps where Pvfp-5 acts as primer that displaces surface-bound water and create adhesive bonds, whereas Pvfp-3 provides the first functional layer for the attachment of other Pvfps.

2.2 Conclusions

The adhesion capabilities of Pvfp-5 and Pvfp-3 was assessed by SFA experiments. Mica was used as the substrate in all the SFA experiments, enabling comparison of Pvfps with extensively studied Mfps. Here we summarize the main results.

At acid pH, Pvfp-5 is less adhesive than Mfp-5, whereas, adhesion of Pvfp-3 and Mfp-3 is comparable.

Interaction of Mfp-5 with mica at pH 2.6 measured strong adhesive with $F_a/R \sim 45$ mN/m.[3] Two symmetric Mfp-5 films exhibited significantly lower attraction ($F_a/R \sim 6$ mN/m) to one another compared to interaction of Mfp-5 with mica.[3] However, adhesion measured for Pvfp-5 in symmetric ($F_a/R = 5.6$ mN/m) and asymmetric ($F_a/R = 4.85$ mN/m) case was comparable and lower than that observed for Mfp-5 (Fig. 2.16 and Table 2.11).

In symmetric configuration, maximum adhesive forces measured for Mfp-3 at pH 5.5 were $F_a/R \approx 3$ mN/m.[1] These values were higher than $F_a/R = 1.8$ mN/m measured for Pvfp-3 at pH 3 (Fig. 2.16). The maximum adhesion strength of Pvfp-3 to mica was $F_a/R = 2.38$ at pH 3 (Fig. 2.16). This value was higher than the strongest adhesion of Mfp-3 to mica recorded earlier at pH 5.5.[12] At acid pH, Pvfp-3 showed adhesion in both symmetric and asymmetric cases.

At neutral and basic pH, Pvfp-5 and Pvfp-3 are more adhesive that their Mfp counterparts.

Exposure of Mfp-5 to pH above 7.5 reduces its adhesion by 95% due to rapid oxidation of Dopa to Dopaquinone.[13] Mfp-3 is also reported to lose its adhesive properties above pH 7.5.[1] In symmetric configuration, Pvfp-5 was adhesive at both neutral and basic pH, however the adhesion was not as strong as that recorded for acid pH (Table 2.11). However, adhesion measured for Pvfp-3 in symmetric configuration at basic pH was stronger than that measured for acid pH, under similar adsorption conditions.

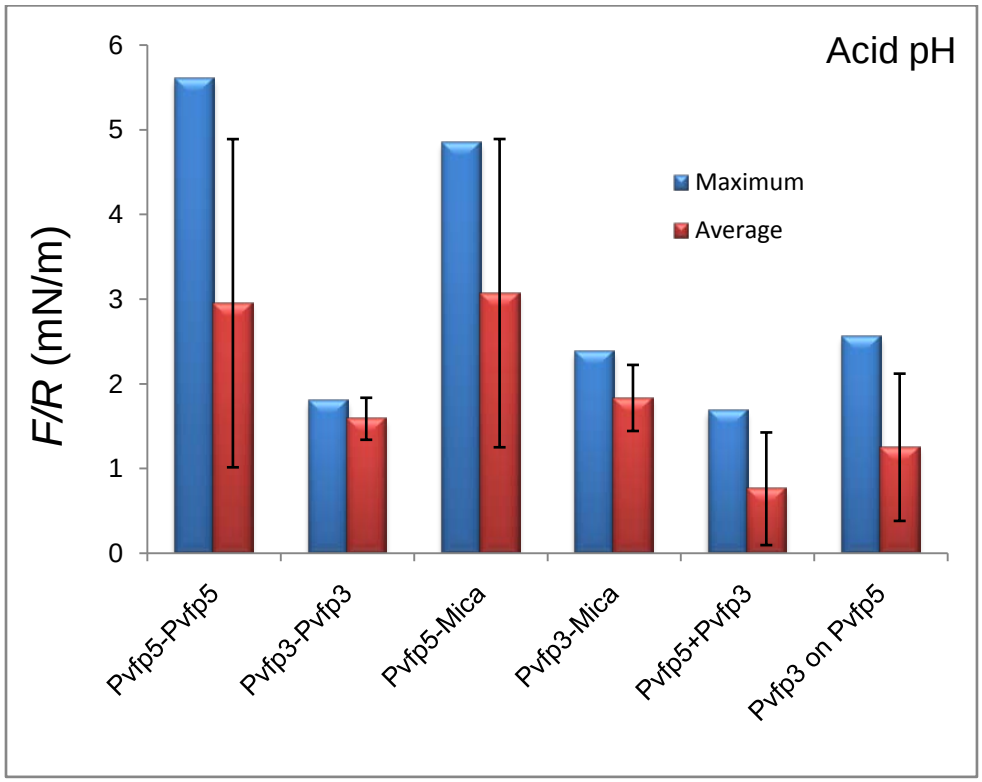

Figure 2.16 Maximum and average adhesion force as measured by SFA.

Pvfp-3 seems to be more resistant to Dopa oxidation at basic pH than Pvfp-5 but the experimental conditions were different.

Pvfp-3 at acidic pH showed a weaker adhesion compared to Pvfp-5, in line with previous SFA studies on Mfps.[3,12] However, at basic pH≈(10) conditions, maximum adhesion measured for cysteine rich Pvfp-3 was F_a/R ~ 2.6 mN/m compared to F_a/R ~ 0.9 mN/m for Pvfp-5 (Table 2.11). However, the adsorption conditions for Pvfp-5 and Pvfp-3 were different.

Interaction	Acid pH		Neutral pH		Basic pH	
	Max. F_a/R (mN/m)	Max. E_a (mJ/m^2)	Max. F_a/R (mN/m)	Max. E_a (mJ/m^2)	Max. F_a/R (mN/m)	Max. E_a (mJ/m^2)
Pvfp5-Pvfp5	5.6	1.2	2.5	0.5	0.86	0.2
Pvfp3-Pvfp3	1.8	0.4			2.61	0.6
Pvfp5-Mica	4.85	1.0				
Pvfp3-Mica	2.38	0.5				

Table 2.11 Summary of Pvfp5 and Pvfp3 interactions measured by SFA.

Pvfp-5 is more adhesive than Pvfp-3, and coadsorption of Pvfp-5 and Pvfp-3 reduces adhesion.

Co-adsorption of Pvfp-5 and Pvfp-3 resulted in an adhesion force weaker than that of Pvfp-5 and comparable to that of Pvfp-3 alone (Table 2.11). This indicates that co-secretion of these two proteins in the early phase of mussel attachment would be detrimental for adhesion. Taken together, our adsorption and SFA measurements thus quantitatively support the idea that stepwise secretion[4] of adhesive proteins is adopted by

mussel as strategy to create a functional adhesive multilayer with Pvfp-5 serving as a vanguard protein.

Adsorbing more proteins reduces adhesion

Adsorption of thicker layers of Pvfps on the substrate resulted in diminished adhesion (Fig. 2.11). Series of experiments done with varying adsorption time and protein concentration in solution revealed that thinner layer have more exposed Dopa molecules available to interact and form adhesive bonds whereas, thicker layers screen Dopa molecules as well as enhances cross-linking between Dopa molecules making them unavailable for subsequent adhesive interactions.

Final remarks

Abundance of cysteine and presence of Tyr/Dopa residues in Pvfps, suggests a different mechanism of adhesion in Pvfps as well as the possibility of cysteine based redox-chemistry to prevent Dopa oxidation at high pH (ref. Introduction Fig. 5).[14] Pvfp-3 and Pvfp-5 may be able to auto-protect themselves against Dopa oxidation, especially at high pH conditions, a hypothesis that shall be tested in future work.

By understanding the basic surface interactions and especially the role of Dopa and Cys in Pvfps, we could improve our understanding of wet adhesion and the strategies for developing next generation wet adhesives.[15]

References

[1] Lin, Q.; Gourdon, D.; Sun, C.; Holten-Andersen, N.; Anderson, T. H.; Waite, H.; Israelachvili, J. *PNAS* **2007**, 104(10), 3782–3786.
[2] Maier, G. P.; Rapp, M. V.; Waite, H.; Israelachvili, J.; Butler, A. *Science* **2015**, 349.
[3] Danner, E. W.; Kan, Y.; Hammer, M. U.; Israelachvili, J.; Waite, H. *Biochemistry* **2012**, 51(33), 6511–6518.
[4] Petrone, P.; Kumar, A.; Sutanto, C. N.; Patil, N. J.; Kannan, S.; Palaniappan, A.; Amini, S.; Zappone, B.; Verma, C.; Miserez, A.; *Nature comm.***2015**, 6:8737.
[5] Yu, J.; Wei, W.; Danner, E.; Ashley, R. K.; Israelachvili, J. N.; Waite. J. H. *Nat Chem Biol*. **2011**, 7, 588–590.
[6] Ohkawa, K.; Nagai, T.; Nishida, A.; Yamamoto, H. *J. Adhes.* **2009**, 85, 770.
[7] Lee, H. S.; Scherer, N. F.; Messersmith, P. B. *P Natl Acad Sci USA*, **2006**, 103, 12999–13003.
[8] Waite, J. H. *Comp Biochem Physiol B Comp Biochem*, **1990**, 97, 19–29.
[9] Menyo, M. S.; Hawker, C. J; Waite. J. H. *Soft Matter*, **2013**, 10314.
[10] Israelachvili, J. N. *Intermolecular and Surface Forces*, 3rd ed. Academic Press: London, **2011**.
[11] Nicklisch, S.; Waite, J. H. *Biofouling* **2012**, 28(8), 865–877.
[12] Lu, Q.; Danner. E.; Waite, J. H.; Israelachvili, J. N.; Zeng, H.; Hwang, D. S. *J. R. Soc. Interface* **2013** 10.
[13] Kan, Y.; Danner, E. W.; Israelachvili, J. N.; Waite, H. *PLoSONE* **2014**, 9(10).
[14] Yang, J.; Cohen Stuart, M. A.; Kamperman, M. *Chem. Soc. Rev.*, **2014**, 43, 8271.
[15] http://www.wired.com/2015/11/mussels-sticky-secretions-make-for-super-strong-adhesives/

CHAPTER 3

Molecular Structure and Nanomechanics of Bovine Submaxillary Mucin

3.1 Introduction

Bovine submaxillary mucin (BSM) is secreted in the saliva that lines teeth, tongue, and palate, and interacts with food, external liquids, and air.[1] BSM shows the typical structural features of mucins with a long central domain rich in proline, threonine and serine (PTS domain) that is densely grafted with anionic and hydrophilic carbohydrate chain. The C- and N- terminals are not glycosylated and contain many cationic and hydrophobic residues. The glycosylation level of PTS domains reaches 70-85% of the total molecular weight in BSM and sialic acid accounts for as much as 30% of the molecular weight (Intro., Fig. 6).[2,3]

Due to commercial availability, BSM is one of the extensively studied mucin. However, high molar mass, polydisperse nature and presence of contaminants in mucins have complicated the study of BSM under controlled chemical conditions. Proust and co-workers were the first to study the properties of adsorbed BSM on following substrates using the SFA[4]: polyethylene, oxidized polyethylene, silicone, poly(vinyl pyrrolidone) grafted silicone and mica. The result shows that the chemical modification of polymer surfaces enhances mucin adsorption, showing the importance of hydrophilic groups in the

adsorption process.[4] The SFA measurements showed that different surfaces exhibit different barrier (steric or electrostatic) for adsorption of mucin molecules arriving at substrate surface. The study on BSM interaction with functionalized polystyrene showed that BSM forms multilayers at low pH.[5] Lindh and co-workers studied adsorption of BSM on hydrophilic and hydrophobized silica using ellipsometry.[6] It was reported that BSM generally had a stronger affinity for hydrophobic surfaces and that salt addition increased the BSM uptake on hydrophilic surfaces, interpreted in terms of reduced electrostatic repulsion.[6]

This chapter is intended to give a detailed survey of the structure and mechanical properties of BSM adsorbed at solid-liquid interface. By combining different experimental techniques such as dynamic light scattering (DLS, Section 1.9), circular dischroism (CD, Section 1.11) spectroscopy, and atomic force microscopy (AFM),[1] structural features of isolated BSM molecules, namely, the hydrodynamic diameter, conformation, and contour length in dilute solutions, were studied. Nanomechanical properties of adsorbed BSM layers on mica from concentrated solutions at physiological salinity were investigated by using the SFA (Section 1.6).[1]

3.2 Purification of BSM

The purification of BSM molecules was performed by prof. Seughwan Lee and coworkers at the Denmark Technological University (DTU). In order to minimize non-mucin impurities present in commercially available mucins, anion exchange

chromatography was employed to purify the BSM samples (BSM; type I-S, M3895) purchased from Sigma-Aldrich (Brøndby, Denmark). The procedure and experiments related to the purification of BSM are described in details in Ref.,[7] while a brief summary if provided below.

As-received BSM was dissolved in 10 mM Na-acetate, 1 mM EDTA at pH 5 on a nutating mixer overnight at 4ºC to a final concentration of 10 mg/mL. The BSM solution was then filtered through 5 µm sterile filter (Pall Corporation, Cornwall, UK) to remove aggregates and fractionated on a High Load 16/26 Q Sepharose High Performance anion exchange column (GE Healthcare Life Sciences) by using Na-acetate buffer as eluent. Purity of the obtained BSM fractions was analyzed with SDS-PAGE (Sodium dodecyl sulphate polyacrylamide gel electrophoresis) that revealed nearly undetectable level of impurities.[7] The fractions containing BSM were pooled, dialyzed against water, freeze-dried and kept at -20 ºC until use. All the experimental results presented in this study were carried out exclusively with purified BSM which was supplied by DTU.

3.3 Sample preparation

Frozen lyophilized BSM was thawed at room temperature and dissolved in filtered phosphate buffer saline (PBS, form Sigma-Aldrich) containing KCl, NaCl and phosphate salts in purified water (Millipore Q from Millipore, resistivity > 18.2 MΩ.cm) at concentrations 0.15-2.2 mg/mL. Neutral PBS had pH 7.4 and Debye length

$\lambda = (\varepsilon kT / I)^{1/2} \approx 1\,\text{nm}$, where $I = \sum C_i q_i^2$ and ε is the dielectric permittivity of water, and C_i and q_i are the molarity and charge of each ionic species.[8]

DLS and CD measurements were performed on BSM samples with concentration of 2.0 mg/mL in acidic (pH 2.6) and neutral (pH 7.4) environment. For AFM measurements, BSM was adsorbed on mica from very dilute solution in neutral PBS (pH 7.4), with concentration lower than 0.01 mg/mL. SFA measurements were performed on BSM samples at pH 7.4 with BSM concentration varying from 0.15-2.2 mg/mL in PBS with adsorption time 10-15 hrs. Measurements at pH 2.6-2.9 were done at concentration of 2.0 mg/mL with adsorption time limited to 5 hrs. since acid solutions infiltrated the Ag-mica interface leading to progressive detachment of the mica sheet from the glass supports.

Acid solutions with pH to 2.6-2.9 were obtained by adding small amounts of HCl to neutral PBS, or a volume of acetic acid (AcOH) equal to the volume of neutral PBS. In both cases, the relative variation of Debye length was varied by less than 1 nm. Protein solutions were centrifugated for 3 min at 4000 rpm to remove insoluble protein aggregates and dust particles prior to SFA force measurements.

3.4 Hydrodynamic size of BSM in bulk solution

The distribution of hydrodynamic diameter, $d_{H,}$ of BSM molecules in pH 7.4 and 2.6 buffer solutions was studied using DLS. Fig. 3.1 shows the distribution of hydrodynamic size of BSM molecules weighted by scattered intensity. At pH 7.4, a single peak was observed in the range d_H = 10-200 nm, corresponding to more than 99% of the entire

peak area. The maximum of intensity was observed for diameter d_{max} = (46 ± 1) nm and the Z-average value was d_z= (35 ± 2) nm.

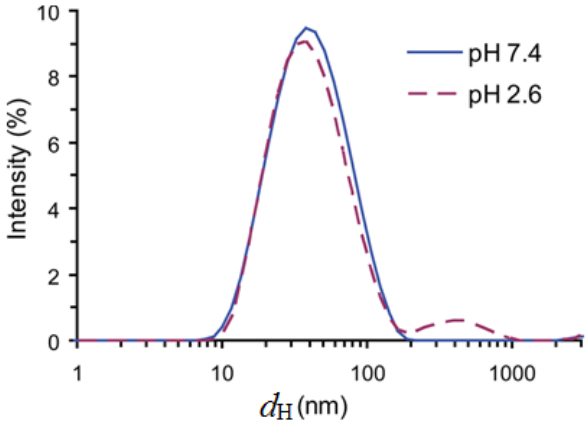

Figure 3.1. Distribution of hydrodynamic diameter d_H of BSM as a function of DLS intensity (2 mg/mL in PBS buffer at pH 2.6 and 7.4).

	neutral, X_1	acid, X_2	X_1/X_2
d_{max}(nm)	35 ± 2	44 ± 1	1.26
d_z (nm)	46 ± 1	41 ± 2	0.89
T (nm)	60 ± 5	95 ± 5	1.58
Γ (mg/m^2)	2.4 ± 0.2	9.5 ± 0.5	3.96
ρ (mg/mL)	40 ± 7	100 ± 13	2.50
A (mN/m)	22 ± 2	33 ± 2	1.50
d (nm)	20 ± 2	26 ± 2	1.30

Table 3.1. Parameters describing the conformation of BSM molecules in solution (d_{max}, d_z) and after adsorption on mica (T, Γ, ρ, A, d) from 2.0 mg/mL solution in PBS. $X_1$and X_2indicate the parameter value for neutral and acid solution, respectively.

At pH 2.6, the intensity maximum shifted to a smaller diameter d_{max} = (41 ± 2) nm and secondary peak appeared for large diameters d_H = 150-1000 nm. Accordingly, The Z-average diameter increased to d_z = (44 ± 1) nm. These results are summarized in Table

3.1 together with other physical parameters. Contraction of d_{max} and appearance of the secondary peak occurred in parallel at low pH. This can be related to the protonation of polyanionic BSM at acidic pH and the reduction of intra- and intermolecular electrostatic repulsions between negatively charged residues.

3.5 Secondary and tertiary structure of BSM molecules

The influence of varying pH on secondary and tertiary structure of BSM was investigated by CD spectroscopy (Section 1.11). As presented in Fig. 3.2,the far-UV CD spectra obtained for BSM at pH 7.4 revealed characteristic of random coil structure with a characteristic strong negative band at around 200 nm and a slight positive shoulder , in consistence with previous studies on BSM[7] and ovine submaxillary mucin (OSM).[9]

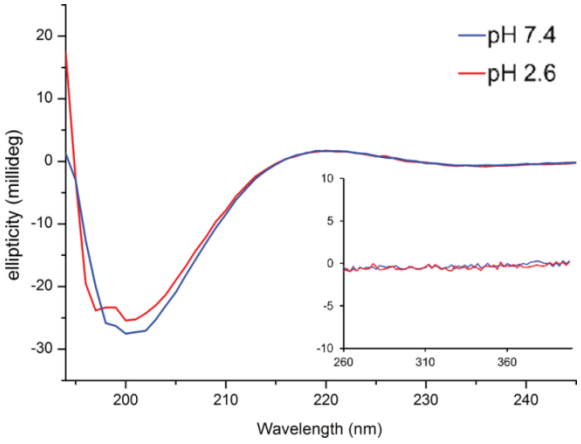

Figure 3.2. Far-UV CD spectra for 2 mg/mL BSM solution in PBS at pH 7.4 and 2.6. The inset shows the near-UV CD spectra.

At pH 2.6, no major changes in far-UV CD spectrum occurred, except that the overall intensity of the negative peak was slightly reduced. As far-UV CD spectra of BSM are determined mainly from the central glycosylated region, this indicates that the conformation of PTS region is largely maintained upon lowering the pH from 7.4 to 2.6, except for a slight weakening of the coiling. Meanwhile, no discernible peak was observed in the near-UV CD spectra, at both pH 7.4 and 2.6 (Fig. 3.2, inset), indicating that a distinct three-dimensional folding was also absent for both pH values.

3.6 Contour length and conformation of single BSM molecules

Fig. 3.3 shows an AFM image of BSM molecules adsorbed on a Ni-treated mica surface. BSM was adsorbed on mica surfaces from very dilute solution with concentration lower than 0.01 mg/mL. Before adsorption, the mica surfaces were immersed in 2mM solution of $NiCl_2$ in purified water for 30 sec, rinsed with purified water, and dried with nitrogen. Such treatment favors the adsorption of isolated mucins parallel (flat) to the surface due to attraction between the negatively charged PTS domains of mucins and cationic surface sites of the Ni-treated mica.[10,11]

The adsorbed molecules appeared as linear objects. Local departures from the linear shape and small globular features were frequently observed along the molecule axis (Fig. 3.3b). These features were randomly distributed along the molecule and at their ends, or were completely absent. In Fig. 3.4, BSM molecules were aligned by the flow created upon rinsing with purified water and subsequent drying with nitrogen. In this case,

molecules were straightened and flattened. These observations suggest that nonlinear and globular regions corresponded to bends, coils and twists of the randomly coiled protein chain (Fig. 3.3b), that could not be resolved by AFM and were unfolded by flow. The height of flat (globule-free) molecular segment was uniform, h = (3.4 ± 1.1) Å, and consistent with the value h< 1 nm reported for other mucins imaged in air.[11] The cross-sectional width of the molecules, w = 7-8 nm, was much larger than h due to shape convolution effects between the molecule and the spherical AFM tip with radius ~10 nm.[12]

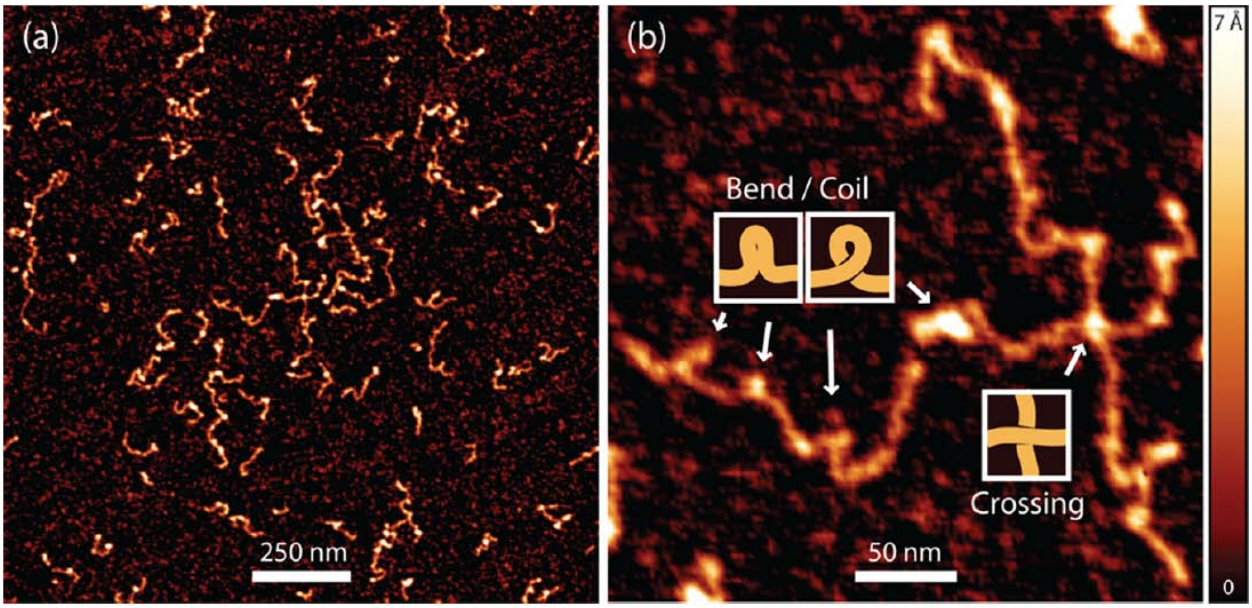

Figure 3.3. (a) AFM image of BSM molecules adsorbed on NI-treated mica from dilute neutral PBS solution. (b) Magnification showing recurring morphological features. The height relative to the mica substrate is color-coded as shown by the color bar to the right.

Flat isolated molecules with uniform height h were always linear and unbranched (Fig. 3.4b), with contour lengths varying over a wide range from a few tens of nanometers to

about 1 μm. These observations indicate that the BSM molecules aggregated mainly by pairwise association of their ends (as opposed to branched or star-like aggregation). Branching was always associated with nonflat globular features with height 7-12 Å that could not be distinguished from random crossing or overlapping of the molecules (Fig. 3.3b).

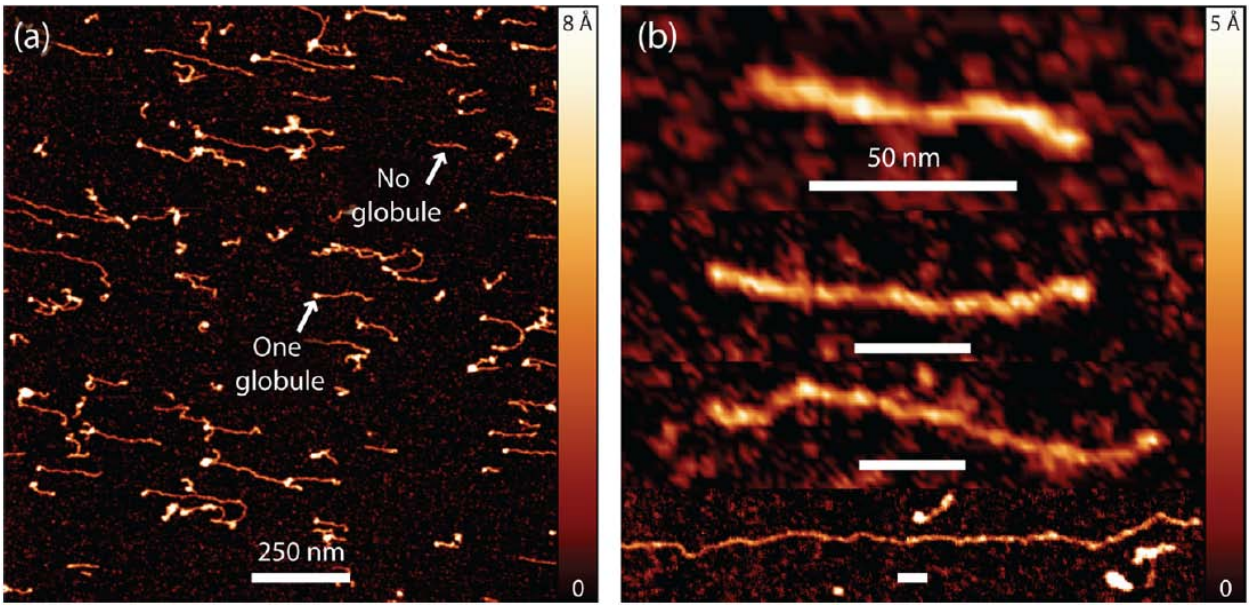

Figure 3.4. (a) AFM image of BSM molecules adsorbed on NI-treated mica from dilute neutral PBS solution. Molecules were aligned upon rinsing/drying the surface. (b) Individual molecules and aggregates adsorbed in a flat confirmation. The horizontal scale bar is 50 nm in all images. The vertical color bars show the height scale.

Fig. 3.5 shows the distribution of contour length *l* for isolated BSM molecules, that is, molecules that did not overlap any other molecule and were entirely exposed (with both ends visible) within an AFM image. The accuracy of *l* was limited by the fact that AFM could not resolve the "hidden" length involved in bends, coils, and globules that

frequently decorated the BSM molecule (Fig. 3.3b and 3.4a). We limited the analysis to molecules that showed variations of height and width smaller than 2*h* and 2*w*, respectively, and molecules showing at most one globular feature, that is, a region with height and width larger than *h* and *w*, respectively.

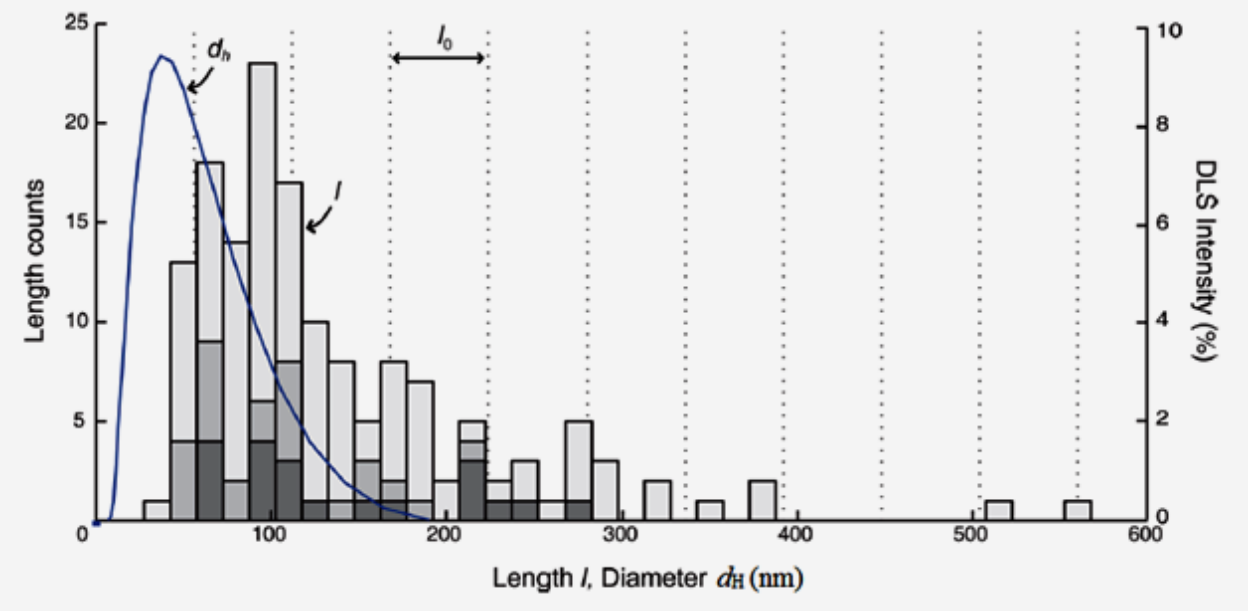

Figure 3.5. Distribution of contour length *l* for isolated BSM molecules. Dark gray indicates flat molecules (without globular features) straightened by fluid flow. Medium gray indicates flat molecules (straightened or not). Light gray indicates molecules with at most one globule. Vertical dashed lines are located at values of *l* multiple of l_0 = 55 nm. The solid line is the distribution of hydrodynamic diameter d_H measured by DLS in neutral solutions (from Figure 3.1).

The length distribution showed a main peak in the range *l* = 40-180 nm with the maximum at l_m = (95 ± 10) nm and a long tail extending beyond 300 nm. Both l_m and the peak width were about twice as large as those measured by DLS for the distribution of

hydrodynamic diameter d_H (solid line in Fig. 3.5). The distribution of contour length also showed local maxima at multiples of the length $l_0 \approx 55$ nm (Fig. 3.5). These peaks were more pronounced for molecules without globular domains and molecules straightened by fluid flow, that is, when the accuracy of l was higher. These results suggest that a molecular species with contour length close to l_0 was either more abundant or more active in forming pairwise end-to-end aggregates. We point out that the distribution of l also included molecules whose lengths were clearly not multiple of l_0, such as the one shown at the top of Fig. 3.4b (l = 97 nm). It is not clear whether these species were molecular fragments created during extraction and purification, distinct mucin types that were not differentiated by the purification process, or BSM variants encoded by the BSM gene.[13,14]

3.7 Surface force measurements

Fig.3.6a shows the force F, normalized by the radius of curvature R of the surfaces, as a function of the mica-mica separation distance D after adsorption of BSM from a 1.8 mg/mL solution in neutral PBS. The force became repulsive and consistently larger than the threshold of 0.05mN/m (Section 1.6.4) when the adsorbed BSM layers touched each other at a distance $D = 2T = (120 \pm 10)$ nm, and increased as D was decreased (Fig. 3.6b). Therefore, the layer thickness was approximately equal to $T = (60 \pm 5)$ nm. The same force curve $F(D)$ was measured upon approaching and retracting the surfaces over many approach/retraction cycles. The absence of hysteresis or viscous response indicates that the measurements were done under equilibrium conditions.

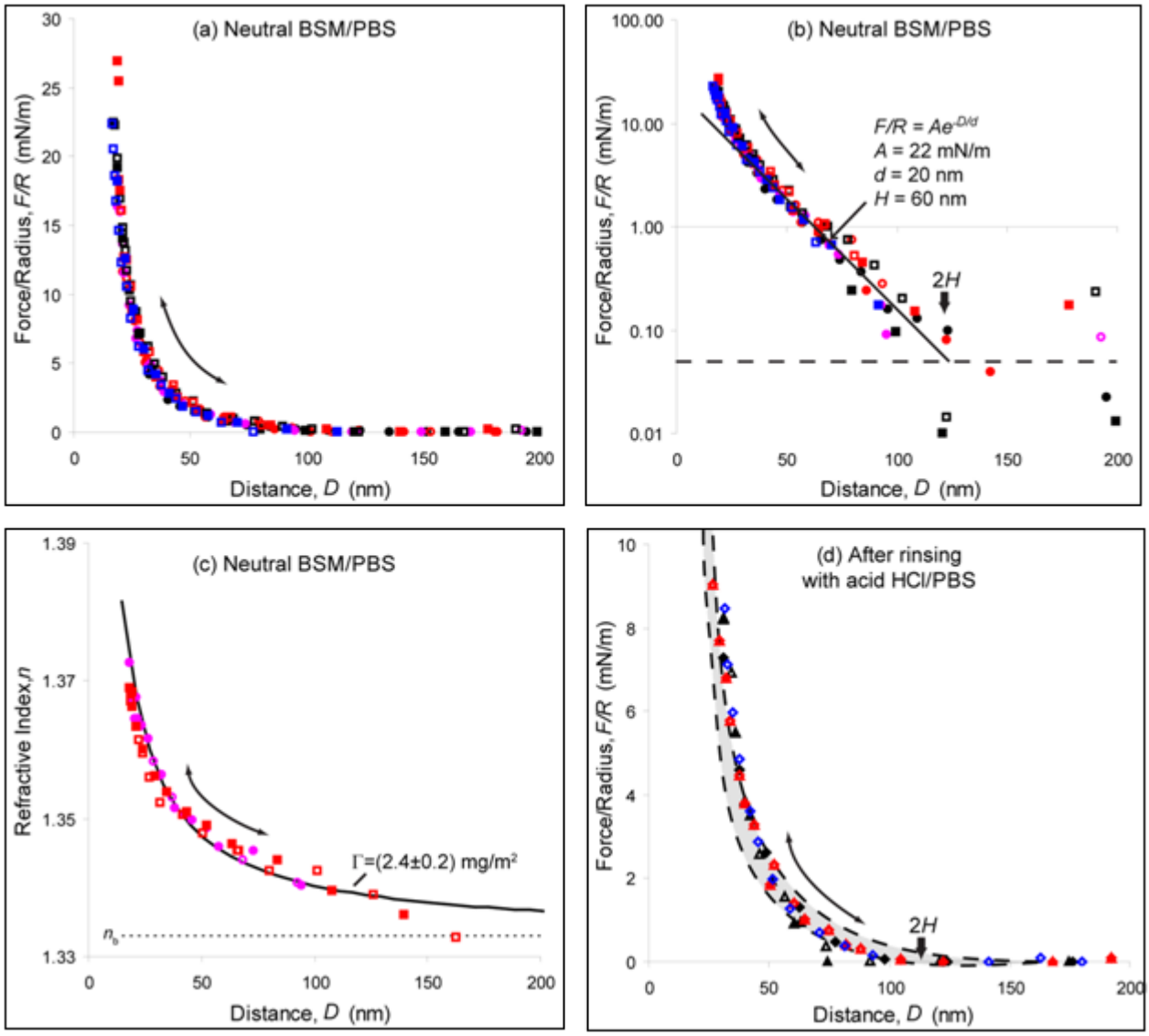

Figure 3.6. (a) Normalized force *F/R*as a function of the mica-mica distance D after adsorption of BSM from 1.8 mg/mL solution in PBS with pH 7.4. Different symbols indicate different experiments or contact positions. Each color represents a different approach/retraction cycle. Filled and open symbols indicate surface approach and retraction, respectively. (b) Semilogarithmic plot showing the exponential decay of *F* for large D. $2T$ is the onset of repulsion. (c) Refractive index *n* as a function of D. The dotted and solid lines indicate respectively the values expected in the absence of adsorption $(n = n_b = 1.333)$ and for the

indicated surface coverage Γ. (d) Force curve obtained after rinsing with protein-free HCl/PBS with pH 2.9. The shaded area contains all data points obtained before rinsing.

BSM layers could repeatedly withstand normalized loads as high as 30 mN/m and layer deformations $\delta = (2T - D_{\min})/2 =$ (120−36)/2 nm = 42 nm without being permanently altered, corresponding to an average pressure $P = F/S \approx$ 60 kPa over the contact area $S = 2\pi R\delta \approx 4600\,\mu m^2$, where R ≈ 2 cm. The force curve increased almost exponentially as D was decreased from 125 nm to about 35 nm: $F/R = A \cdot e^{-D/d}$ with a decay length d = 20 nm and prefactor (amplitude) A = 22 mJ/m (Fig. 3.6b). As D was further decreased, F increased faster than exponentially. The refractive index n increased above the bulk value n_b as D was decreased (Fig.3.6c). By fitting the $n(D)$ curve, with the formula[15] (Eq. 1.26)

$$n = n_b + (2\Gamma / D)\, dn/dC \qquad (3.1)$$

the surface coverage Γ of BSM on mica can be determined, where $n_b = n_w$ = 1.333 is the refractive index of the bulk protein solution, close to the value n_w of water, and dn/dC= 0.150 cm^3/g is the refractive index variation as a function of BSM mass concentration.[16] A fit of the $n(D)$ curve with Eq. 1 gave a surface coverage Γ = (2.4 ± 0.2) mg/m^2. The protein mass density in the adsorbed layers was $\rho = \Gamma / T$ = 40 mg/mL, that is 24 times larger than that in the bulk (Table 3.1).

Adsorption from more concentrated (2.2 mg/mL) or more dilute (0.15 mg/mL) neutral BSM/PBS solutions produced similar force curves with layer thickness T, amplitude A

and decay length d decreasing as the concentration decreased (Fig.3.7). Rinsing the surfaces with protein-free neutral PBS did not alter the force profiles, showing that BSM molecules were not desorbed upon rinsing and unadsorbed molecules could be flushed away upon rinsing without affecting the normal forces.

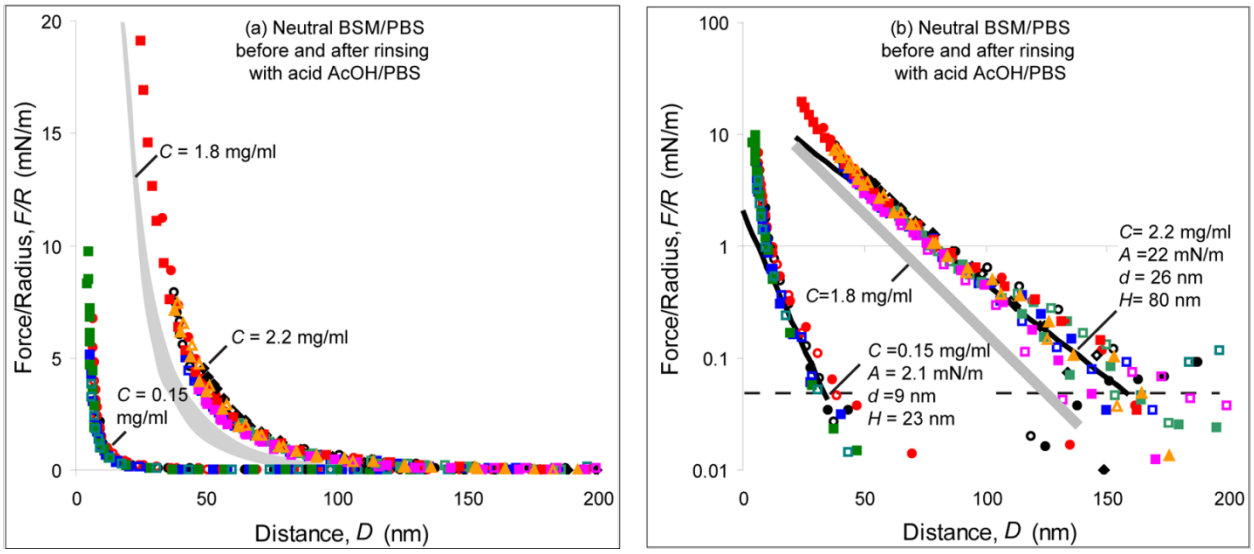

Figure 3.7. (a) Normalized force F / R measured as a function of the mica-mica separation D for neutral BSM/PBS solutions at different concentrations after adsorption(●/○, ◆/◇) and after rinsing (■/□, ▲/△) with protein-free acid AcOH/PBS at pH 2.6. (b) Semilogarithmic plot showing the exponential decay of F for large D. The shaded area in (a) and dashed line in (b) represents the data of Fig. 3.6.

Moreover, when a BSM layer adsorbed from neutral PBS was rinsed with protein-free acid HCl/PBS (Fig.3.6d) or AcOH/ PBS (Fig.3.7), the force curves did not show any significant change.

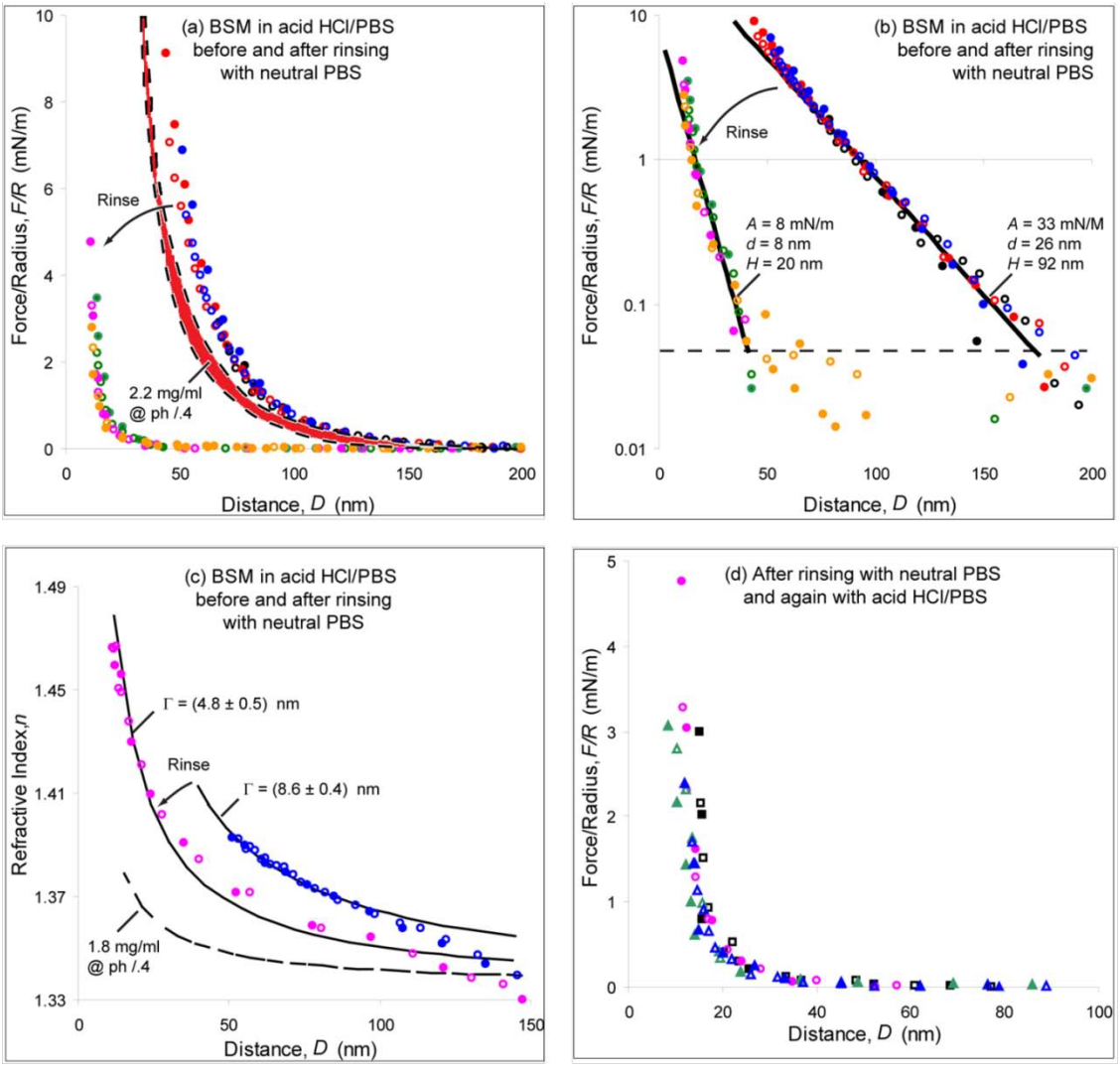

Figure 3.8. (a) Normalized force F/R measured as a function of the mica-mica separation D after adsorption of BSM from 2.0 mg/mL acid HCl/PBS solution and after rinsing with neutral PBS. In all figures, the red shaded area and dashed line represents the data obtained after adsorption from neutral BSM/PBS solutions. (b) Semi-logarithmic plot of the force curves showing the exponential decay of $F(D)$. (c) Refractive index n as a function of D. Solid lines correspond to the values calculated for the indicated values of surface coverage Γ. (d) Comparison of the forces obtained after rinsing with neutral PBS (circles and squares) and after rinsing again with acid HCl/PBS (triangles).

Adsorption from low pH, despite the shorter adsorption time, produced layers with greater surface coverage Γ, larger thickness T, density ρ, prefactor A of the exponential force and a relatively small increase of the decay length d (Fig.3.8a-c and Table 3.1). After rinsing with protein-free neutral PBS, all parameters decreased due to desorption of BSM from the layers. The force became less repulsive (Fig. 3.8a) but the surface coverage remained larger than for BSM layers adsorbed from neutral solution (Fig. 3.8c), suggesting a different layer structure. When the layers were rinsed again with protein-free acid HCl/PBS, the force did not change (Fig.3.8d).

3.8 Discussion

3.8.1 Single molecule

Because of the heavy glycosylation of the PTS domain, BSM molecules can be considerably more rigid than ungylcosylated proteins. Strongly hydrated and negatively charged sugar groups of the PTS domain repel each other by steric and electrostatic interactions that restrict the range of orientation angles between consecutive amino acids along the polypeptide chain. As a consequence, mucins are often described as "wormlike" semiflexible polymer chains (Section 1.2) with contour length s and persistence length l_P approaching the limit $s/l_P \approx 1$.[9,17-20] In fact, l_P is of the order of 10 nm, much larger than the value $l_P \approx 0.4$ nm for non mucins, unstructured proteins.[9,11,18] For $s/l_P >> 1$, a wormlike chain forms an ideal random coil (Section 1.2) with radius of gyration $R_g \approx (l_P\, s)^{1/2} << s$ (neglecting the chain self-avoidance), whereas for $s/l_P << 1$ the chain behaves like the

rigid rod with $R_g \approx (s^2/12)^{1/2} \approx s$.[21] Calculations show that for all values of s/l_P, the ratio of $d_H/2R_g$ is in the range 1-3.5, where the lower bound corresponds to the rigid rod limit.[22] Our findings that both the maximum point (d_{max}) and the width of the distribution of d_H (Fig. 3.1) are about half the corresponding values in the distribution of s (Fig. 3.5) indicates that BSM should be considered as a stiff chain with $s/l_P \geq 1$ and $d_H \approx 2R_g \approx s$, rather than a polymer-like random coil with $s/l_P >> 1$ and $R_g << s$.

The hydrodynamic diameter and molar weight of BSM monomers have previously been reported to be d_H = 40-76 nm and MW = 0.8-2.0 MDa, respectively.[8,23] While the diameter compare well with the values of d_m and d_z obtained in the present study (Table 3.1), MW seems too high for the short contour length measured by AFM, s < 300 nm (Fig.3.5). Indeed the length of the PTS domain increases approximately as $s = pN$ where N is the number of monomeric residues in the domain prior to glycosylation and $p \approx$ 0.25 nm/residue is the typical pitch of the wormlike chain.[9] If we consider an average molar mass of 120 g/mol for amino acids in the PTS domain and $N = s / p \approx 100/0.25 =$ 400, the molecular weight of the PTS domain is about 50 kDa, excluding carbohydrate chains. If we further suppose that the peptides in the end domains have the same mass as those in PTS domain and the percentage of glycans in the total molecular weight is 50−80%, the total MW of BSM can be estimated from AFM images to be 200−500kDa.

3.8.2 Nanomechanics of adsorbed BSM layers

BSM has an isoelectric point IEP ≈ 3 and is negatively charged at neutral pH due to the abundance of sialic acid in the PTS domain. BSM also contains many positively charged

and hydrophobic residues in the end domains. Since the mica surface is also negatively charged in water (IEP ≈ 3),[24] the adsorption of BSM on mica at neutral pH is likely due to binding of the end domains (Fig. 3.9).[2,25,26]

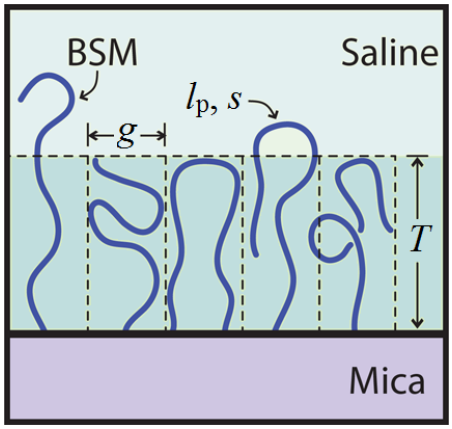

Figure 3.9. Schematic representation of BSM molecules adsorbed on mica from PBS solution. s and l_p are the average contour length and persistence length of a single molecule. Molecules are grafted to the substrate by their ends at an average distance g from each other. T is the height of the adsorbed layer.

The surface coverage Γ is higher than the values measured on silica surfaces in saline solution,[16,27] despite silica having a higher surface density of negative charges.[28,29] This suggests that non-electrostatic interactions also contribute to BSM-mica adsorption interaction.[5]

The repulsive force between two surfaces coated with end-grafted polymer molecules can be described with two different models depending on the ratio ($2R_g$ / g) between the radius of gyration in solution and the grafting distance g on the surface (Fig. 3.9). When $2R_g / g < 1$, the layer is dilute and the force is given by[8]

$$\frac{F}{R} = Ae^{-D/d} = 72\pi kT \frac{e^{-D/R_g}}{g^2} \qquad (3.2)$$

for distances such that D/R_g= 1-4. For $2R_g / g > 1$, the layer is dense (or "semidilute") and the lateral interaction between adsorbed molecules forces them to stretch along the substrate normal, forming a "brushlike" layer. The force is given by

$$\frac{F}{R} = Ae^{-D/d} = 64\pi kT \frac{Te^{-\pi D/T}}{g^3}, \qquad \text{with } T = s(l_p / g)^{2/3} \qquad (3.3)$$

for distances $D/2T$ = 0.2-0.9, where T is the layer thickness. On one hand, BSM layers adsorbed from neutral solution (concentration 1.8-2.2 mg/mL) produced an exponentially repulsive force with decay length comparable to the gyration radius, d = 20-26 nm ≈ $d_m/2$ (Fig. 3.6b and 3.7b, and Table 3.1), in agreement with the dilute layer model (Eq. 3.2). On the other hand, BSM display a rigid rod-like conformation in solution and may sustain such confirmation after being adsorbed onto mica surface, even in dilute regime. Thus, primarily owing to its stiff unique confirmation rather than grafting density, BSM may stretch and form rigid layers that are semidilute and brushlike (Fig. 3.9). Indeed, the layer thickness T is comparable to the contour length s and the decay length is $d \approx T/\pi \approx s/\pi \approx$ 30 nm, as in Eq. 3.3. Therefore, both the dilute and brush layer model can be fitted to the force curves. The prefactor A = 22 mN/m of the normalized force can be obtained with g = 6.4 nm in Eq.3.2, or g = 13 nm and T = 60 nm in Eq. 3.3. The molecular weight estimated from the relationship MW = $N_A \Gamma g^2$ with the experiment value Γ = 2.4mg/m^2 (Table 3.1) is 60 kDa in the dilute layer case and 250 kDa in the

brush layer case. Therefore, the brushlike description of the adsorbed layer is more consistent with the molecular weight estimated from the morphology imaging by AFM (subsection3.6.1). For both the dilute and brush layer models, F increases faster than an exponential for $D/R_g \ll 1$ or $D/T \ll 1$,respectively, as observed in all force curves.

When BSM was adsorbed from dilute solution, T = 23 nm was comparable to d_H but the decay length was $d < d_H/2$ (Fig. 3.7), in contrast to what expected for a dilute layer (Eq.3.2).Moreover, the force showed a second exponential regime for D < 20 nm with a shorter decay length of about 4 nm. Most likely, the conformation of BSM molecules in the dilute layers varied during surface approach, e.g. molecules became more parallel to the surface, thereby changing the mechanical response to the external compressive load.

3.8.3 Effect of acidification

At pH < 3, more than half of the negative charges in the PTS domain are neutralized. The bonding rigidity and persistence length l_p are expected to decrease as a result of reduced electrostatic repulsion between neighboring negatively charges sugar chains along the protein chain. Therefore, the hydrodynamic diameter is expected to decrease. While this was indeed observed, the variation $\delta d_m/d_m \approx -0.11$ was small (Fig. 3.1 and Table 3.1). In the limit of $s/l_p \approx 1$, this variation corresponded to a comparable decrease of the persistence length $\delta l_p/l_p \approx \delta d_m/d_m \approx -0.1$. Such small variation indicates that steric hindrance between sugar chains is more important than electrostatic repulsion in determining the persistence length l_p at the physiological salinity of our solutions, in agreement with similar results obtained for previous studies on BSM[30] and OSM.[9] It is

worth noting here that the Debye length, $\lambda \approx 1$ nm, may be shorter than the average spacing between neighboring charged residues along the polypeptide chain, so that electrostatic interactions between these residues may be effectively screened both at low and neutral pH.

The conformation of isolated chains molecules and stability of adsorbed layers of chains depend on intramolecular interactions between nonconsecutive segments (far from each other along the same chain) and intermolecular interactions between segments belonging to different chains. These interactions modify the effective excluded volume per segment that plays a central role in Flory theory of real polymer chains (Section 1.4) and are commonly referred to as "excluded volume" effects.[21] Within an isolated wormlike chain molecule with $s/l_p \approx 1$, such as BSM in solution, the number of "contacts" between nonconsecutive segments is relatively small and intersegment interactions can be neglected. In fact, the worm-like chain model is considered a model of ideal chain (no excluded volume) as opposed to real polymer chain (including excluded volume effects). On the other hand, the protein mass density, ρ inside adsorbed BSM layers (Table 3.1) is much larger than the density $MW/(N_A s^3) \approx 1$ mg/mL ("overlap"density[21]) inside the volume pervaded by an isolated wormlike BSM molecule in solution, that is of the order of s^3. Therefore, the probability of contact is high and intersegment interactions may play an important role. Indeed adsorbing from acid solution, that is, neutralizing negative charges and reducing electrostatic repulsion between acidic PTS segments, led to higher density ρ (higher volume fraction ϕ) of BSM molecules in the layer (Table 3.1). The

density increase may also be due to stronger attractive interactions between BSM and mica at low pH, due to charge neutralization and decreased repulsion of negative charges of both BSM and mica. However, the density increase was observed also for BSM adsorbing on uncharged apolar surfaces at low pH, where BSM-mica interactions are not expected to be pH-dependent.[16] Therefore, the density increase appears to be driven mainly by intersegment interaction.

Inside the densely packed layers, end-to-end association (Fig. 3.5) is much more likely to occur than in solution, increasing the contour length s of the worm-like chains. The volume fraction ϕ inside an adsorbed polymer layer is expected to depend on the excluded volume per segment, which does not depend on s.[21]Therefore, a pH-dependent increase of s due to end-to-end association cannot explain the density increase at low pH. On the other hand, acidification favors aggregation in solution (Fig.3.1) and may induce the formation of long chains at the surface, increasing the thickness of the layer: $T \propto s$ (Eq.3.3).

Desorption was observed upon rinsing with neutral solution a layer adsorbed from acid solution (Fig.3.8a and b). In this case, electrostatic repulsion between PTS domains was restored and osmotic pressure inside the layer increased to a point that BSM−mica adsorption interactions were not sufficient anymore to stabilize the layer structure. BSM−mica interaction may also become more repulsive as the pH is increased and negative charges are restored on both BSM and mica. However, as previously noted,

changes in adsorption density can be also induced for BSM layers adsorbed on uncharged surfaces.[16]

It is noteworthy that rinsing with acidic solution a layer that was stable at neutral pH (Figs.3.6d, 3.7, and 3.8d) did not produce any desorption because rinsing reduced the electrostatic repulsion and osmotic pressure. Moreover, the normal forces, F remained almost unaltered after acidification (Figs. 3.6d, 3.7, and 3.8d). In fact, F depends on pH via the grafting distance g and contour length s (Eq.3.2 and 3.3), since the persistence length l_p and gyration radius R_g do not significantly change upon acidification. Rinsing with protein-free acid solution did not produce desorption (i.e., g remained constant)and could not induce chain elongation (s can increase only when proteins are added to the layer from the solution) or chain shortening/fragmentation (acidification enhances association, Fig.3.1). Therefore, the force F could only remain constant upon acidification of a layer adsorbed at neutral pH.

3.9 Conclusions

Understanding the molecular-scale mechanisms underlying the surface properties of mucins such as hydration,[31] mucoadhesion,[32] and lubrication[33,34,35] is crucial for the biomimetic development of biocompatible, environment-friendly polymeric materials and coatings for water-based applications.[36-38] In this study, we investigated the relation between the structure and properties of single BSM molecules, and the nanomechanics of dense BSM layers adsorbed on charged surfaces such as mica. Using highly purified

BSM was essential to minimize the influence of nonmucin impurities. Complementary observations by DLS, CD and AFM revealed that BSM molecules behave as rigid "wormlike" polypeptide chains lacking a defined protein structure, due to the heavy glycosylation of the central PTS domain. The persistence length of the domain was not affected by acidification at physiological salinity, indicating that the stiffness of the PTS domain is mainly due to steric hindrance between acidic side sugar chains, rather than their mutual electrostatic repulsion. Using the SFA study, we have shown that BSM readily adsorbs on mica with a density much higher than the overlap concentration. Strong, long-ranged, reversible (elastic) repulsive forces are generated between BSM-coated surfaces, which can be modeled using current theories for polymer-like molecules. Intersegment interactions(i.e., excluded volume effects) were found to play a significant role during BSM adsorption, leading to a higher adsorbed mass density at low pH due to reduced electrostatic repulsion between PTS domains. Conversely, increasing the pH after adsorption restored electrostatic repulsion and induced desorption. Remarkably, acidification of the layers adsorbed from neutral solution did not produce desorption or variations of the repulsive forces. Such ability of BSM to remove adhesion and prevent the direct contact between two surfaces during compression, and the stability against acidification can be linked to the native function of BSM in the oral cavity as a surface protective and lubricating agent at work in variable pH conditions.

References

[1] Zappone, B.; Patil, N. J.; Madsen, J. B.; Pakkanen, K. I.; Lee, S. *Langmuir* **2015**, 31, 4524−4533

[2] Perez, E.; Proust, J. E. *J. Colloid Interface Sci.* **1987**, 118, 182−191.

[3] Caldwell, K. D.; Sandberg, T.; Hellstrom, J.; Tengvall, P.; Andersson, J. *Abstr. Pap. Am. Chem. Soc.***2003**, 225, U712−U712.

[4] Proust, J. E.; Baszkin, A.; Perez, E.; Boissonnade, M. M. *Colloids and Surfaces,*.**1983**, 10, 43-52.

[5] Durrer, C.; Irache, J. M.; Duchene, D.; Ponchel, G. *J ColloidInterf. Sci.***1995**, 170, 555-561.

[6] Lindh, L.; Glantz, P-O.; Carlstedt, I.; Wickström, C.; Arnebrant, T. *Colloids Surf. B* **2002**, 25, 139-146.

[7] Madsen, J. B.; Pakkanen, K. I.; Duelund, L.; Svensson, B.; AbouHachem, M.; Lee, S. *Prep. Biochem. Biotechnol.* **2015**, 45, 84−99.

[8] Israelachvili, J. N. *Intermolecular and Surface Forces*, 3rd ed.; Academic Press: London, **2011**.

[9] Shogren, R.; Gerken, T. A.; Jentoft, N. *Biochemistry* **1989**, 28, 5525−5536.

[10] McMaster, T. J.; Berry, M.; Corfield, A. P.; Miles, M. J. *Biophys. J.* **1999**, 77, 533−541.

[11] Round, A. N.; Berry, M.; McMaster, T. J.; Stoll, S.; Gowers, D.; Corfield, A. P.; Miles, M. J. *Biophys. J.* **2002**, 83, 1661−1670.

[12] **http://afmhelp.com.**

[13] Hoorens, P. R.; Rinaldi, M.; Li, R. W.; Goddeeris, B.; Claerebout, E.; Vercruysse, J.; Geldhof, P. *BMC Genomics* **2011**, 12, 140−151.

[14] Jiang, W. P.; Gupta, D.; Gallagher, D.; Davis, S.; Bhavanandan, V. P. *Eur. J. Biochem*. **2000**, 267, 2208−2217.

[15] de Feijter, J. A.; Benjamins, J.; Veer, J. A. *Biopolymers* **1978**, 17, 1759−1772.

[16] Sotres, J.; Madsen, J. B.; Arnebrant, T.; Lee, S. *J. Colloid Interface Sci.* **2014**, 428, 242−250.

[17] Sheehan, J. K.; Brazeau, C.; Kutay, S.; Pigeon, H.; Kirkham, S.; Howard, M.; Thornton, D. J. *Biochem. J.***2000**, 347, 37−44.

[18] Cao, X. X.; Bansil, R.; Bhaskar, K. R.; Turner, B. S.; LaMont, J. T.; Niu, N.; Afdhal, N. H. *Biophys. J.***1999**, 76, 1250−1258.

[19] Bettelheim, F. A.; Hashimoto, Y.; Pigman, W. *Biochim. Biophys. Acta* **1962**, 63, 235−242.

[20] Thornton, D. J.; Howard, M.; Khan, N.; Sheehan, J. K. *J. Biol. Chem.***1997**, 272, 9561−9566.

[21] Rubinstein, M.; Colby, R. *Polymer Physics*; Oxford: New York, **2003.**

[22] Amoros, D.; Ortega, A.; de la Torre, J. G. *Macromolecules* **2011**, 44, 5788−5797.

[23] Caldwell, K. D.; Sandberg, T.; Hellstrom, J.; Tengvall, P.; Andersson, J. *Abstr. Pap. Am. Chem. Soc.***2003**, 225, U712−U712.
[24] Pashley, R. M. *J. Colloid Interface Sci.***1981**, 83, 531−546.
[25] Lundin, M.; Sandberg, T.; Caldwell, K. D.; Blomberg, E. *J. Colloid Interface Sci.***2009**, 336, 30−39.
[26] Dedinaite, A.; Lundin, M.; Macakova, L.; Auletta, T. *Langmuir* **2005**, 21, 9502−9509.
[27] Sandberg, T.; Blom, H.; Caldwell, K. D. *J. Biomed. Mater. Res., Part A* **2009**, 91A, 762−772.
[28] Toikka, G.; Hayes, R. A. *J. Colloid Interface Sci.***1997**, 191, 102−109.
[29] Acuna, S. M.; Toledo, P. G. *J. Colloid Interface Sci.***2011**, 361, 397−399.
[30] Perez-Vilar, J.; Hill, R. L. *J. Biol. Chem*. **1999**, 274, 31751−31754.
[31] Shi, L.; Caldwell, K. D. *J. Colloid Interface Sci.***2000**, 224, 372−381.
[32] Li, D. X.; Yamamoto, H.; Takeuchi, H.; Kawashima, Y. *Eur. J. Pharm. Biopharm*. **2010**, 75, 277−283.
[33] Lee, S.; Muller, M.; Rezwan, K.; Spencer, N. D. *Langmuir***2005**, 21, 8344−8353.
[34]Yakubov, G. E.; Mccoll, J.; Bongaerts, J. H. H.; Ramsden, J. J. *Langmuir***2009**, 25, 2313−2321.
[35] Nikogeorgos, N.; Madsen, J. B.; Lee, S. *Colloids Surf., B* **2014**,122, 760−766.
[36] Ron, T.; Javakhishvili, I.; Patil, N. J.; Jankova, K.; Zappone, B.; Hvilsted, S.; Lee, S. *Polymer* **2014**, 55,4873−4883.
[37] Javakhishvili, I.; Ron, T.; Jankova, K.; Hvilsted, S.; Lee, S. *Macromolecules* **2014**, 47, 2019−2029.
[38] Ron, T.; Javakhishvili, I.; Jankova, K.; Hvilsted, S.; Lee, S. *Langmuir* **2013**, 29, 7782−7792.

CHAPTER 4

Enhanced Boundary Lubrication of Porcine Gastric Mucin via Complexation with Polyethylenimine in Neutral Aqueous Solution

4.1 Introduction

Porcine gastric mucin (PGM) is the most important sub units of gastric mucus of pig, secreted by the gastric epithelium. PGM can be acquired in different ways; commercialized crude isolated PGM or natural PGM scraped off a pig stomach. However, commercially available dried PGM, from which mucin solutions can be readily made are widely used in several mucin-related studies. The detailed description of mucin glycoproteins can be found in ref.[1,2,3].

Mucoadhesion is the ability of materials to adhere to mucosal membranes in the body and provide a temporary retention. This property has been widely used to develop polymeric dosage forms for buccal, oral, nasal, ocular and vaginal drug delivery.[4] Cationic polymers such as chitosan and some synthetic polymethacrylates have been reported to show excellent mucoadhesive performance.[4] Electrostatic attractions appears to be major mechanism for mucoadhesion of cationic polymers like chitosan with negatively charged mucins like PGM and BSM, but is also reinforced by contributions from hydrogen bonding and hydrophobic effects.[4.5]

Many diseases, especially genetic disorders, are closely associated with the absence of specific proteins or enzymes and can be cured by delivering a gene encoding the protein or enzyme to the patient. Polyethylenimine (PEI) has emerged as the choice transgene delivery agent or transfection reagent for mammalian cells[6] as well as optimum therapeutics due to its strong interaction with mucins.[7] A rich literature is available on PEI, both for the linear and branched form, with different molecular weights (MW = 2-1600 kDa) and functional chemical groups. Branched PEI (b-PEI) with MW=25 kDa obtained via cationic ring-opening polymerization of aziridine (ethylene imine)[8] is the form commonly utilized in various biomedical applications.

PGM was reported to exhibit effective aqueous lubricating properties under acidic pH and low ionic strengths.[9] A previous study on PGM and cationic mucoadhesive polymer chitosan displayed excellent lubricating properties at pH 3.2 (chitosan is insoluble at neutral pH) and low concentration where total concentration of mixture was 0.1 mg/mL.[5] The aim of the present study was to understand the interaction between PGM and b-PEI form the point of view of aqueous lubrication at neutral pH. Macroscale lubricating properties of the PGM:b-PEI mixture between soft (polydimethylsiloxane, PDMS) elastomer surfaces was studied using pin-on-disk tribometry (Section 1.7). The lubricating properties of mixtures were tested at various shearing velocities as a function of PGM:b-PEI mixing ratios and in the presence of NaCl salt or chaotropic agent guanidine hydrochloride (GuHCl), which screens electrostatic interactions or breaks hydrogen bonds between interacting species in aqueous solution, respectively. Optical

waveguide lightmode spectroscopy (OWLS) (Section 1.8), circular dichroism (CD) (Section 1.11), dynamic light scattering (DLS) (Section 1.9) and ζ-potential measurements (Section 1.10) were conducted in parallel to probe the response of PGM/b-PEI interactions to variations of mixing ratios, salt and chaotropic agent concentration.

4.2 Sample preparation

Commercially available porcine gastric mucin (PGM Type III: partially purified, bound sialic acid 0.5-1.5%),branched polyethylenimine (b-PEI, nominal molecular weight, MW = 25000 g/mol) and (b-PEI, low molecular weight (LMW), MW = 800 g/mol) were purchased from Sigma-Aldrich (Denmark Aps, Brøndby, Denmark) were used as received from the manufacturer without. All other chemicals were of laboratory grade and were also purchased from Sigma Aldrich (Denmark Aps, Brøndby, Denmark).

Solutions of PGM and b-PEI were prepared at the concentration of 1 mg/mL. Phosphate buffer saline (PBS, 10 mM Na_2HPO_4 and 1.8 mM KH_2PO_4 in purified water without extra salts) with pH value adjusted to 7.2 was used as solvent for all polymer solutions. Mixture were prepared at [PGM:b-PEI] ratios of 1:1, 2:1 and 4:1 by mixing aliquots of PGM and b-PEI solutions prepared at 1 mg/mL. Thus, the ratios represent both weight ratio and volume ratio of each solution. The total biopolymer concentration in the final mixture was 1 mg/mL for all cases.

The 1:1 mixture was further investigated to study the influence of added NaCl salt (0.1M, 0.5M, and 1M) or chaotropic agent guanidine hydrochloride, GuHCl (6M, purity ≥ 99%,

Sigma-Aldrich, Brøndby, Denmark). Mixtures with salts were prepared prior to the measurements and continuously stirred for at least 5 min at room temperature. Samples containing b-PEI were protected from light. The solutions were not filtered and pH was adjusted by the addition of HCl or NaOH. Sample preparation and measurements were performed at room temperature and sample pH was adjusted to 7.2, unless otherwise stated.

4.3 Synergistic lubrication of PGM and b-PEI mixtures

Fig. 4.1A shows the friction coefficient, μ as a function of the sliding speed measured by pin-on-disk tribometry for the PDMS-PDMS tribopairs. In general sense, both PGM and b-PEI displayed poor lubricating capabilities. At speeds below 5 $mm \cdot s^{-1}$, corresponding to the boundary lubrication regime, the values of μ of both PGM and b-PEI were comparable to those of the sliding contact of PDMS-PDMS in PBS. Only at the highest speed (100 mm/s), the friction coefficient for PGM and b-PEI decreased to 0.02 and 0.015, respectively. Upon mixing PGM and b-PEI at ratios of 1:1, 2:1 and 4:1, however, a substantial decrease of μ was observed. All three mixtures showed superior lubrication, particularly in the boundary lubrication regime at low speeds (< 10 $mm \cdot s^{-1}$).

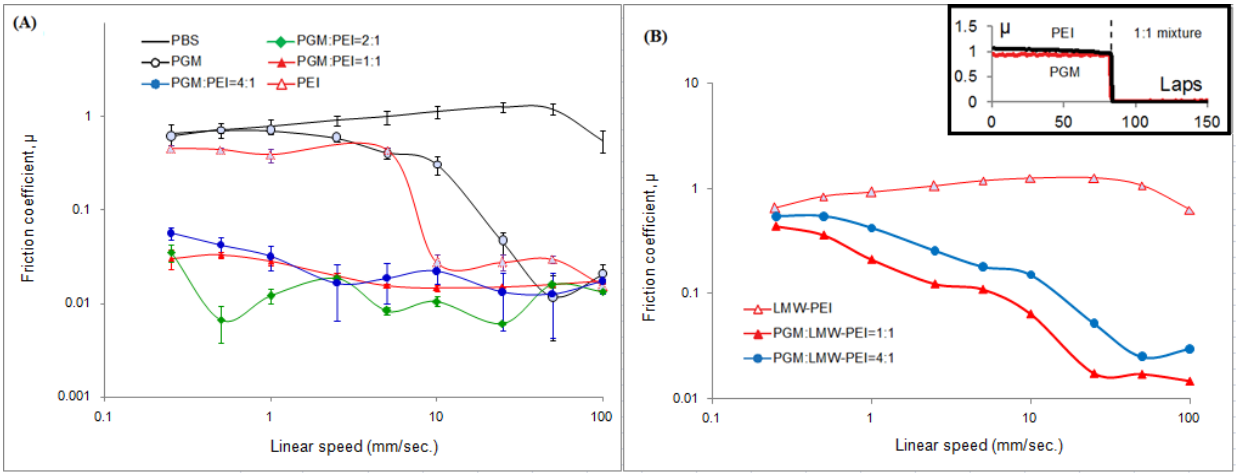

Figure 4.1 (A) Friction coefficient (μ) vs. linear speed for PDMS/PDMS sliding contact lubricated with PBS buffer solution (10 mM, pH 7.2), PGM, b-PEI and their mixtures at different ratios. **(B)** Measurements on low molecular weight (LMW) b-PEI and its mixtures with PGM. Inset: μas a function of the number of laps for the sequential adsorption of polymers. μ suddenly decreased when PGM and b-PEI were mixed during the friction test (speed 5 mm/s). Experiments were performed at constant pH of 7.2 and constant load F_{Load}= 1.

This synergetic lubricating effect between PGM and b-PEI is similar to that observed from PGM and chitosan in acid conditions in a previous report,[5] with two noteworthy differences. First, stable PGM:b-PEI mixtures were obtained at neutral pH whereas chitosan is soluble only at acid pH that is less relevant to applications. Second, the lubricating properties of PGM:chitosan mixtures declined as the PGM concentration was decreased from 4:1 to 1:1,[5] whereas 20% w/w of b-PEI (in 4:1 mixture) was sufficient to achieve maximum synergetic lubrication. Interestingly, the synergetic effect was less pronounced for b-PEI with lower molecular weight (800 g/mol) (1:1 mixing ratio, Fig. 4.1B).

In order to investigate the kinetics aspect of such synergy observed, PGM and b-PEI was injected to the sequentially as opposed to mixing them in advance. As shown in the Fig. 4.1B, the decrease in μ upon addition of the second polymer was instantaneous regardless of the order of addition (PGM or b-PEI).

4.4 Influence of ionic strength and chaotropic agent on the enhanced lubrication of PGM:b-PEI mixtures

Given that PGM and b-PEI are respectively polyanionic and polycationic at neutral pH, electrostatic attraction between them is thought to be involved in their interaction. Moreover, as hydroxyl, carboxylic, and various amine groups are abundant in PGM and b-PEI, hydrogen bonding may additionally contribute to the interaction between them. Thus, the influence of ionic strength and chaotropic agent on the lubrication of PGM:b-PEI mixtures was studied by adding either NaCl (from 0.1 M to 1.0 M) or 6 MGuHCl (Fig. 4.2)

The low salt concentration of 0.1M NaCl did not significantly affect the lubricating properties of the mixture, except for a slight increase in μ values at speed ≤ 0.5 mms^{-1}. As the concentration of NaCl was increased to 0.5M and 1 M, friction progressively increased at low speed. Addition of GuHCl led to an increase in μ comparable to that obtained by adding 1 M NaCl. This observation indicates that hydrogen bonding also contributes to PGM/b-PEI interaction and synergetic lubrication.

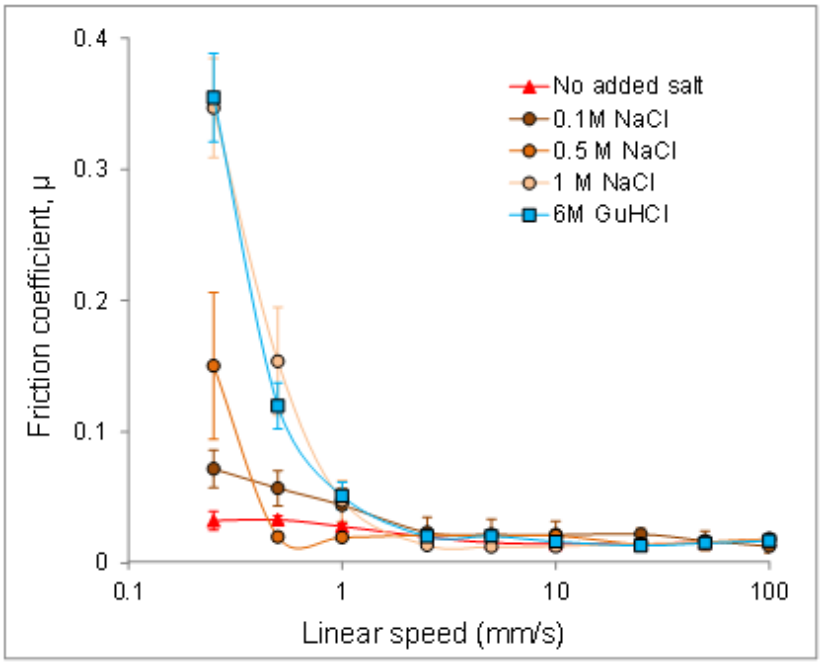

Figure 4.2 Friction coefficient (μ) vs. linear speed plot for PDMS/PDMS sliding contact obtained for 1:1 mixture of PGM and b-PEI with added NaCl (0.1M, 0.5M and 1M) or 6M GuHCl at pH 7.2. Data was obtained at a constant load F_{Load}= 1N and adsorption time of 10 min.

4.5 Surface adsorption of PGM, PEI and their mixtures

Given that synergetic lubricating effect between PGM and b-PEI was observed exclusively in low-speed boundary lubrication regime, it is crucial to understand the surface adsorption properties of the polymers onto the PDMS tribopair. In Fig. 4.3, the surface adsorbed masses (mg/m^2) for PGM, b-PEI, and their mixtures are presented. In these experiments, the adsorption time was limited to 15 min in order to emulate the surface adsorption conditions of the polymers under tribological stress, where desorption/(re)adsorption of the polymers onto PDMS is repeatedly established due to the cyclic tribostress, and the surface adsorption is far from equilibrium.[10] The adsorbed

mass of PGM(1.33 ± 0.37 mg.m^{-2}) was more than double that of b-PEI (0.43 ± 0.1 mg.m^{-2}) presumably because, unlike b-PEI, PGM has unglycosylated hydrophobic patches in the C- and N-termini that can bind to hydrophobic PDMS. PGM:b-PEI mixtures with mixing ratio 4:1 (1.72 ± 0.38 mg.m^{-2}) and 2:1 (1.69 ± 0.14 mg.m^{-2}) showed a slightly higher adsorbed masses than PGM or b-PEI alone, whereas the mass was more than double for 1:1 mixtures (2.95 ± 0.35 mg.m^{-2}). Since boundary lubrication showed a comparable enhancement for mixing ratios (Fig. 4.1A), it is not simply due to the increase in adsorbed mass.

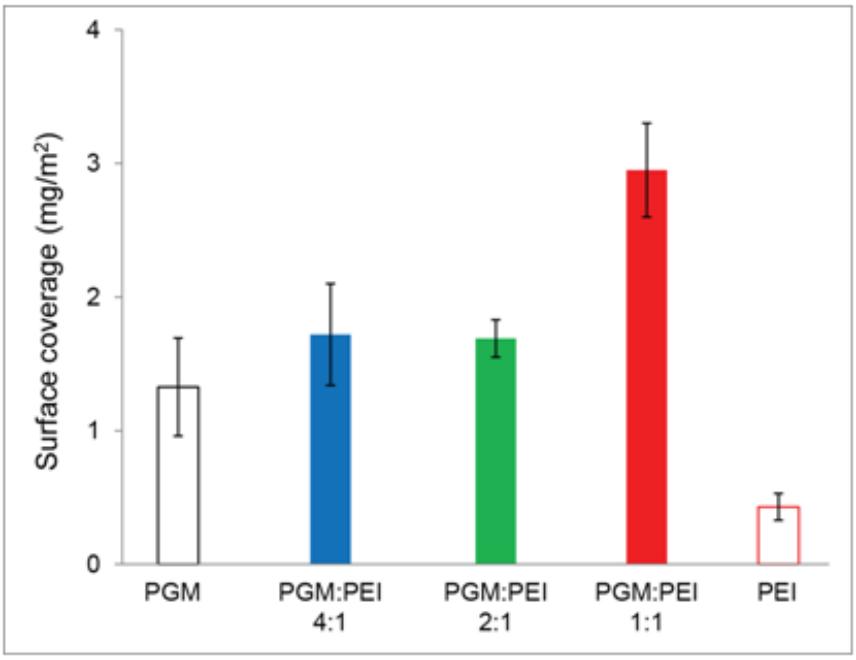

Figure 4.3 Adsorbed masses of PGM, b-PEI, and their mixtures at varying ratios onto PDMS-coated waveguides as determined by OWLS at pH 7.2.The adsorption time was 15 min.

PGM is known to be a poor lubricant for PDMS-PDMS tribopairs, especially at neutral pH and despite the significant amount of adsorbed mass.[9] This was attributed to weak

binding strength of PGM onto PDMS surface. Therefore, mixing of PGM with b-PEI may have an influence of improving the binding strength of the adsorbate compared to PGM alone. A strong complexation between PGM and b-PEI on PDMS surface can be assumed to be responsible for the improved lubricating properties of the PGM:b-PEI layer, similarly with the case of PGM:chitosan mixtures reported in a previous study.[5]

4.6 Conformational changes of PGM upon mixing with b-PEI

Fig. 4.4 shows the far-UV CD spectra of PGM, b-PEI, and mixture with 1:1 ratio. The concentration of polymer in solution was kept 1 mg/ml and pH was 7.2 in all cases.

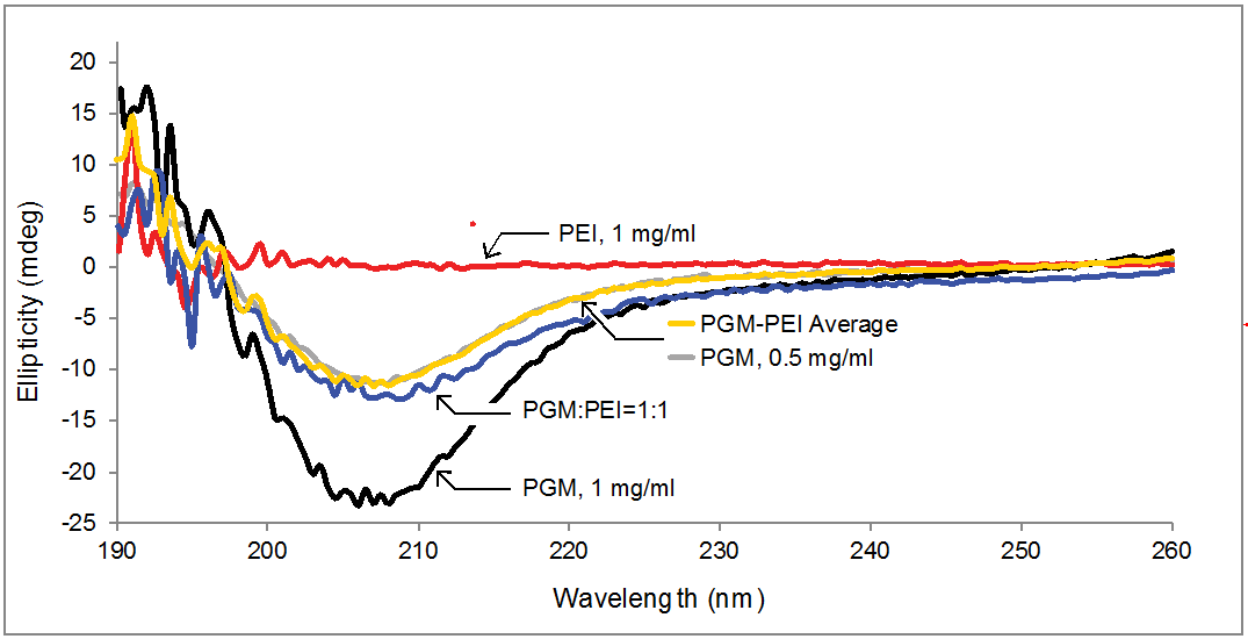

Figure 4.4 Far-UV CD spectra for PGM, b-PEI, and their 1:1 mixture. Numerical average is calculated as [(PGM + b-PEI), 1 mg/ml] / 2, and compared with the observed experimental curve for the 1:1 mixture.

The far-UV spectrum of PGM solution showed a single, broad negative peak with the minimum at 207 nm which represents a broadly defined random coil structure,[11] whereas b-PEI solution did not show any detectable signals. If the two macromolecules were simply dispersed in the mixture without interacting, the CD spectrum of the 1:1 mixture would display the features of (unmixed) PGM with the intensity reduced by half due to dilution of the PGM chromophore. Indeed, the spectrum of 0.5 mg/ml PGM solutions completely overlapped with the numerical average of (unmixed) PGM and b-PEI solutions with 1 mg/ml concentration (Fig. 4.4). In contrast, the spectrum of 1:1 mixture deviated from the numerical average in the region from ca. 207 – 235 nm. This suggests that some changes in the secondary structure of PGM occur as a result of interaction with b-PEI.

This effect is even more pronounced in the near-UV CD spectra of Fig. 4.5. The intense, positive peak observed from 1 mg/ml PGM solution with maximum around 270 nm may originate from two sources. Firstly, commercial mucins are known to contain varying quantities of non-mucin proteins and they may be responsible for the occurrence of tertiary structure signals in the PGM.[9] Secondly, self-aggregated structure of PGM in solution may formulate tertiary structure. The near UV CD signals observed from the mixture of PGM:b-PEI at 1:1 ratio showed similar peak shape compared with those of PGM at halved concentration (0.5 mg/ml), or numerical average, but much lower intensity. If the near UV CD signal of PGM at ca. 270 nm indeed originates from its self-

aggregated structure, the reduced intensity upon mixing with b-PEI indicates that self-aggregated structures of PGM are as a result of the interaction with b-PEI.

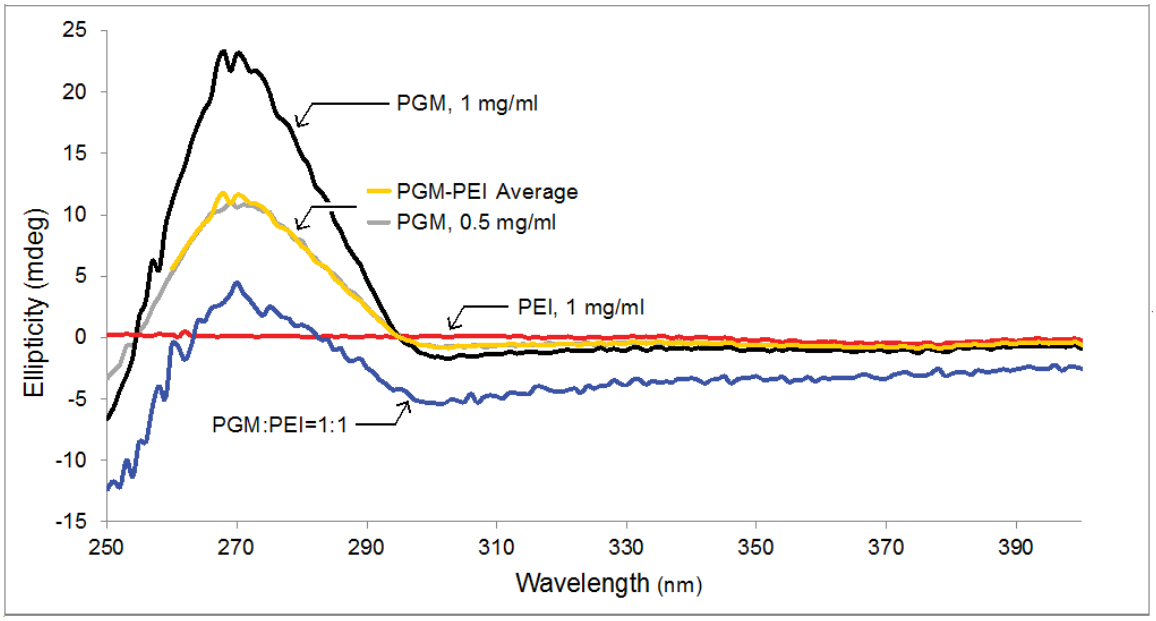

Figure 4.5 Near-UV CD spectra for PGM, b-PEI and their 1:1 mixture. Numerical average is calculated as [(PGM + b-PEI), 1 mg/ml] / 2, and compared with the observed experimental curve for the 1:1 mixture.

4.7 Hydrodynamic size and surfaces charge of PGM upon mixing with b-PEI

Along with the conformational changes as studied by CD spectroscopy, investigation on the changes in hydrodynamic size of PGM before and after mixing with b-PEI can provide further information on the interaction characteristics between them. Fig. 4.6 shows the intensity weighted hydrodynamic size distribution of the polymer solutions as examined by DLS. Three major peaks appeared in the intensity-weighted size distribution of hydrodynamic diameter (d_H) for PGM with local maxima at ca. 130 nm (labeled as

"A"), 761 nm ("B"), and 3000 nm ("C"). PGM has intrinsically high polydispersity due to self-aggregation as mentioned above. In addition, non-mucin biomolecules present in commercially available PGM may contribute to multiple peaks over the wide range of d_H values either as non-bound, free "impurity particles" or as linker between PGM molecules. In contrast, b-PEI showed one dominant d_H population with the maximum at 11 nm.

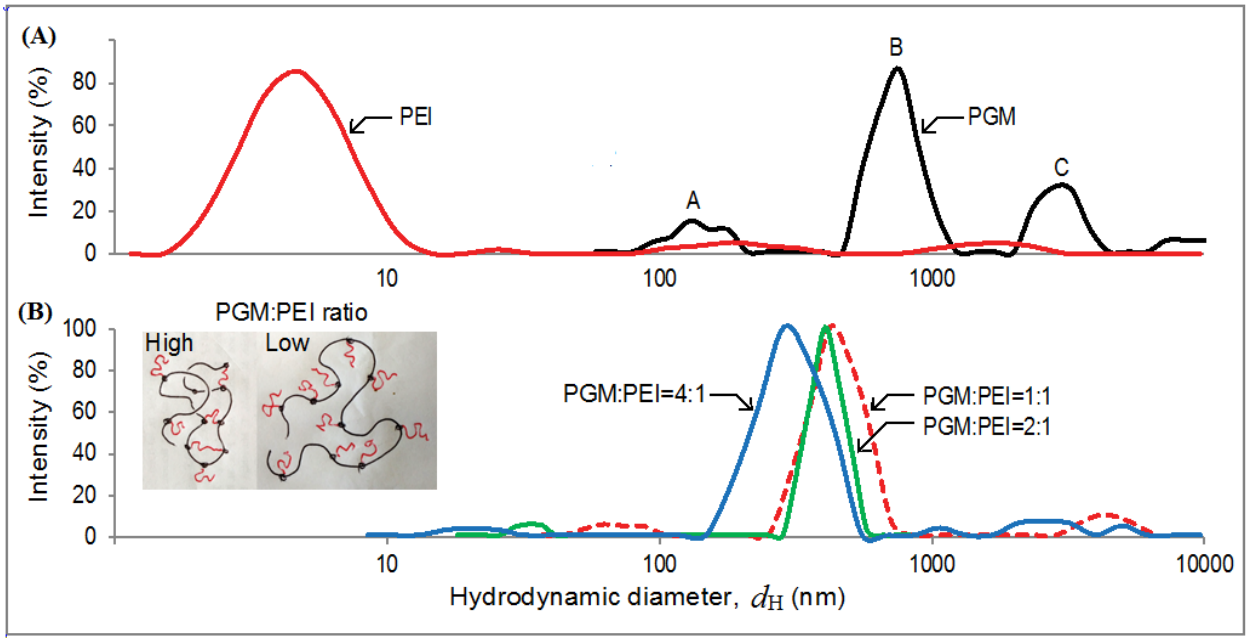

Figure 4.6 Intensity-weighted size distribution showing relative percentage contribution of the size range against the hydrodynamic diameter (d_H) for **(A)** PGM and b-PEI, and **(B)** their mixtures with varying weight ratios. Inset: schematic illustration of the PGM-PEI complex structure as a function of the PEG:PEI mixing ratio.

In PGM:b-PEI mixtures (Fig. 4.6B), the "A" and "C" peaks of PGM were significantly reduced and the peak corresponding to b-PEI, at ca. 11 nm, completely disappeared.

Considering that d_H is orders of magnitude larger for PGM than that for b-PEI (Fig. 4.6A) and b-PEI has notable interaction sites with PGM,[12] these observations indicate that all b-PEI molecules were bound and integrated into much larger PGM molecules. Moreover, the dominant ("B") peak of showed a gradual shift towards smaller values the mixing ratio was increased from 1:1 to 4:1. Therefore, PGM molecules were contracted in the presence of b-PEI suggesting that b-PEI created intra-molecular cross-links within PGM molecules (Fig. 4.6, Inset). In the presence of excess PGM (i.e. for high PGM:b-PEI mixing ratios), b-PEI molecules could make multiple bonds and cross-links within one PGM molecule. As the relative concentration of b-PEI was increased, the number of PGM/b-PEI bonds decreased and PGM contraction was reduced.

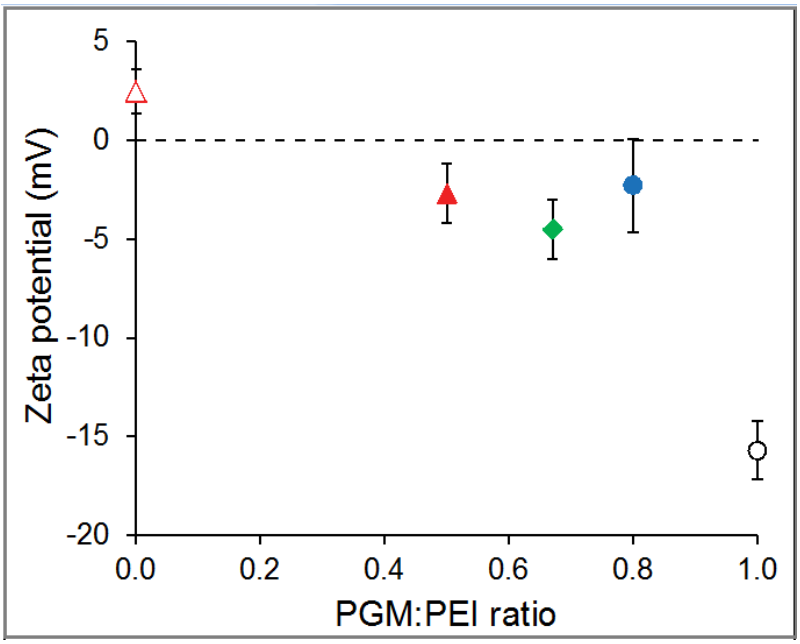

Figure 4.7 Zeta potential (ζ) of PGM, b-PEI and three different mixtures of PGM and b-PEI with varying weight ratios.

PGM and b-PEI are poly-ions bearing multiple negative and positive charges, respectively. Therefore, it is natural to ascribe PGM/b-PEI interaction to electrostatic attraction. This idea was tested by measurements of zeta potentials *(ζ)* on PGM, b-PEI, and their mixtures (Fig. 4.7). As expected, the ζ potential was negative for PGM (-15.7 mV), positive for b-PEI (2.5 mV)and intermediate for their mixture. However, ζ was close to zero for all PGM:b-PEI mixing ratios considered. Therefore, PGM/b-PEI complexes had a much lower surface charge than PGM molecules, supporting the idea that charge compensation drives PGM/b-PEI complexation. Since b-PEI is a small molecule that can penetrate into PGM molecules, PGM:b-PEI complexes as a residual, slightly negative surface charge (Fig. 4.7).

4.8 Influence of salt and chaotropic agent on the size and surface potential of PGM/b-PEI complexes

Fig. 4.8, shows the distribution of d_H of PGM:b-PEI mixture at 1:1 ratio in the presence of 6 M GuHCl and various concentrations of NaCl. In the former case, the peak structure was similar to that of PGM but peak “B” was broadened towards the position occupied in the mixture and peaks “A”, “C” and “D” were amplified compared to PGM. These observations indicate that disrupting hydrogen bonds by adding a chaotropic agent to the mixture tends to disassemble the PGM/b-PEI complexes. However, the b-PEI peak

around 11 nm was not recovered, implying that b-PEI was not released in solution a free species.

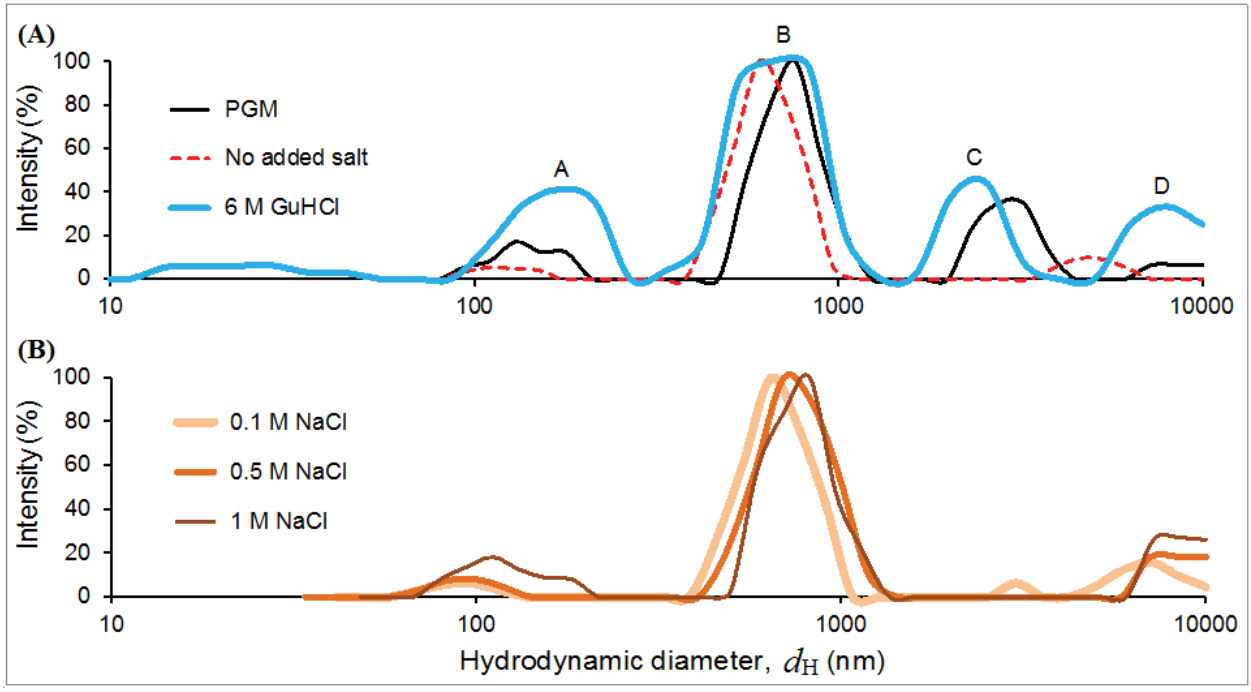

Figure 4.8 Intensity-weighted distribution of hydrodynamic diameter d_H for **(A)** PGM and1:1 PGM:b-PEI with and without 6M GuHCl; **(B)**1:1 PGM:b-PEI mixture with various concentrations of NaCl salt.

Also in the case of NaCl the peak structure evolved from that of the PGM:b-PEI mixture towards that of PGM as the salt concentration was increased. Namely, peaks “A”, “C” and “D” were gradually amplified and peak “B” shifted towards the position occupied in the PGM samples. b-PEI was not released in solution and the peak structure remained closer to that of 1:1 PGM:b-PEI mixture, lacking the “C” peak, i.e. complexes were not disassembled in the presence of NaCl as much as by GuHCl. The shifting of the “B” peak

was due to partial swelling of the complexes due to reduced electrostatic attraction between PGM and b-PEI.

The weakened integrity of PGM:b-PEI aggregates induced by NaCl and GuHCl causes the degradation of boundary lubricating properties of mixtures at PDMS-PDMS sliding contacts (Fig. 4.2). Overall, these observations imply that both electrostatic attraction and hydrogen bonding are responsible for the complexation of the two macromolecules.

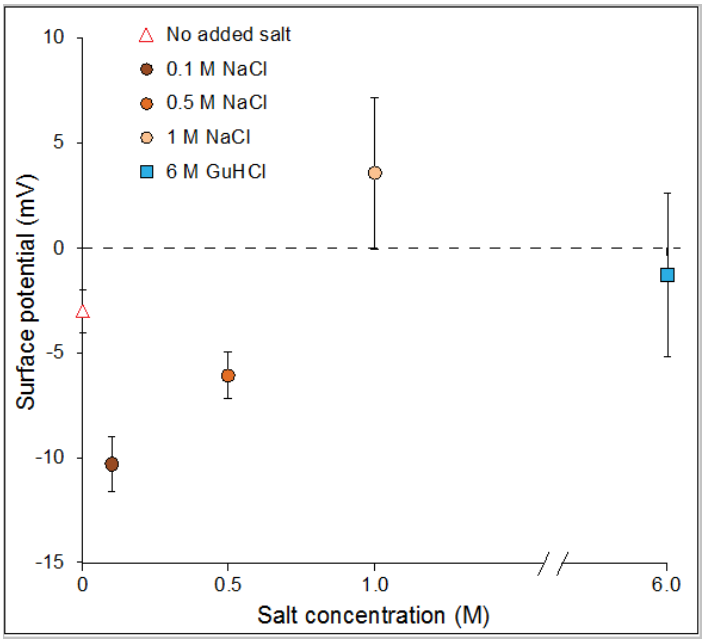

Figure 4.9 Zeta potential of 1:1 mixture of PGM and b-PEI as a function of the concentration of NaCl (0.1M, 0.5M and 1M) and GuHCl salts.

Fig. 4.9 shows ζ for PGM:b-PEI mixture (1:1) with addition of NaCl or GuHCl. Since the pH of the solution was maintained constant for all cases, the absolute surface potential ζ of molecules was expected to decrease with increasing ionic strength due to decreasing thickness of the electric double layer.[13] But for the 1:1 mixture of PGM:b-PEI, a drastic

increase of the absolute value of ζ from -2.31 mV to -10.32 mV was observed upon addition of 0.1 M NaCl first. Then, by further increasing the concentration of NaCl to 0.5 M and 1.0 M, continuous shift of ζ towards positive values was observed. A gradual shift of ζ towards positive values with further increase of NaCl concentration is due to the decreasing thickness of the electric double layer. However, the initial increase in negative ζ of PGM:b-PEI mixture by addition of 0.1 M NaCl cannot be simply explained by changing double layer thickness. This effect has not been addressed and requires additional literature survey or further experimental studies. Additionally, increasing population of smaller species at ca. 100 nm in d_H (Fig. 4.8B) with increasing concentration of NaCl may be composed of higher portion of b-PEI on the surface and contribute to overall positive charges. In contrast, 6M GuHCl did not seem to affect the ζ of the 1:1 PGM:b-PEI mixture significantly. This is probably because the influence of 6 M GuHCl on the structure of PGM:b-PEI aggregates is mainly disruption of hydrogen bonding, which has little contribution to ζ values.

4.9 Conclusions

In this study, we have shown that the aqueous lubricating properties of PGM can be significantly improved by adding b-PEI, a polycations that is widely utilized as mucoadhesive in medical applications. Compared to PGM:chitosan mixture which are stable only at low pH, PGM:b-PEI mixtures show enhanced lubrication in the boundary lubrication regime at neutral pH where applications are most anticipated in medicine and

bioengineering. Also, enhanced lubrication was obtained with b-PEI concentrations as small as 20% w/w (in 1:1 mixtures), to be compared with the 50% w/w concentration required to improve lubrication in PGM:chitosan mixtures. Moreover, due to exceedingly higher water solubility of b-PEI than chitosan, water-dissolvable mixtures of PGM:b-PEI can be obtained at much higher concentrations.

The mechanism of boundary lubrication of PGM:b-PEI mixtures is synergistic in the sense that neither one of the two polymers is able to provide good lubrication (friction coefficient $\mu < 0.1$) when taken alone. Our work showed that the synergy stems from strong attractive interactions and complexation between PGM and b-PEI involving both electrostatic and hydrogen bonding. Therefore, lubrication can be tuned in PGM:b-PEI mixtures by adding electrolytes and chaotropic agents. Also. the lubrication synergy is not simply correlated to how abundantly or strongly the polymers adsorb onto the surfaces to be lubricated.

References

[1] Strous, G. J.; Dekker. J. *Critical Reviews in Biochemistry and Molecular Biology*, **1992**,
7:1-2, 57-92.
[2] Coles, J. M.; Chang, D. P.; Zauscher, S. *Current Opinion in Colloid & Interface Science* **2010**, 15 406–416.
[3] Bansil, R.; Turner. B. S. *Current Opinion in Colloid & Interface Science* **2006**, 11, 164–170.
[4] Khutoryanskiy, V. V. *Macromol. Biosci.***2011**, 11, 748–764.
[5] Nikogeorgos, N.; Efler, P.; Kayitmazer, A. B.; Lee, S. *Soft Matter* **2015**, 11, 489-498.
[6] Boussif, O.; Lezoualch, F.; Zanta, M. A.; Mergny, M. D.; Scherman, D.; Demeneix, B.; Behr, J. P. *PNAS* **1995**, 92(16), 7297-7301.

[7] Griffiths, P. C.; Occhipinti, P.; Morris, C.; Heenan, R. K.; King, S. M.; Gumbleton, M. *Biomacromolecules* **2010**, 11, 120-125.
[8] Godbey, W. T.; Wu, K. K.; Mikos, A. G. *Journal of Controlled Release* **1999**, 60(2-3), 149-160.
[9] Lee, S.; Muller, M.; Rezwan, K.; Spencer, N. D. *Langmuir* **2005**, 21, 8344-8353.
[10] Lee, S.; Muller, M.; Heeb, R.; Zurcher, S.; Tosatti, S.; Heinrich, M.; *Tribol Lett.***2006**, 24, 217-223.
[11] Kelly, S. M.; Jess, T. J.; Price, N. C. *Biochimica et BiophysicaActa (BBA) - Proteins and Proteomics* **2005**,*1751* (2), 119-139.
[12] Huang, Y.; Peppas, N. A. *Nanotechnology in Therapeutics: Current Technology and Applications***2007**,109-129, Horizon Press, Norfolk, UK.
[13] Salgin, S.; Salgin, U.; Bahadir, S. *Int. J. Electrochem. Sci*. **2012**, **7**, 12404-12414.

Conclusions and Outlook

Surface adhesion of *P. viridis* mussel foot proteins

SFA was used for investigating adhesive properties of purified Pvfp-5 and Pvfp-3 taken individually or in combination. Dopa rich Pvfp-5 was adhesive at acidic, neutral and basic pH conditions and the maximum adhesion was recorded at acidic pH. Pvfp-3 was adhesive at both, acidic and basic pH conditions tested. Considering the time-regulated secretion of Pvfps, Pvfp-5 appears to be at the forefront of the initial interactions with external surfaces exhibiting more surface adhesive character than Pvfp-3 at acidic pH, but more adhesion was measured for Cys-rich Pvfp-3 at basic pH conditions. Adsorbing Pvfp-5 and Pvfp-3 simultaneously showed a significant decrease in adhesion compare with Pvfp-5 alone, which further supports the stepwise secretion of Pvfps to create a functional adhesive multilayer with Pvfp-5 serving as a vanguard protein.

Given the high content of Cys within Pvfps, another plausible scenario is that intermolecular disulphide bond formation could protect Dopa residues from oxidation via redox chemistry. In other words, Pvfp-3 and Pvfp-5 may be able to protect themselves against Dopa oxidation and therby minimizing loss of adhesion, a hypothesis that will be tested in future work.

An understanding of green mussel adhesion is critical to the development of specific anti-fouling strategies against the species that will contribute to the design of environment friendly antifouling paints and to the development of underwater adhesives strategies for

the development of adhesives for medical and dental applications such as cell and tissue adhesives and as surgical glues for sealing soft and hard tissues.

Molecular structure and equilibrium forces of adsorbed bovine submaxillary mucin

The primary objective of our work on chromatographically purified BSM was to study the conformation of BSM in dilute solution and nanomechanical properties of adsorbed mucin layers adsorbed on mica. The mucin molecule can be described as wormlike semiflexible polymer chain due to the large persistence length of its central glycosylated domain. Mucin molecules adsorbed abundantly onto mica from saline buffer, generating polymer-like, long-ranged, repulsive, and nonhysteretic forces upon compression of the adsorbed layers. Detailed analysis of such forces suggests that adsorbed mucins favor an elongated conformation due to the stiffness of its heavily glycosylated central domain. Acidification of aqueous media was chosen as means to reduce mucin-mucin and mucin-substrate electrostatic interactions. The hydrodynamic diameter in solution did not significantly change when the pH was lowered, showing that the large persistence length of the mucin molecule is due to steric hindrance between sugar chains, rather than electrostatic interactions. Remarkably, the force generated by an adsorbed layer with a fixed surface coverage also remained unaltered upon acidification. This observation can be linked to the surface-protective, pH-resistant role of BSM in the variable environmental conditions of the oral cavity. The extensive knowledge about the structure

of mucins their surface adsorption and nanomechanical properties may serve as inspiration towards the development of next generation protective, anti-biofouling, lubricating and biocompatible surface coating materials.

Interaction between porcine gastic mucin and cationic polymer branched polyethyleimine

General understanding of complex interaction between mucins and polymers requires systematic investigation to unveil its full potential. Interaction of PGM with b-PEI was studied at neutral pH conditions and the results obtained reveal that synergistic interaction of PGM with b-PEI significantly improved its boundary lubricating capability. The mechanism of boundary lubrication of PGM:b-PEI mixtures is synergistic in the sense that neither one of the two polymers is able to provide good lubrication (friction coefficient $\mu < 0.1$) when taken alone. Our work showed that the synergy stems from strong attractive interactions and complexation between PGM and b-PEI involving both electrostatic and hydrogen bonding. Superior lubricating property of PGM:b-PEI mixture can be exploited in various biomedical and bioengineering applications where neutral pH conditions are anticipated. Moreover, due to exceedingly higher water solubility of b-PEI, water-dissolvable mixtures of PGM:b-PEI at much higher concentrations can be obtained. Rheological and tribological properties of these high concentration gels is under study.

List of Publications

Title:	Status
Aqueous lubricating properties of charged (abc) and neutral (aba) triblock copolymer chains.	Article published in Polymer, 2014.
Molecular structure and equilibrium forces of bovine submaxillary mucin adsorbed at a solid-liquid interface.	Article published in Langmuir, 2015.
Mussel adhesion is dictated by time-regulated secretion and molecular conformation of mussel adhesive proteins.	Article published in Nature Communications, 2015.
Enhanced boundary lubricating properties of porcine gastric mucin via complexation with branched poly(ethylene-immine) in neutral aqueous solution.	Manuscript in preparation.
Interaction of porcine gastric mucin with various polycations and its influence on the boundary lubricating properties.	Manuscript in preparation.